Target Emission and Wall Response: National Ignition Facility Target Area Studies Interim Report for the Period 5/1/95 Through 3/31/96

R.R. Peterson, J.J. MacFarlane, J.F. Santarius, G.A. Moses

April 1996

UWFDM-1008

FUSION TECHNOLOGY INSTITUTE

UNIVERSITY OF WISCONSIN

MADISON WISCONSIN

Target Emission and Wall Response:
National Ignition Facility Target Area Studies
Interim Report for the Period 5/1/95 through 3/31/96

Robert R. Peterson, J. J. MacFarlane, J. F. Santarius, and G. A. Moses

Fusion Technology Institute
University of Wisconsin-Madison
1500 Engineering Drive
Madison, WI 53706

April 1996

UWFDM-1008

Contents

1. Introduction **1**

2. NIF X-ray Source **5**

2.1. Indirect Drive 5

2.2. Direct Drive 19

2.3. Comparison of Direct and Indirect Drive 25

3. NIF Wall Response to Target Emissions **26**

3.1. Vaporization and Melting of Wall 26

3.2. Tritium Deposition in NIF Target Chamber Walls 32

3.3. Material Properties of Alumina Plasma Sprayed Coatings 43

4. Code Development **44**

4.1. Testing of BUCKY Results 44

4.1.1. Ion Stopping 44

4.1.2. Radiation Transport and Hydrodynamics 45

4.1.3. X-ray Vaporization 56

4.1.4. Ion Vaporization and Melting 60

4.2. Code Development 68

4.2.1. BUCKY Laser Deposition 68

4.3. BUCKY Ion Deposition in Solids 70

4.3.1. ZEUS 2-D Radiation Hydrodynamics Code 70

5. Future Work **71**

1. Introduction

During the period 5/1/95 through 3/31/96, considerable progress was made on the study of target chamber phenomena in the National Ignition Facility (NIF). Three general areas of emphasis were selected for this period. The calculation of the x-ray and debris emission from the direct drive and indirect drive NIF target, shown in Figures 1.1 and 1.2, is the first general topic studied. The response of the target chamber wall to the target x-ray and debris emissions is the second; the melting and vaporization from the walls of the NIF target chamber coated with several candidate materials is calculated. Tritium penetration into the walls is part of this general area. Finally, the BUCKY [1] code, which is used in these calculations, has been documented, compared with other codes and experiments, and laser deposition physics has been added. Also, a 2-D radiation hydrodynamics code was under development.

The NIF target area is shown in Figure 1.3. The general features of the target chamber are listed in Table 1.1. The first wall is coated with one of several possible materials. The three most likely materials are shown in the table. The coating is on a substrate of aluminum alloy, which is the structural material for the target chamber. The coating must undergo only a minimal amount of vaporization and melting from the x-rays and debris from any likely target explosion. The material that is lost from the target chamber walls could deposit onto the debris shields that protect the laser optics, requiring cleaning. Energetic tritium ions from the targets will penetrate the surface of the coatings and the debris shield, leading to a growing radioactive inventory that can be controlled through periodic cleaning by removal of the surface layers. The work discussed in this report addresses both of these issues.

In this report, the progress on the analysis of these issues is discussed. The first topic is the x-ray and debris emission by the NIF targets. These x-rays are an important part of the threat to the first wall. Computer code simulations of the x-ray emissions from direct and indirect drive targets are presented. Likewise, debris emissions are presented. The response of the materials listed in Table 1.1 to x rays and debris is then discussed. In all of the results presented, radiation-hydrodynamic computer codes are used. The BUCKY code is heavily used in this work. The validity of this code is crucial to this work. Experiments to test the code and comparisons with other codes are discussed. Also, developments to the BUCKY 1-D and ZEUS 2-D codes are discussed. Finally, work on the target chamber of NIF is not finished, so future work is discussed.

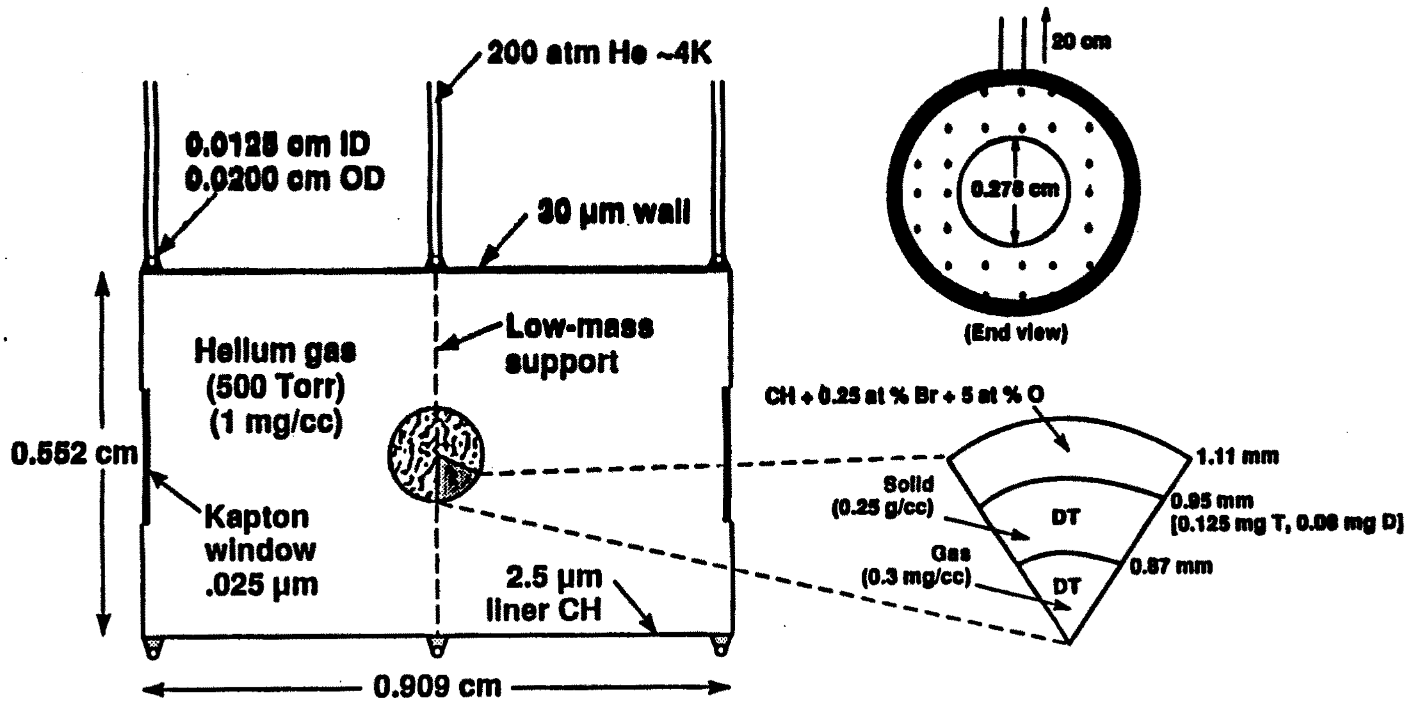

Figure 1.1. NIF indirect drive target.

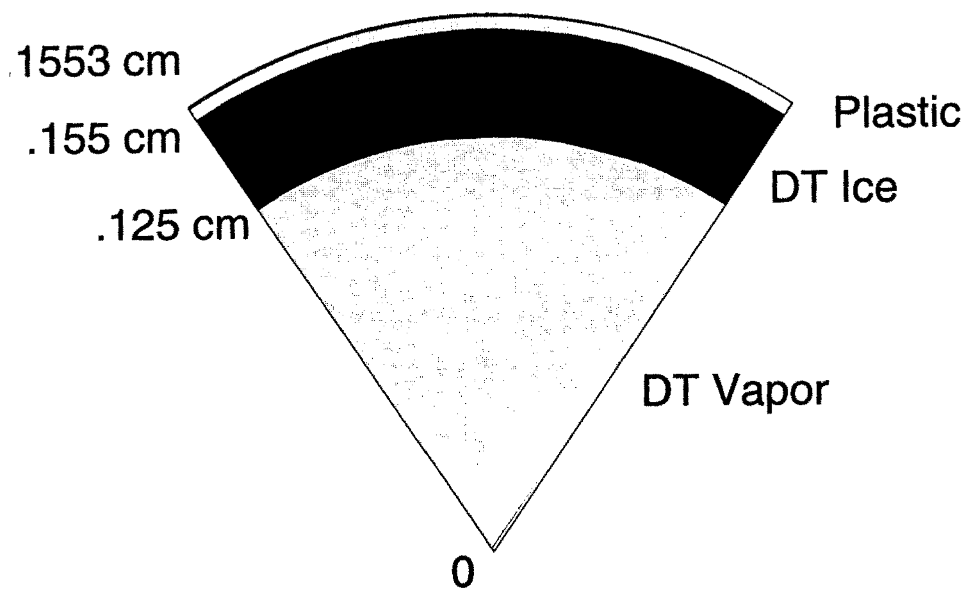

Figure 1.2. NIF direct drive target.

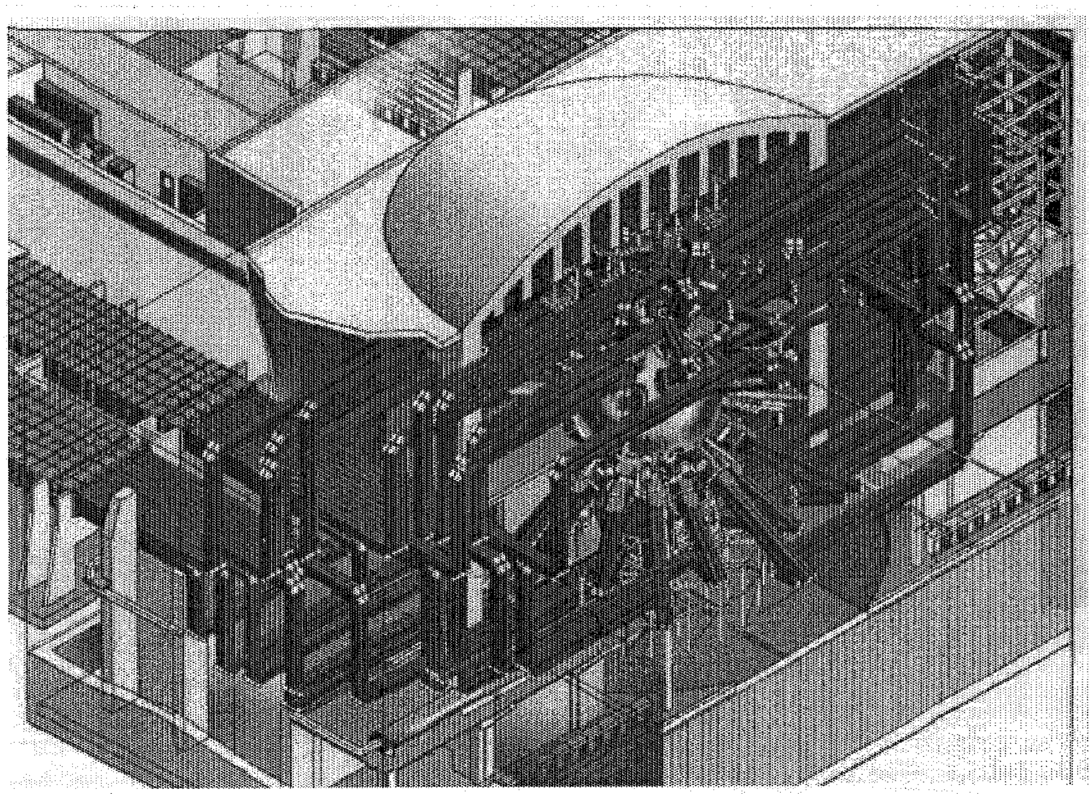

Figure 1.3. Schematic picture of NIF target area.

Table 1.1. NIF Target Area Parameters

First wall radius (m)	5
First wall material	Aluminum alloy
First wall coating	Plasma sprayed B_4C, Plasma sprayed Al_2O_3, Carbon/carbon composite
Optical material	SiO_2
Target chamber atmosphere	Vacuum

2. NIF X-ray Source

2.1. Indirect Drive

The emission of x-rays and debris by the NIF indirect drive target is due to the complicated interaction of several phenomena. These are depicted in Figure 2.1. Some x-ray emissions from the laser plasmas take place during the implosion phase. When the target burns, some hard x-rays are emitted by the fuel capsule. The capsule then expands very rapidly and then collides with the hohlraum case. This collision generates a stagnated hot plasma that radiates x-rays, some of which leave the target through the laser entrance holes. Finally, the target disassembles into debris.

One-dimensional BUCKY code simulations of radiative breakout of the NIF indirect target, shown in Figure 1.1, have been performed. These are one-dimensional simulations of an inherently two dimensional process. Simulations have been performed in three directions; spherically out from the center of the capsule through the gold case, spherically out from the center of the capsule through the laser entrance hole, and from the back of the gold case at the point nearest the capsule out through the laser entrance hole in a slab geometry. The final calculation is called oblique. The three directions are depicted in Figure 2.2.

No thermonuclear burn occurs in these simulations. It is assumed that burn has finished before the run starts. The burn energy is included in the initial energy in the capsule at the beginning of each run. The initial conditions (mass density, velocity, and temperatures) are obtained from the “out through case” run and the “laser entrance hole” run from profiles supplied by Jon Larsen [2], which are results of a simulation with the HYADES [3] code. This calculation also neglected thermonuclear burn, but did model the implosion. The appropriate amounts of energy were added to these initial conditions by adjusting the temperature of the DT fuel. This procedure ignores the finite thermonuclear

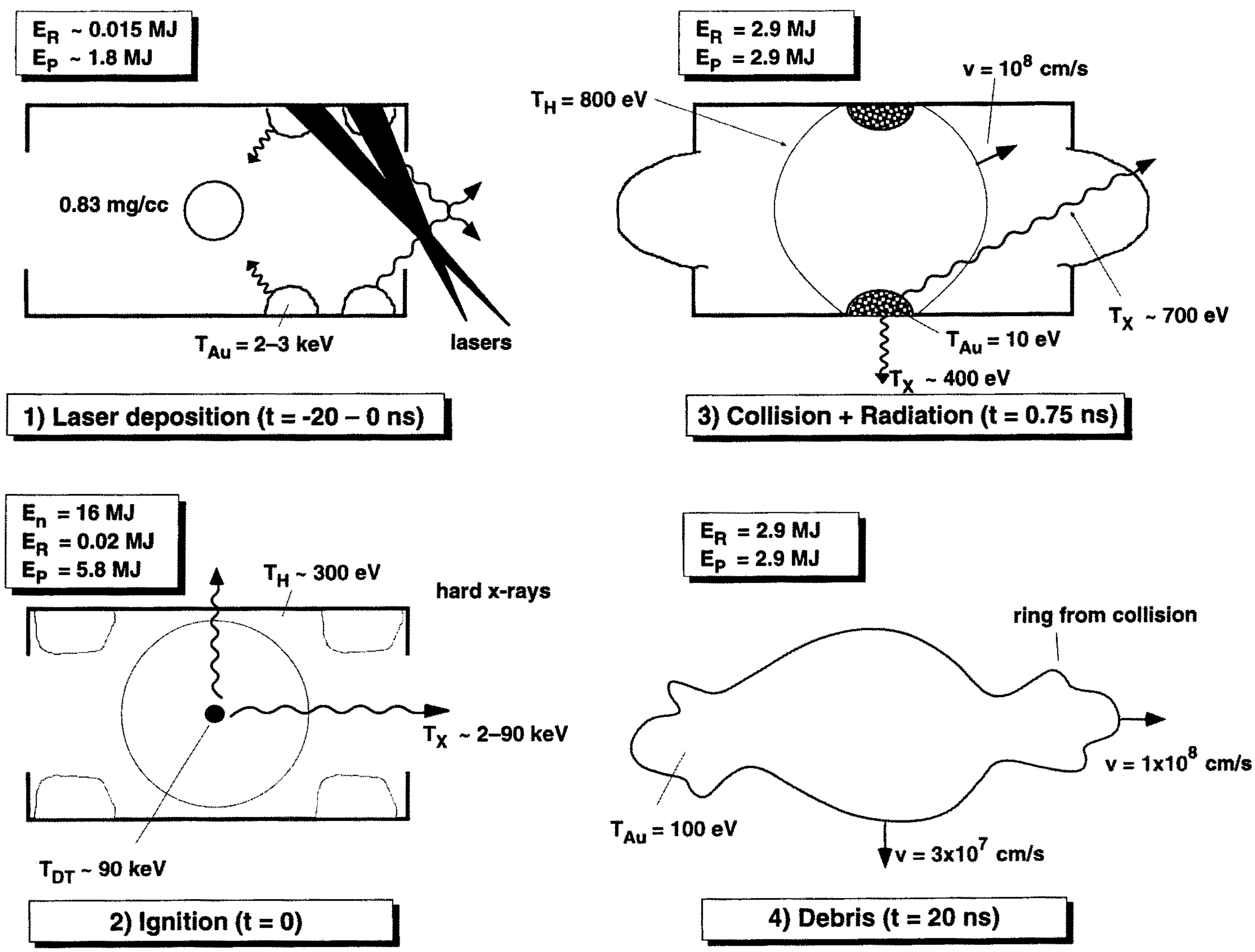

Figure 2.1. Schematic picture of the radiative disassembly of the NIF indirect drive target.

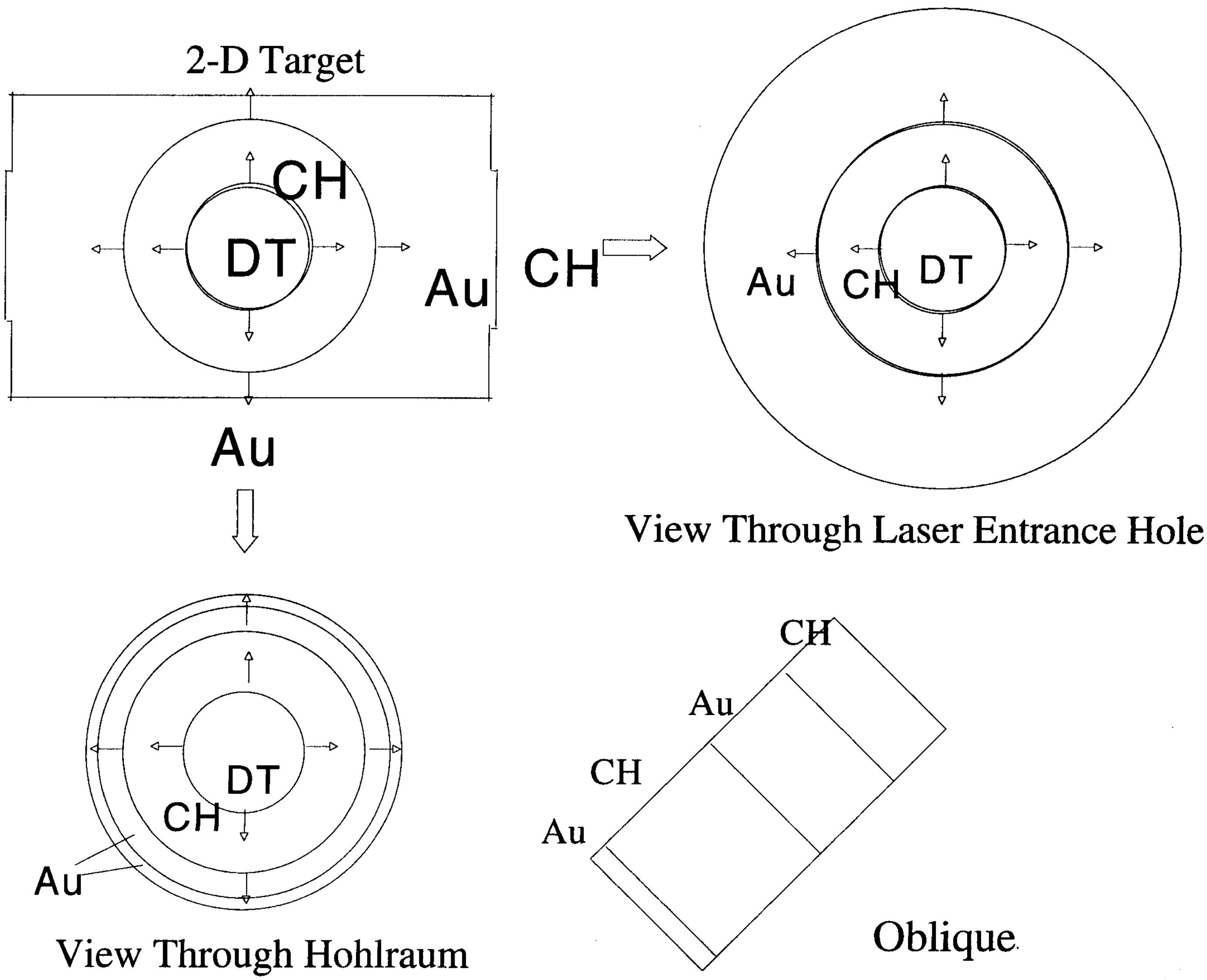

Figure 2.2. One-dimensional simulations of the radiative break-up of the NIF indirect drive target.

burn time and the transmutation of a fraction of the DT into helium. The first will tend to predict a higher than correct temperature for the DT plasma. The initial density, velocity, and temperature profiles for the calculation in the direction "out through the case" is shown in Figure 2.3. The initial condition for the "out through the laser entrance hole case" is the same, except the high mass density gold is excluded and a larger region of gold vapor is added. The initial conditions for the "oblique" run will be discussed later.

The BUCKY code used in these simulations has been used to study a variety of target chamber related physical phenomena, including laser and ion beam deposition, target implosion, thermonuclear burn, target microexplosions, fireballs in gases, and x-ray and debris ion response of structures in a target chamber. The hydrodynamic motion of the target plasma and the radiation released by the target are the issues of interest here. Hydrodynamic motion is calculated with a Lagrangian finite differencing scheme. Radiation transport is calculated here with multigroup flux limited diffusion, though BUCKY has options to transport individual lines or to use higher order multigroup methods. Equations-of-state and opacities are read in from tables generated by the EOSOPAC [4] codes. The opacities are calculated with an unresolved transition array method for high atomic numbers, and a detailed configuration accounting method at low atomic number.

The results from the "out through case" run are depicted in Figures 2.4 through Figure 2.8. The plot of Lagrangian zone boundary positions against time is seen in Figure 2.4. One can clearly see the collision between the rapidly expanding capsule and the gold case that occurs at about 0.75 ns after the end of the burn. The density, temperature, and velocity profiles are shown at the time of the collision between the capsule and case in Figure 2.5, and at the end of the run in Figure 2.6. Near the collision time, one can see the high temperature where the capsule plasma is stagnating against the gold. At the end of the run, one can see that the gold is at a velocity between 1.3×10^6 and 2.5×10^6 cm/s. The spectrum time-integrated spectrum up to various times leaving the back of the gold case is shown in Figure 2.7. The spectrum integrated out to the end of the run is approximately a blackbody spectrum at 200 eV. The radiant power out the back of the case is shown in Figure 2.8. The peak power corresponds to the time of the collision between case and capsule.

The results from the "out through hole" run are depicted in Figures 2.9 through Figure 2.12. The plot of Lagrangian zone boundary positions against time is shown in Figure 2.9. One sees the rapidly expanding capsule with no impediment sweeping up the gold vapor in its path. The density, temperature, and velocity profiles are shown at the end of the run in Figure 2.10. One can see that the gold is at a velocity between 1.2×10^8

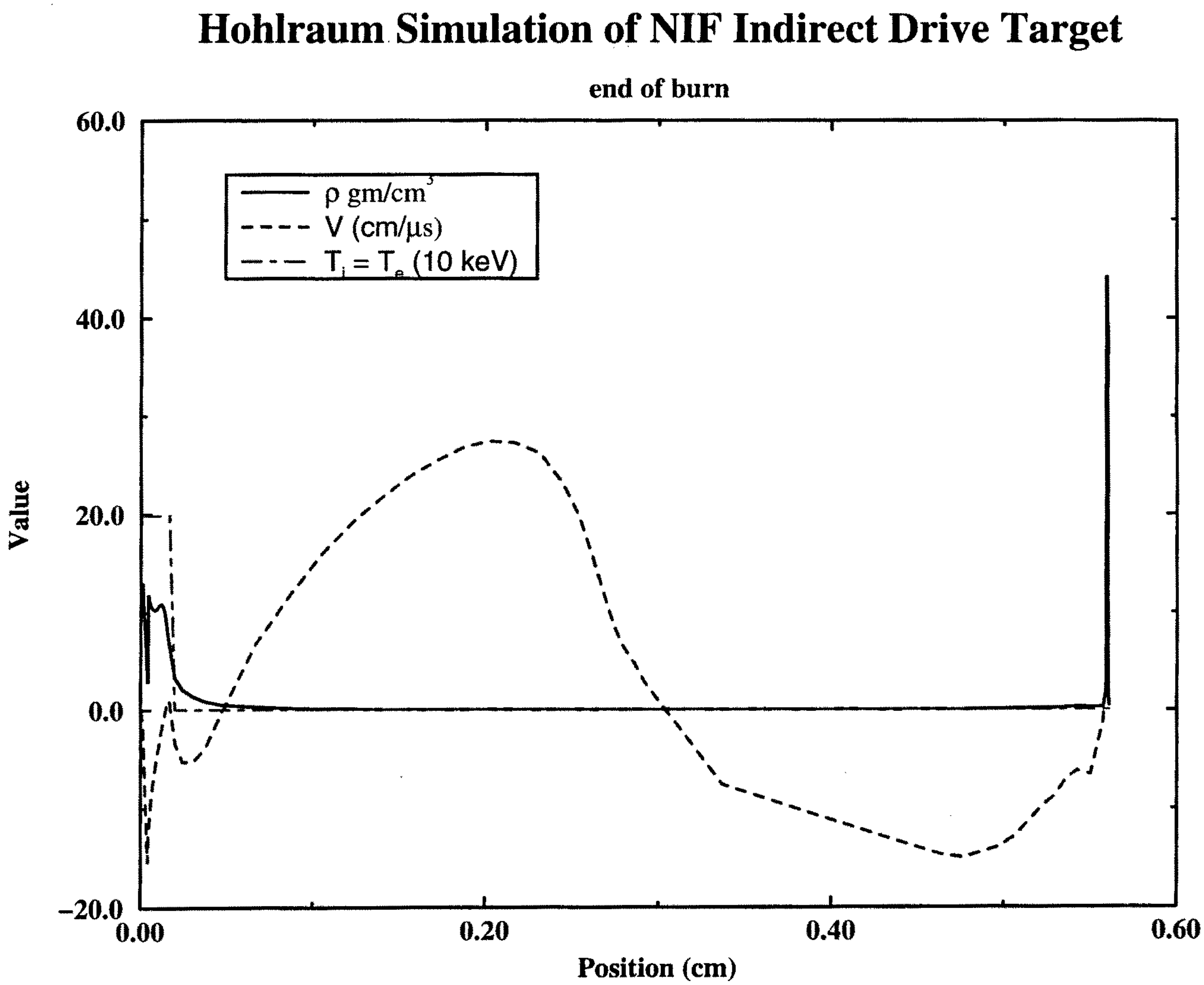

Figure 2.3. Initial conditions for one-dimensional simulations of the radiative break-up of the NIF indirect drive target. Profiles of mass density, fluid velocity, and ion temperature are plotted against distance from the center of the capsule at a time shortly after the end of the burn..

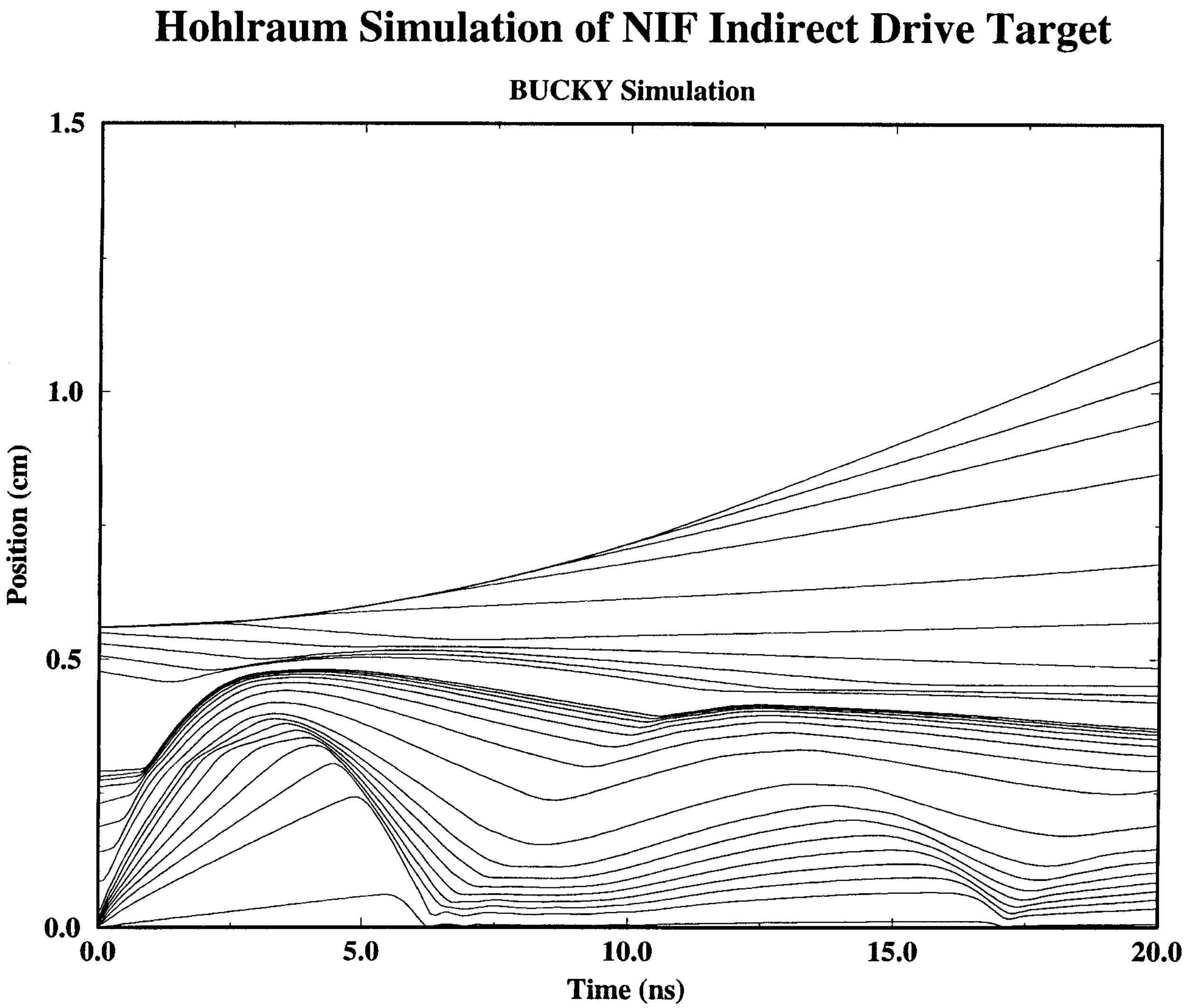

Figure 2.4. BUCKY simulation of the behavior of the NIF indirect drive target in the direction from the center of the capsule out through the case at the nearest point. The positions of Lagrangian zone boundaries are plotted against time.

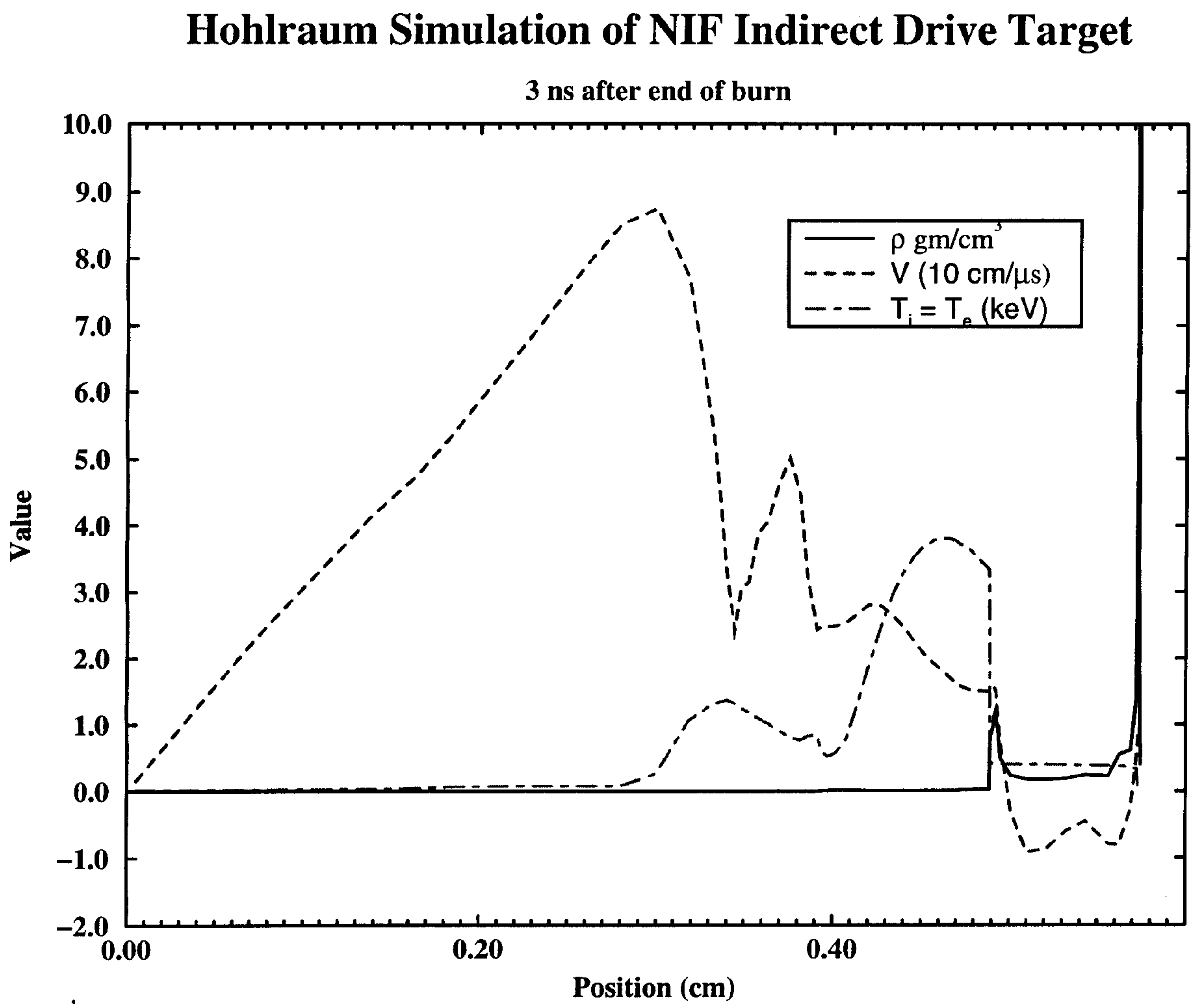

Figure 2.5. BUCKY simulation of the behavior of the NIF indirect drive target in the direction from the center of the capsule out through the case at the nearest point. Profiles of mass density, fluid velocity, and ion temperature are plotted against distance from the center of the capsule approximately at the time of peak stagnation.

Hohlraum Simulation of NIF Indirect Drive Target

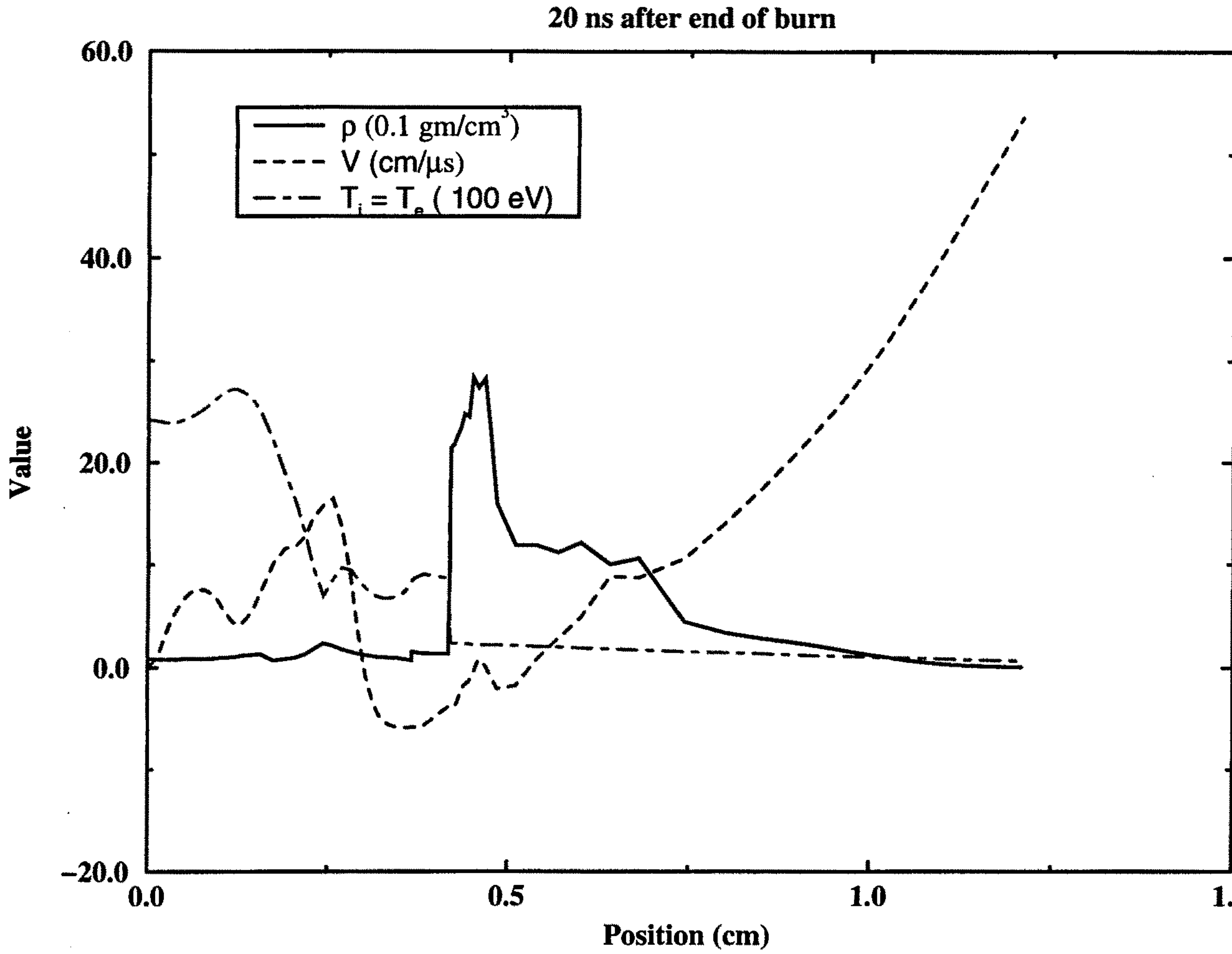

Figure 2.6. BUCKY simulation of the behavior of the NIF indirect drive target in the direction from the center of the capsule out through the case at the nearest point. Profiles of mass density, fluid velocity, and ion temperature are plotted against distance from the center of the capsule at the end of the run.

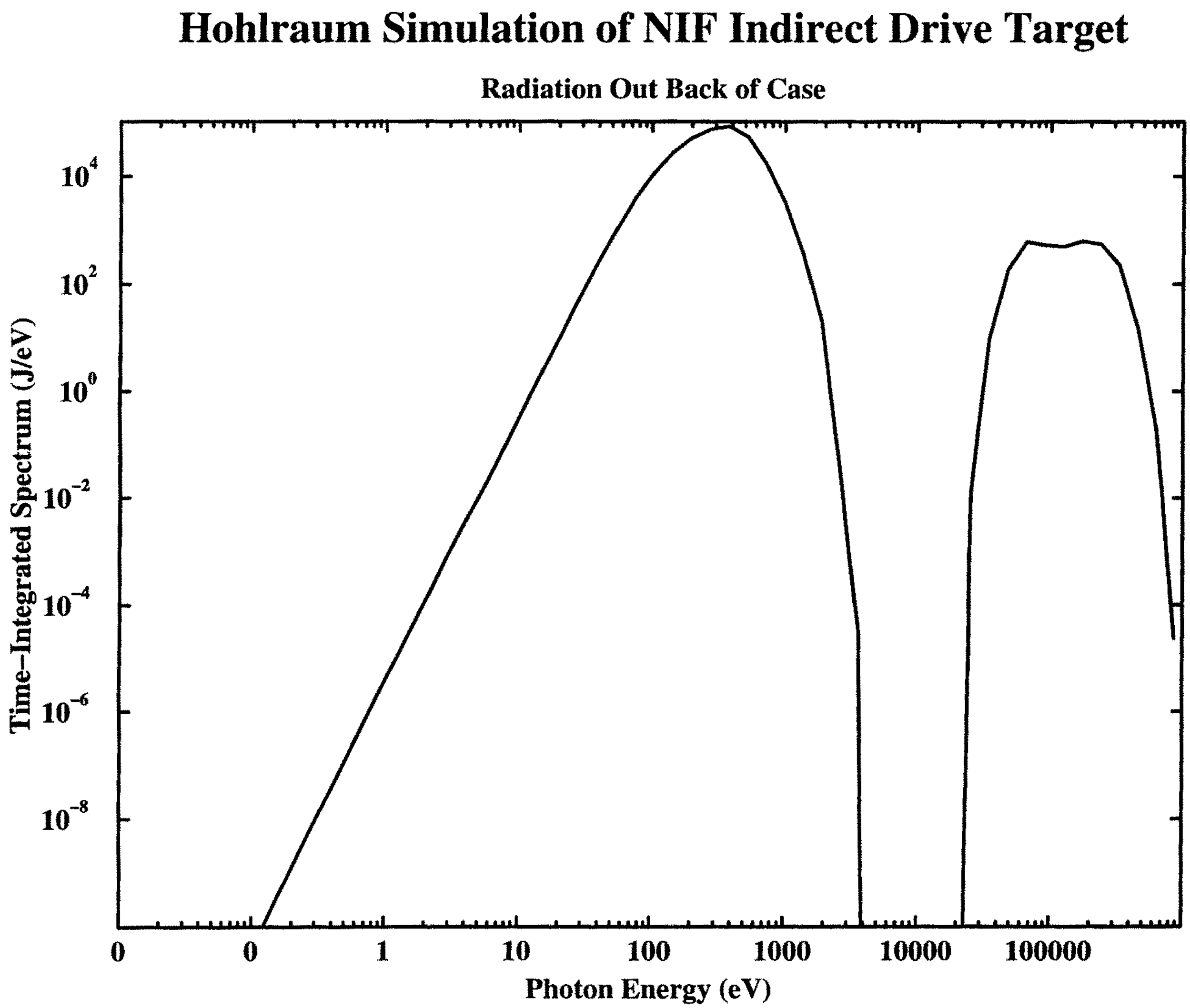

Figure 2.7. BUCKY simulation of the behavior of the NIF indirect drive target in the direction from the center of the capsule out through the case at the nearest point. The time integrated spectrum is shown integrated out to 20 ns for the radiation coming out the base of the case.

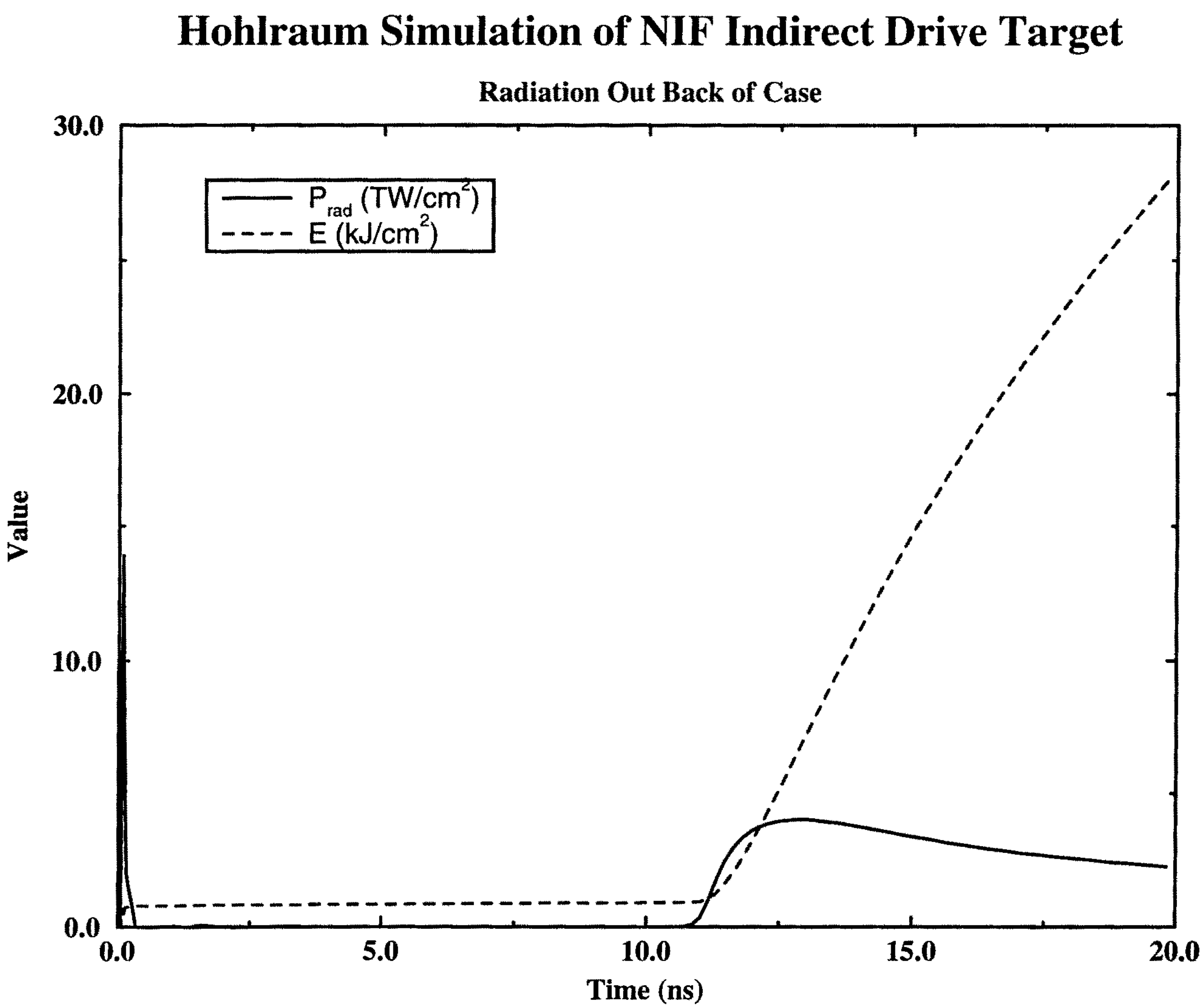

Figure 2.8. BUCKY simulation of the behavior of the NIF indirect drive target in the direction from the center of the capsule out through the case at the nearest point. The radiant power and fluence are plotted against time.

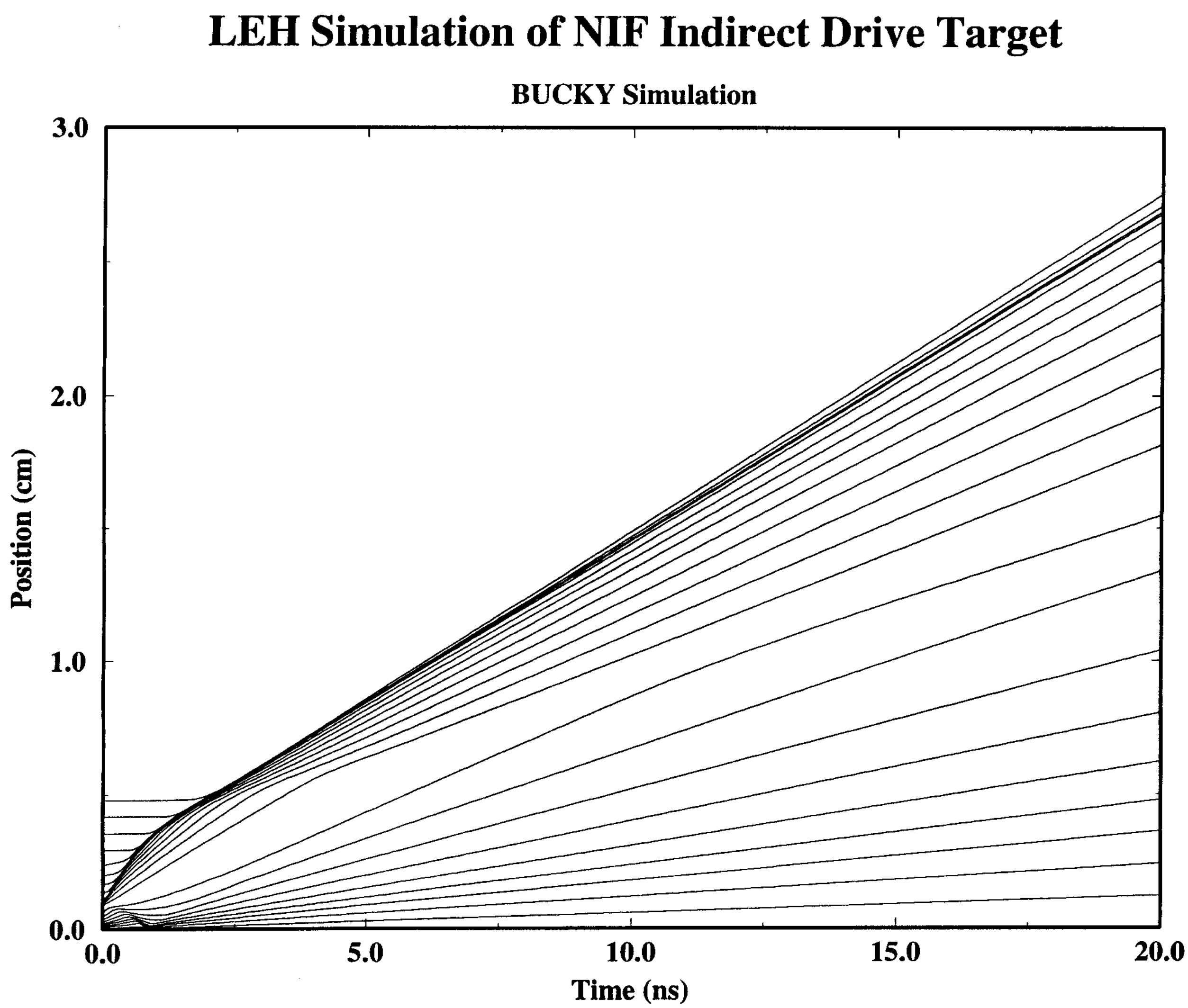

Figure 2.9. BUCKY simulation of the behavior of the NIF indirect drive target in the direction from the center of the capsule out through the laser entrance hole. The positions of Lagrangian zone boundaries are plotted against time.

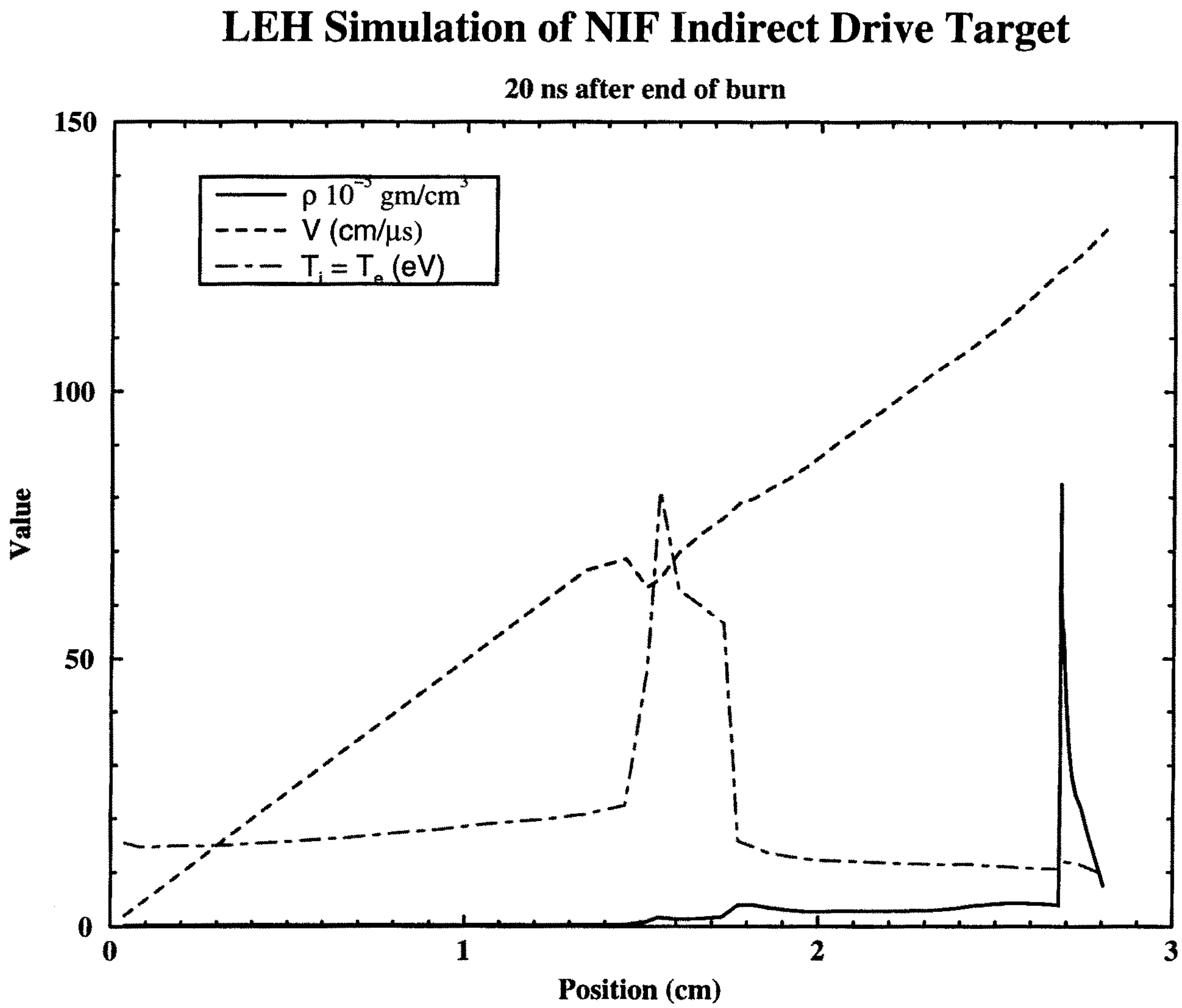

Figure 2.10. BUCKY simulation of the behavior of the NIF indirect drive target in the direction from the center of the capsule out through the laser entrance hole. Profiles of mass density, fluid velocity, and ion temperature are plotted against distance from the center of the capsule approximately at the end of the run.

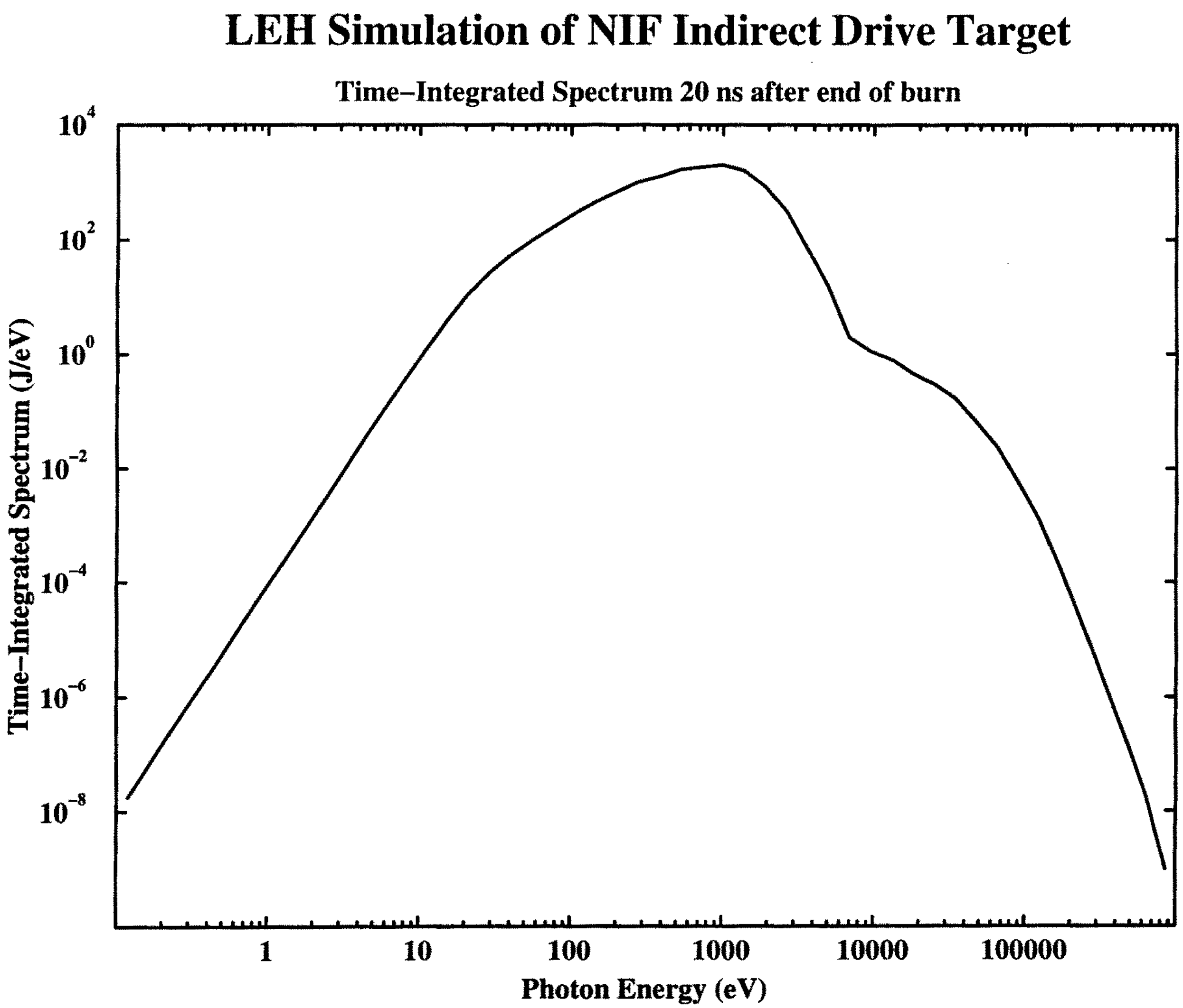

Figure 2.11. BUCKY simulation of the behavior of the NIF indirect drive target in the direction from the center of the capsule out through the laser entrance hole. The time integrated spectrum is shown integrated out to 20 ns for the radiation coming out the back of the gold vapor.

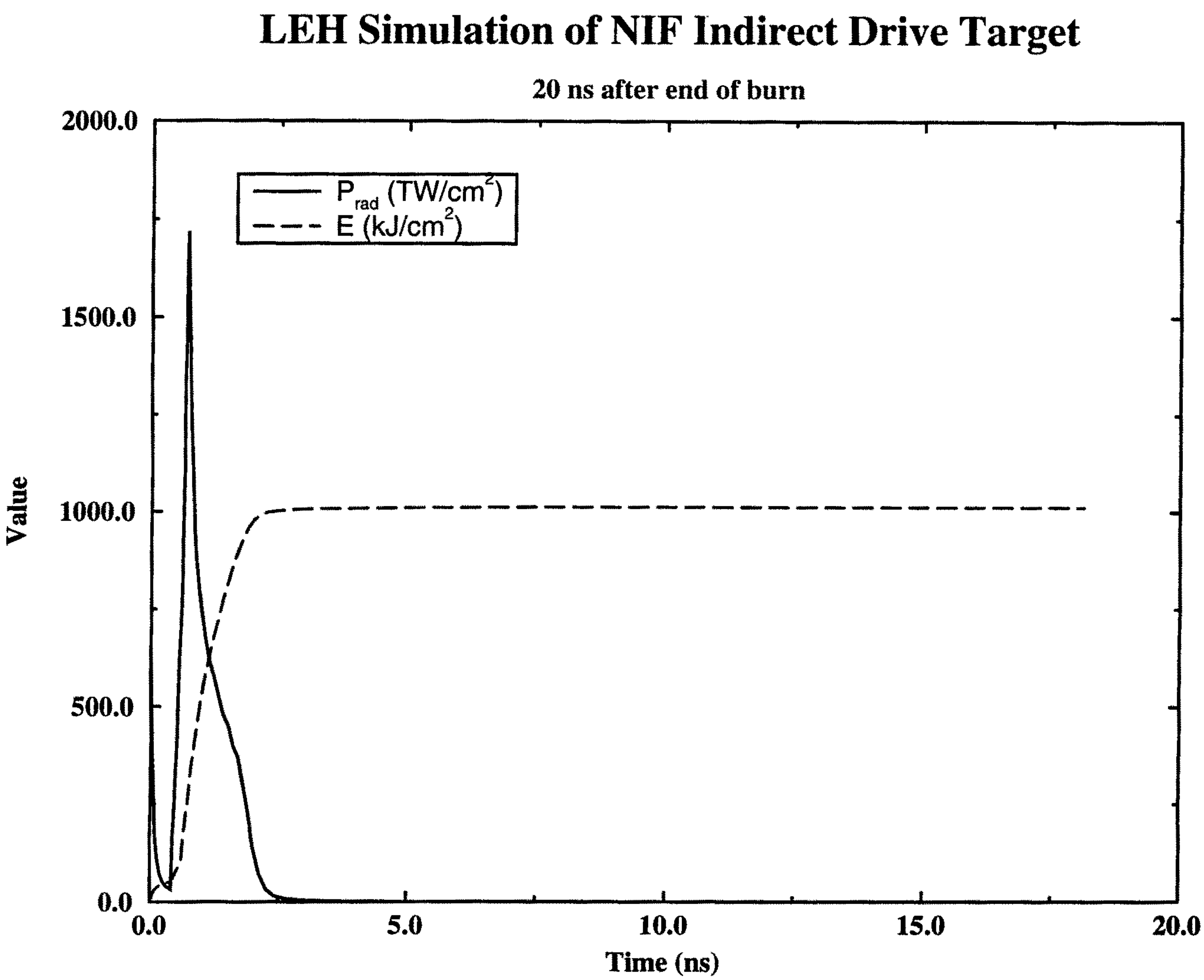

Figure 2.12. BUCKY simulation of the behavior of the NIF indirect drive target in the direction from the center of the capsule out through the case at the nearest point. The radiant power and fluence are plotted against time.

and 1.3×10^8 cm/s, and that the DT and plastic velocities increase linearly with distance from the target. The time-integrated spectrum up to various times leaving the back of the gold vapor is shown in Figure 2.11. The spectrum integrated out to the end of the run is approximately a blackbody spectrum at 330 eV. The radiant power out the back of the gold vapor is shown in Figure 2.12.

The results from the "oblique" run are depicted in Figures 2.13 through Figure 2.16. The plot of Lagrangian zone boundary positions against time is given in Figure 2.13. This is a slab calculation with motion allowed at both boundaries. The initial conditions are taken from the "out through the case" run at peak stagnation. One sees the expanding high pressure stagnation region pushing the low pressure gold vapor in its path. The density, temperature, and velocity profiles are shown at the end of the run in Figure 2.14. The time-integrated spectrum up to various times leaving the laser entrance hole is shown in Figure 2.15. The radiant power out the laser entrance hole is shown in Figure 2.16.

2.2. Direct Drive

The x-ray and debris emission from a direct concept for a NIF target has been studied with Lasnex and BUCKY. The basic target concept is a pure solid DT inner shell with an outer plastic shell and the central void filled with DT vapor. The design is shown in Figure 1.2. The laser pulse must be carefully shaped to implode this target. Chris Fontes at LANL has designed a laser pulse shape that implodes this target to ignition, generating about 40 MJ of yield. We have continued Fontes' Lasnex run to the point in time when the target stops emitting x rays and the velocity profiles in the target stabilize. The emitted x-ray spectrum is hard (a blackbody spectrum of 1.7 keV). The Lasnex calculations predict a yield of about 40 MJ. We have used the BUCKY code to continue this study. BUCKY now has the capability to simulate laser deposition. The velocity, temperature and density profiles are shown in Figure 2.17. From these profiles, we have deduced a target debris energy spectrum. The deutrium and tritium forms the peak in density at 2 cm. We have approximated the DT density profile as a Gaussian with a half width of 0.7 cm. The bump in density at 5 cm is due to the plastic ablator. The velocity profile is linear in position and peaks at 0.5 cm/ns at 5 cm from the original center of the target.

From these profiles we have generated a discrete energy spectrum. The spectrum is shown in Table 2.1. The spectrum consists of seven energy bins, where each bin has a given species, particle energy and power. The time of arrival of the start and end of each ion bin is given 5 m from the target, the position of the NIF first wall. There is a great deal of time-of-flight spreading during the transit of ions from the target to the wall.

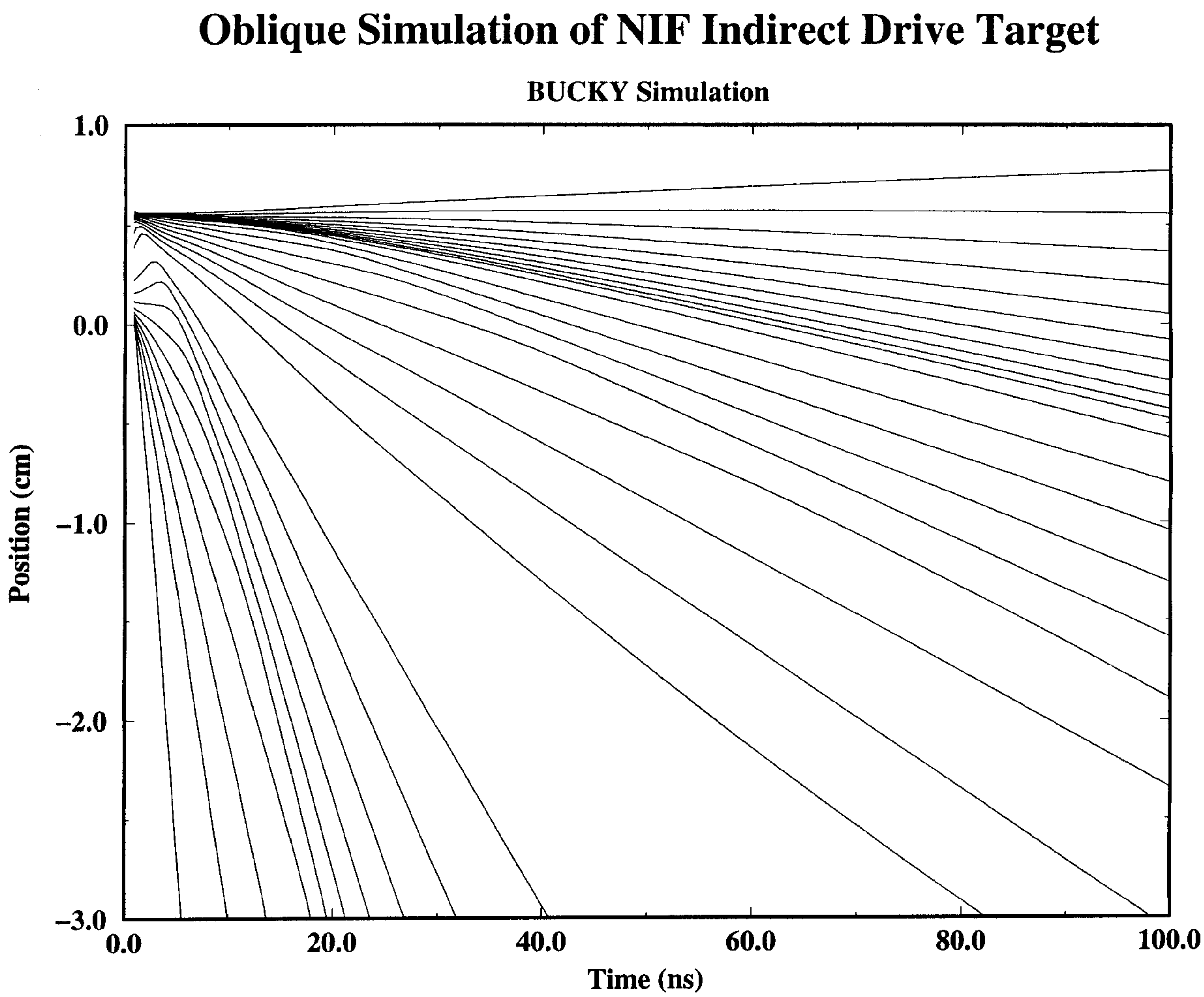

Figure 2.13. BUCKY simulation of the behavior of the NIF indirect drive target in the direction from the inside of the case out through the laser entrance hole. The positions of Lagrangian zone boundaries are plotted against time

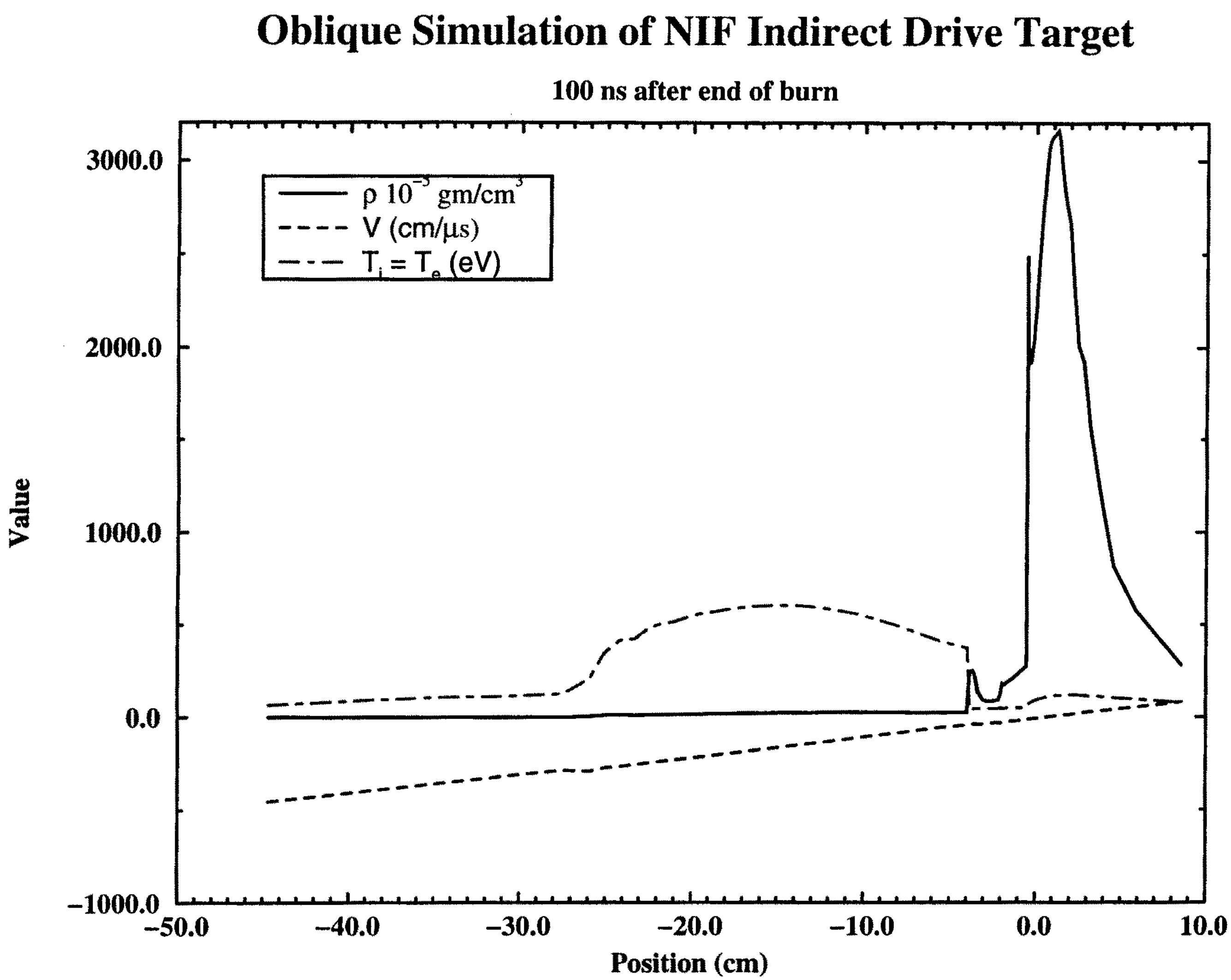

Figure 2.14. BUCKY simulation of the behavior of the NIF indirect drive target in the direction from the inside of the case out through the laser entrance hole. Profiles of mass density, fluid velocity, and ion temperature are plotted against distance along the oblique direction.

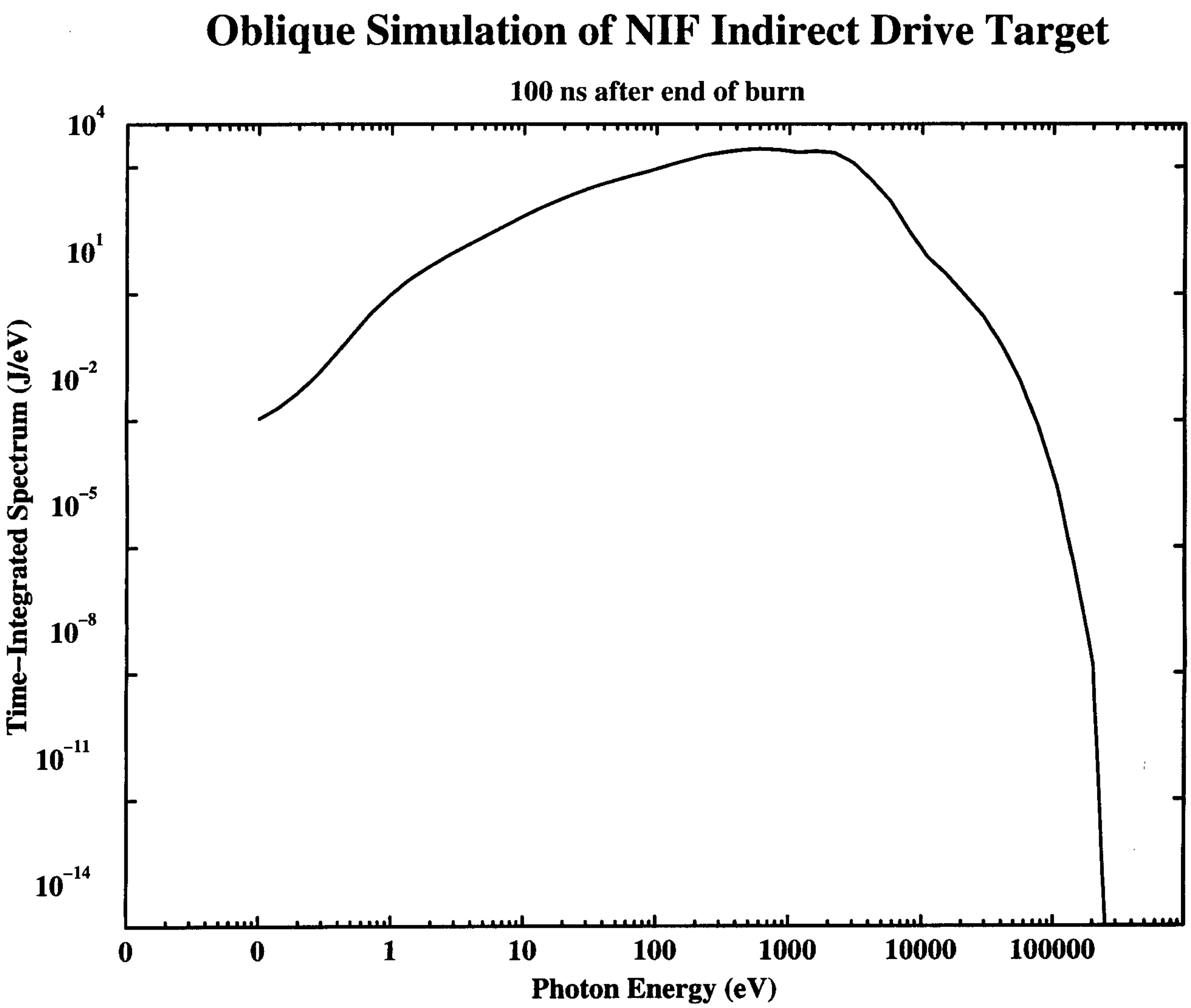

Figure 2.15. BUCKY simulation of the behavior of the NIF indirect drive target in the direction from the inside of the case out through the laser entrance hole. The time intergrated spectrum is shown integrated out to 100 ns for the radiation coming out the back of the laser entrance hole.

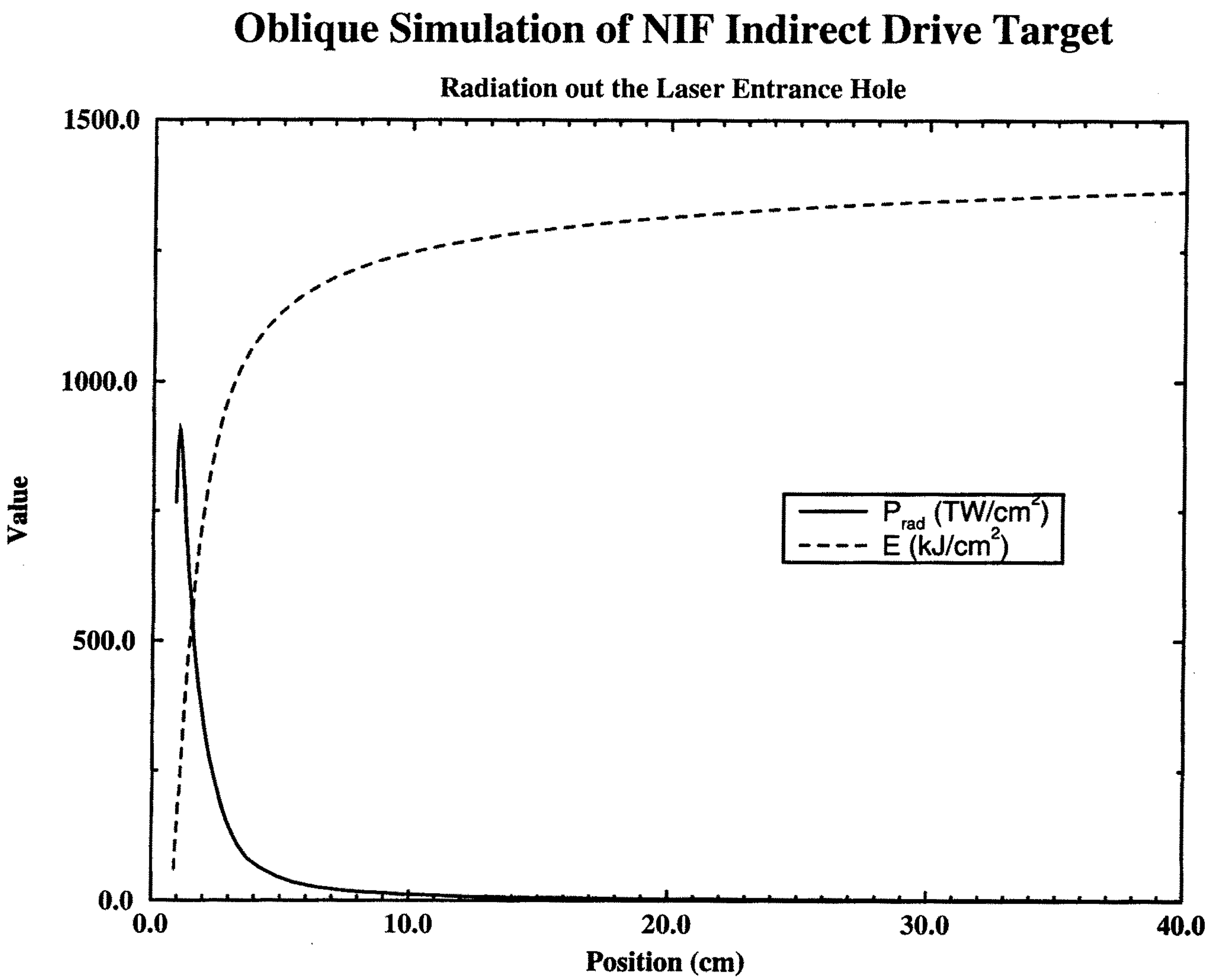

Figure 2.16. BUCKY simulation of the behavior of the NIF indirect drive target in the direction from the inside of the case out through the laser entrance hole. The radiant power and fluence are plotted against time.

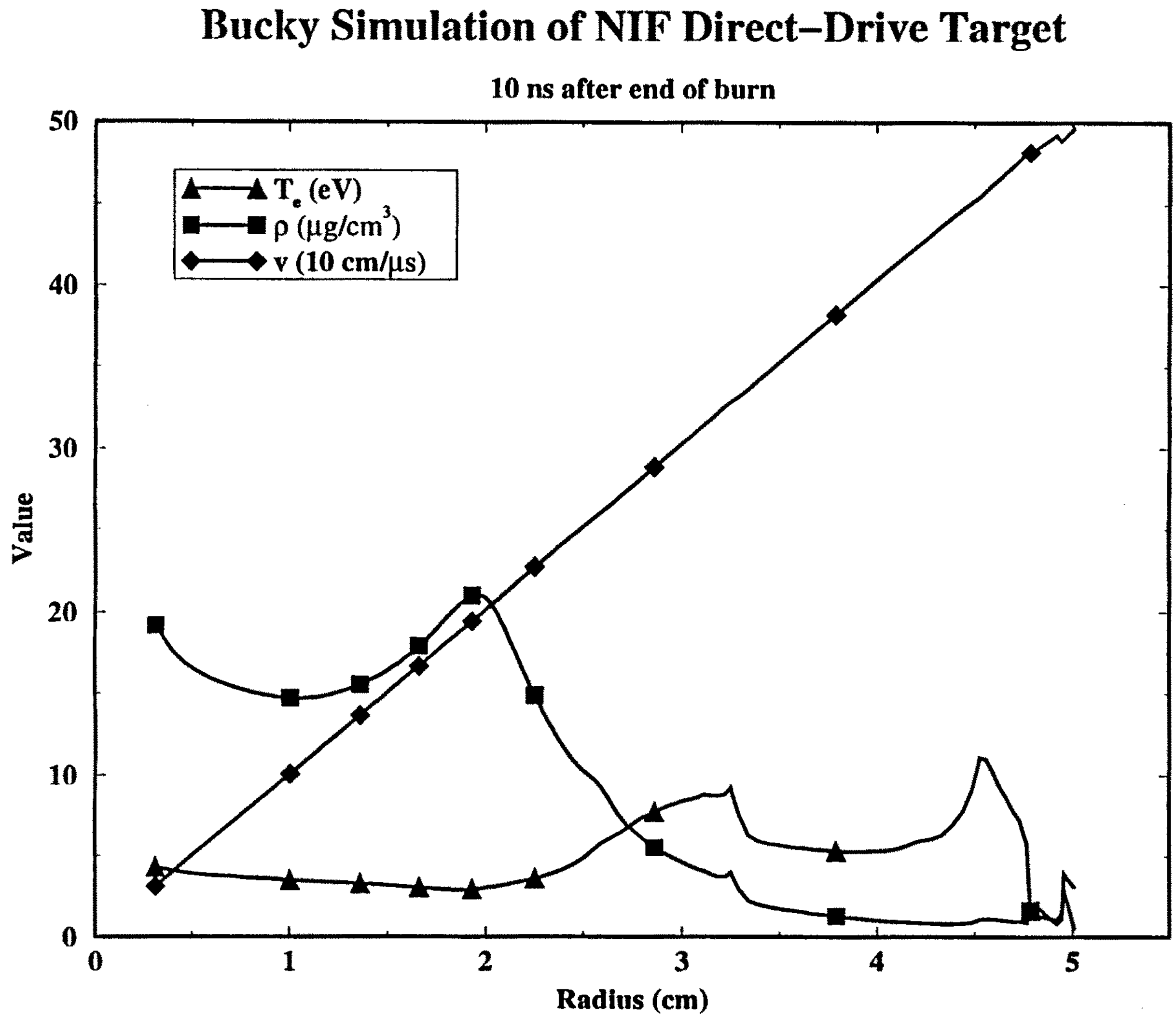

Figure 2.17. BUCKY simulation of the behavior of the NIF direct drive target. The velocity, mass density and plasma temperature are plotted against distance from the center of the target.

Table 2.1. Direct Drive Target Debris Spectrum

Bin Number	1	2	3	4	5	6	7
Species	T	T	T	D	D	D	C
Velocity (cm/ns)	0.13	0.20	0.27	0.13	0.20	0.27	0.5
Energy (keV)	26.4	62.5	114	17.6	41.7	76	3130
Number of ions ($\times 10^{19}$)	4.77	12.3	4.77	4.77	12.3	4.77	.452
Start of pulse at 5 m (μs)	3.03	2.13	1.67	3.03	2.13	1.67	.980
End of pulse at 5 m (μs)	5.00	3.03	2.13	5.00	3.03	2.13	1.02
Pulse width at 5 m (μs)	1.97	0.9	0.46	1.97	0.9	0.46	0.04
Pulse energy (MJ)	0.202	1.30	0.871	0.135	0.865	0.58	2.26
Power (TW)	0.103	1.44	1.89	0.069	0.961	1.26	56.5

The deuterium and tritium bins have particle energies in the few 10's of keV range and μs pulse widths, while the carbon bin contains 3.13 MeV with a 40 ns pulse width. The carbon bin contains by far the largest pulse energy and power. These results could be more accurate with a larger number of bins, but we need to improve our method of converting Figure 2.17 into the information in Table 2.1. The results using this discrete spectrum will give representative results, but not the final answer.

2.3. Comparison of Direct and Indirect Drive

During the summer of 1995 a series of Lasnex calculations was performed at and supported by Los Alamos National Laboratory to simulate the performance of direct and indirect drive NIF targets. Because of the relevance of these calculations to the NIF work discussed in this report, these results are summarized here. Details of these simulations will not be discussed. The energy balance of direct and indirect drive NIF targets are compared in Table 2.2. Two types of direct drive targets are shown; one of pure DT and one with an outer plastic coating. Two indirect drive targets are also shown; one that barely ignited and one that experienced significant burn. The two direct drive targets performed in a very similar way. The direct drive x-rays were all very hard (1.8 keV blackbody spectrum), though only 1% of the yield was in x rays. 19% of the direct drive yield was in debris and the rest in neutrons. The low fraction of energy in x rays is because most of the target is fully ionized after the end of the burn, so Bremsstrahlung is the dominant radiative emission process. The indirect drive targets have much larger fraction of energy in x rays because the debris energy coming out of the capsule is converted into x rays by the collision between the capsule debris and the hohlraum case. The indirect drive spectra, shown in Figures 2.18,

Table 2.2. Target Energy Balance

	Direct Drive		Indirect Drive	
	Pure DT	CH Coated	Ignited	Significant Yield
E_{laser}	1.26	1.27	1.31	1.33
TN yield (MJ)	38.6	39.7	0.11	9.40
Neutron losses (MJ)	32.4	33.1	0.08	7.12
X-ray losses (MJ)	0.38	0.40	0.45	1.98
Debris energy (MJ)	7.04	7.44	0.89	1.63
Maximum total energy (MJ)	39.8	41.0	1.42	10.73

2.19, and 2.20 are much cooler than the direct drive spectra because the stagnation region between the capsule and case is much cooler than the DT core during burn. The spectra and the fluence is very angle dependent. The x-rays are mostly emitted from the stagnant gold plasma inside the hohlraum. The fact that some emission is seen even 90% off of the hohlraum axis is due to some of the hot gold plasma inside the case moving through the laser entrance holes. This angle dependence is a major difference between the direct and indirect drive NIF targets.

3. NIF Wall Response to Target Emissions

3.1. Vaporization and Melting of Wall

The vaporization and melting of the NIF target chamber first wall has been calculated with the BUCKY code. Target x-rays and debris parameters from the BUCKY calculations presented above are used as inputs for these calculations. There were three materials considered: boron, Al_2O_3, and SiO_2. Direct and indirect drive spectra were considered. The energy partitioning and spectra are quite different, as shown in Table 2.2 and Figures 2.7, 2.11, and 2.15. The direct drive spectrum is much harder and much more energy from the direct drive target is in debris.

In these calculations, the BUCKY code deposits the x-ray and debris energy in the material and then uses the local energy density to determine whether the material is vaporized or melted. Both forms of energy are deposited in a time-dependent manner, which competes with the conduction of heat away from the surface. This results in a temperature profile as shown in Figure 3.1 for SiO_2 in the path of debris from a 40 MJ direct drive target. The material that is above the melting temperature is assumed melted.

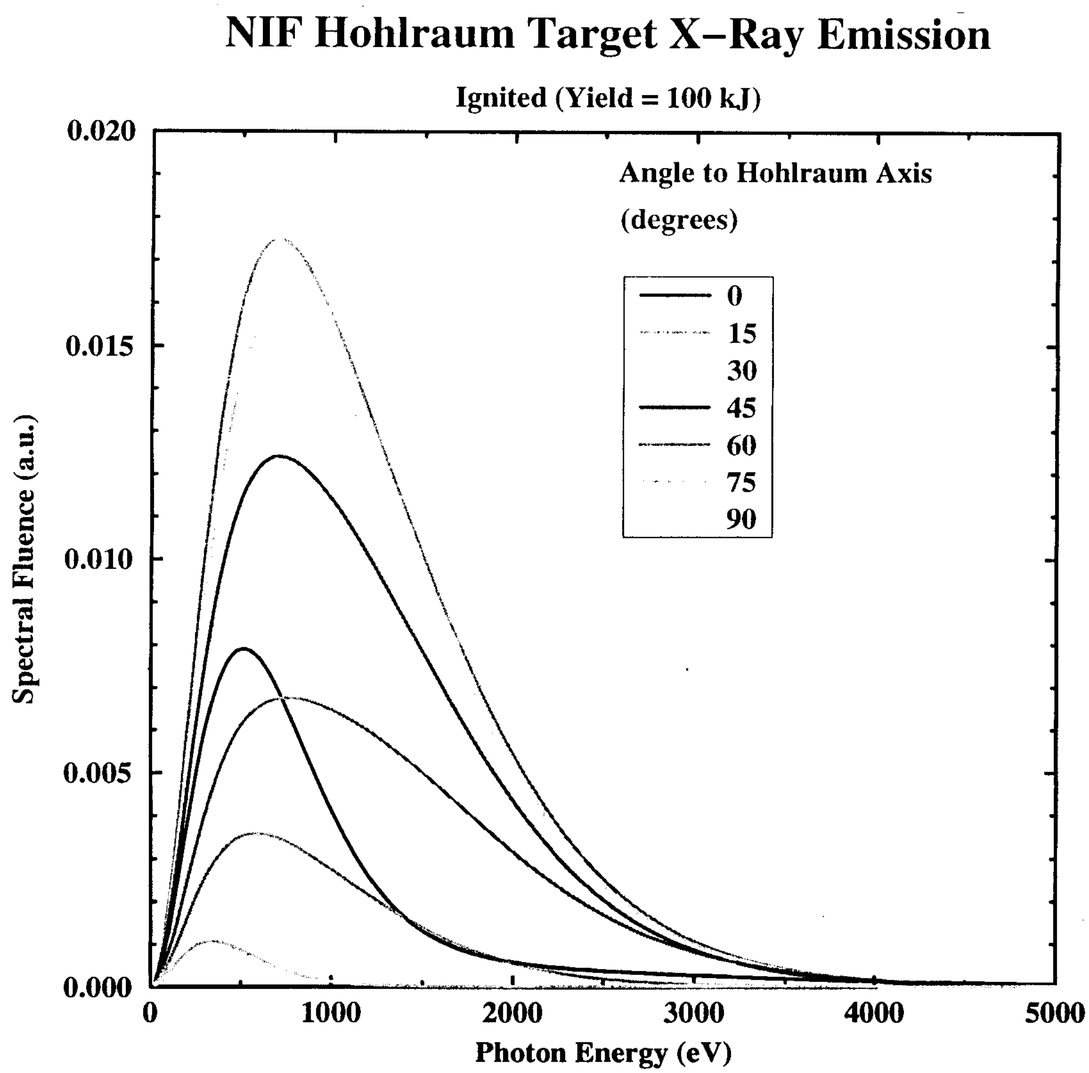

Figure 2.18. Angle dependent scaled x-ray spectrum of the barely ignited NIF indirect drive target. Calculation performed at LANL with Lasnex and TDG. Spectra are the sum of 3 blackbody spectra.

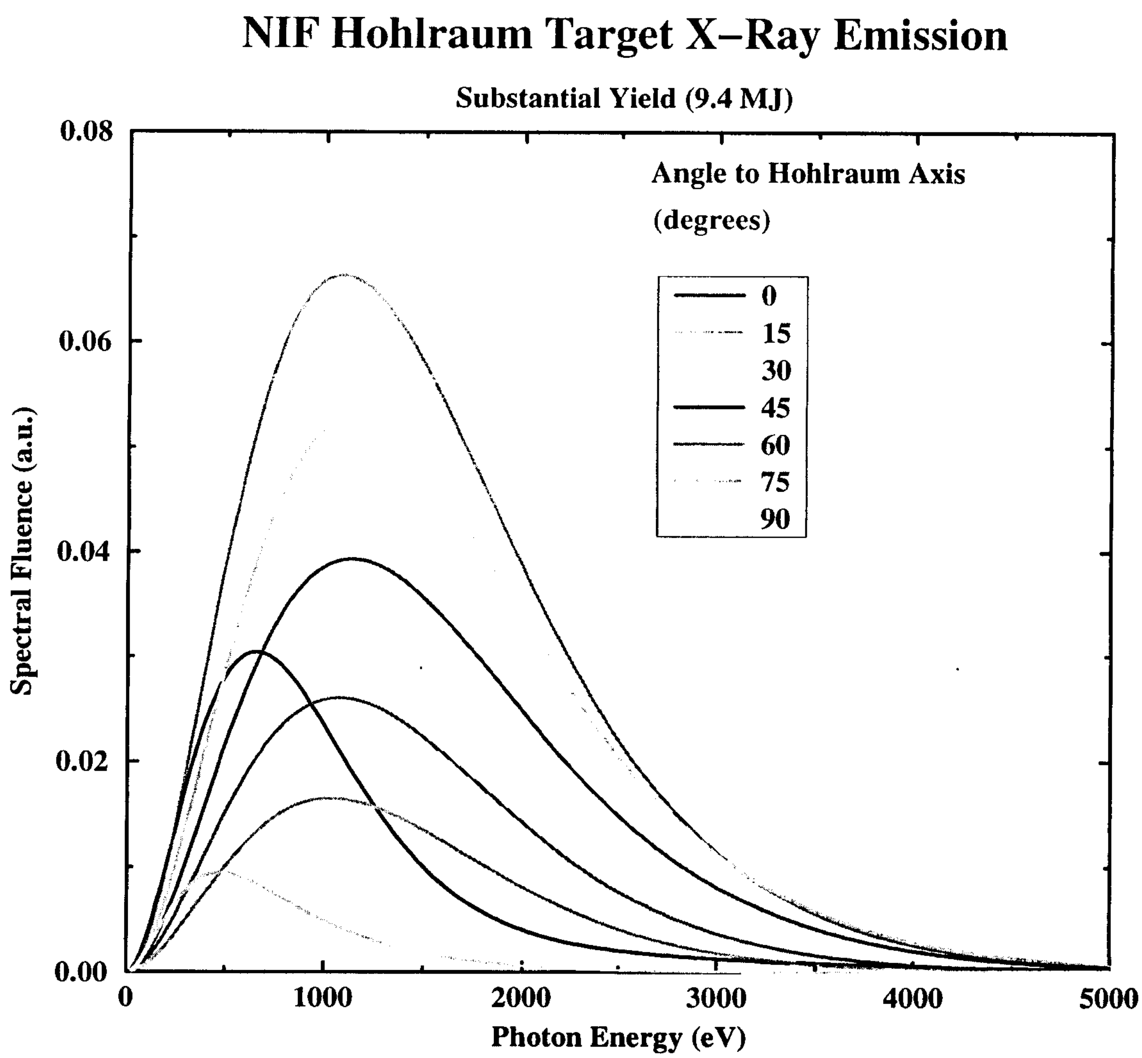

Figure 2.19. Angle dependent scaled x-ray spectrum of the NIF indirect drive target with significant yield. Calculation performed at LANL with Lasnex and TDG. Spectra are the sum of 3 blackbody spectra.

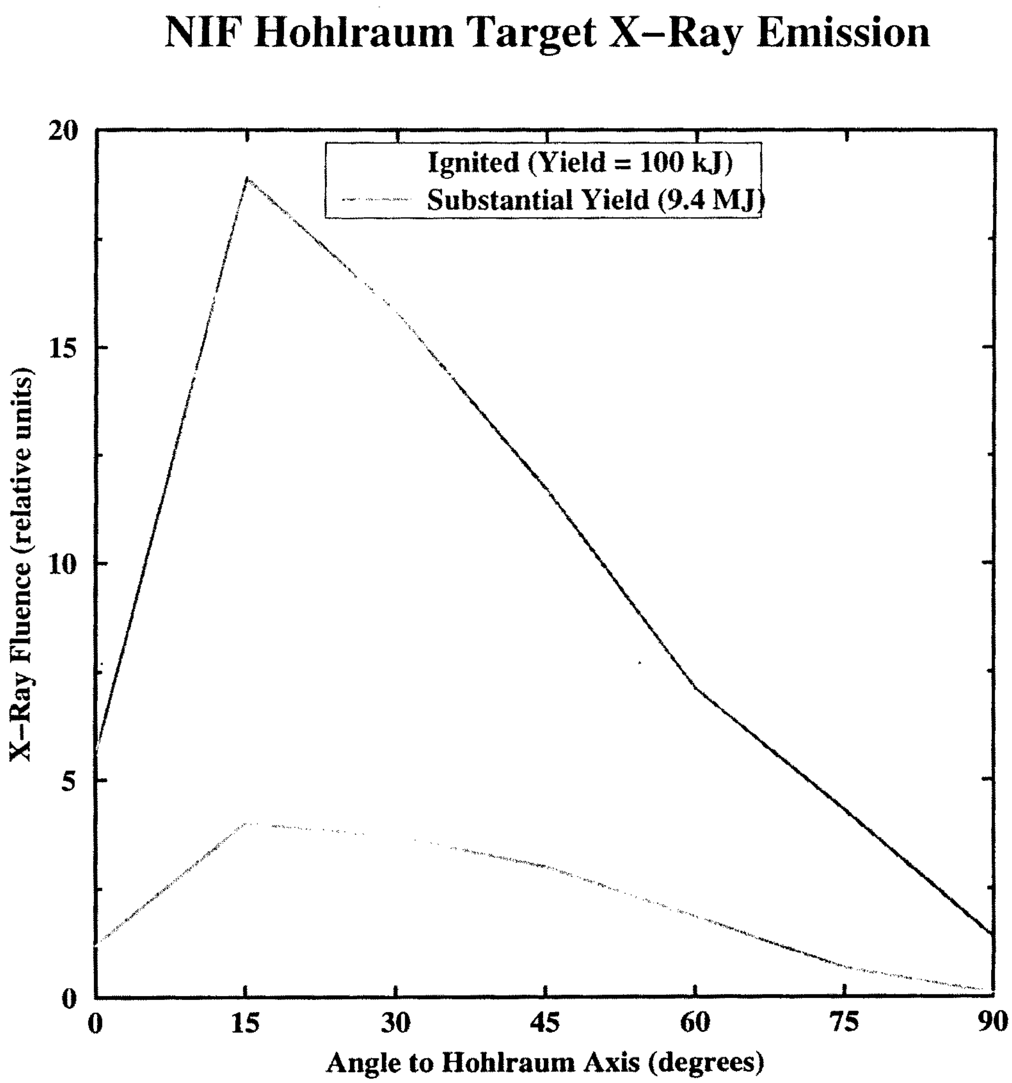

Figure 2.20. Angle dependent scaled x-ray fluence of the barely ignited and significant yield NIF indirect drive target. Calculation performed at LANL with Lasnex and TDG.

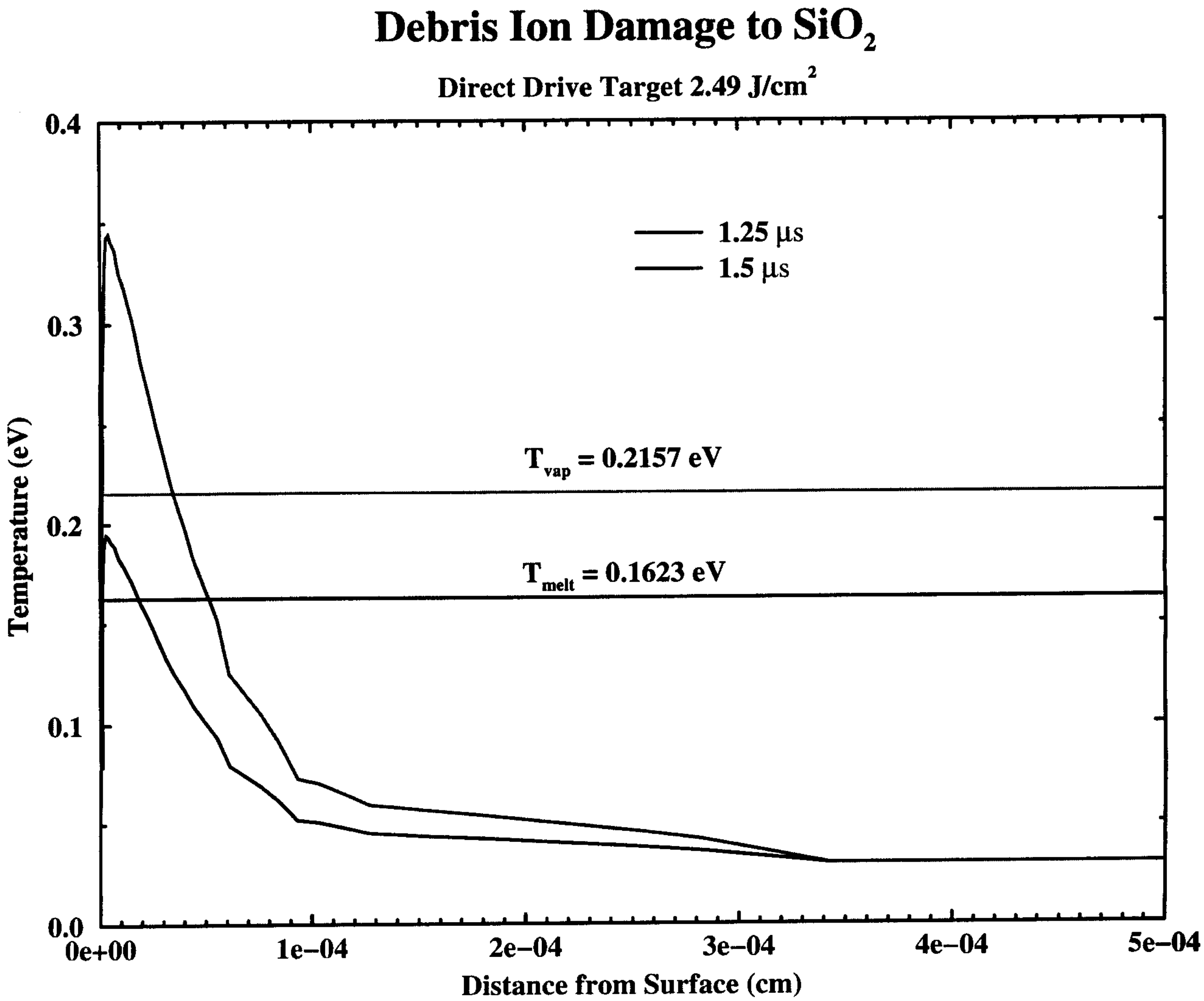

Figure 3.1. Temperature profiles in SiO_2 in the path of debris from a 40 MJ direct drive target at two times after the end of target burn.

Table 3.1. Wall Damage by Indirect Drive Target X Rays

	B			Al_2O_3		
Target Yield (MJ)	0.1	20	45	0.1	20	45
CASE SPECTRUM						
X-Ray Fluence (J/cm^2)	0.281	0.905	1.684	0.281	0.905	1.684
Debris Fluence (J/cm^2)	0.292	0.942	1.753	0.292	0.942	1.753
Vaporized Mass (mg/cm^2)	0	0	0	0	0	0.0098
Vaporized Thickness (μm)	0	0	0	0	0	0.025
Melted Mass (mg/cm^2)	0	0	0	0	0	0.098
Melted Thickness (μm)	0	0	0	0	0	0.25
OBLIQUE SPECTRUM						
X-Ray Fluence (J/cm^2)	0.258	0.831	1.547	0.258	0.831	1.547
Debris Fluence (J/cm^2)	0.315	1.015	1.891	0.315	1.015	1.891
Vaporized Mass (mg/cm^2)	0	0	0	0	0	0
Vaporized Thickness (μm)	0	0	0	0	0	0
Melted Mass (mg/cm^2)	0	0	0	0	0	0.051
Melted Thickness (μm)	0	0	0	0	0	0.13

The heat of fusion is ignored. Material is evaporated from the surface of the material at a rate determined by the surface temperature.

No melting or vaporization was seen on boron or Al_2O_3 from the radiation from the base of the case or the oblique radiation from a 20 MJ indirect drive target. The response of SiO_2 to this radiation and debris has not been studied. A parametric study of the response of boron and Al_2O_3 as a function of target yield has been performed. The results are given in Table 3.1. Boron experiences no vaporization or melting for either x-ray spectrum up to a target yield of at least 45 MJ. Al_2O_3 is not damaged at either 100 kJ or 20 MJ yield for either spectrum, but is slightly melted at a 45 MJ yield. Therefore, these calculations show that boron is a marginally better first wall coating material, from the point of view of x-ray vaporization by indirect drive NIF targets.

The target debris from direct drive targets does some damage to the target chamber materials. The target x-ray fluence is much lower than the debris fluence and the x-ray spectrum is hard enough that the deposition length is long in the chamber materials so the specific energy in the material is relatively low. Neglecting the effects of x rays, the melting and vaporization caused by the debris from a 40 MJ plastic coated direct drive target has been calculated with BUCKY, using the debris spectrum discussed above. The results are

Table 3.2. Wall Damage by 40 MJ Direct Drive Target Debris

	B	Al_2O_3	SiO_2
Vaporized Mass (mg/cm^2)	0	0.0035	0.079
Vaporized Thickness (μm)	0	0.009	0.35
Melted Mass (mg/cm^2)	0	0.29	0.12
Melted Thickness (μm)	0	0.75	0.55

sumarized in Table 3.2. Here, boron is clearly superior to Al_2O_3. Also, the debris shield, which is made of SiO_2, will be damaged by a full yield direct drive target.

3.2. Tritium Deposition in NIF Target Chamber Walls

The deposition of tritium ions in carbon, boron, alumina and glass has been calculated with the BUCKY code. At the time the calculations were performed, only a discrete spectrum was available for the NIF targets. In the future, calculations with continuous ion spectra will be performed. The discrete spectra are enough to give a rough indication of how deeply the ions penetrate into the materials.

BUCKY considers the effects of free electron, bound electrons and target nuclei in the calculation of ion stopping. The traditional approach in BUCKY has been to divide the contributions from free and bound electrons and treat them separately. In the calculations presented in this section, this approach is used. In this work, free electrons in the stopping medium are not important because the medium never gets hot enough to do much ionization. The bound electron contribution is calculated in two ways, depending on the ion energy. At low energy, the Lindhard-Scharff [5] model is used. Here, the stopping power is calculated as,

$$\left(\frac{dE}{dx}\right)_{LS} = (3.84 \times 10^{18}\,\text{keV cm}^{-1}) N_2 \frac{Z_1^{7/6} Z_2^*}{[Z_1^{2/3} + (Z_2^*)^{2/3}]^{3/2}} \left(\frac{E_1}{A_1}\right)^{1/2} . \qquad (1)$$

Here, Z_1, E_1, and A_1 are respectively the atomic number, energy in keV, and atomic mass of the projectile ions. Z_2^* is the average number of bound electrons per atom in the stopping medium. This expression is valid when the velocity of the projectile ions is small compared to the orbital velocities of the bound electrons in the stopping medium. Here the stopping power is proportional to the projectile ion velocity. This expression derives from the treatment of the electrons in the stopping medium as a cloud.

When the velocity of the projectile ions is greater than the orbital velocities of electrons in the stopping medium, BUCKY uses the Bethe [6] stopping power;

$$\left(\frac{dE}{dx}\right)_{\text{Bethe}} = \left(\frac{\omega_p q_1 e}{v_1}\right)^2 \left[\ln\left(\frac{2m_e v_1^2}{<\Phi_2> (1 - v_1^2/c^2)}\right) - \frac{v_1}{c}\right] . \tag{2}$$

Here, ω_p and $<\Phi_2>$ are the electron plasma frequency and the average ionization potential in the stopping medium. q_1 and v_1 are the projectile ion charge state and velocity. The Bethe model treats the bound electrons in the stopping medium as point charges. In this expression, the stopping power decreases with increasing projectile velocity.

Since the Lindhard model predicts increasing stopping power at low ion energy and the Bethe model predicts a falling stopping power at high ion energies, a maximum exists in the interface between the regions of validity of the two models. This is when the projectile ion velocity is approximately equal to the orbital velocity of the bound electrons is the stopping medium. BUCKY does a linear interpolation between these two methods in this regime. A new feature in BUCKY allows a more general calculation of the stopping power, where the interaction of bound electrons in a muffin-tin potential are explicitly calculated [7]. This gives the same results as the Lindhard model at low ion energies and the Bethe model at high energy, but it is a better approach in this intermediate region. The range calculated with the old model is compared with calculations from the TRIM [8] code that uses fits to experimental data, which will be discussed in a later section of this report.

In these calculations, the charge state of the tritium ions is assumed to be constant at 1.0. BUCKY has the ability to calculate the time dependent in-flight charge state of the projectile ions. This is an important effect for high atomic number projectiles, though hydrogen is a trivial case.

The results of the BUCKY tritium deposition calculations are shown in Figures 3.2 through 3.9. BUCKY has been modified to record the positions where ions deposit in the solid materials. The density of tritium ions is plotted against distance into the material in arbitrary units. The calculations were performed for discrete ion energies, so the ions stop at discrete positions. In reality, the ions will continuously deposit. The plots shown here give an indication of the maximum and minimum deposition lengths. The input parameters for these simulations are summarized in Table 3.3. The results are summarized in Table 3.4, for a direct drive target with a yield of 40 MJ, and in Table 3.5, for a direct drive target with a yield of 0.1 MJ. In all cases, the same total number of tritium atoms is assumed to be the same. For the 40 MJ NIF direct drive target, the profiles of velocity and mass density, shown in Figure 2.17, have allowed the choice of three discrete tritium energies. The relative numbers of ions at each energy are determined by these profiles.

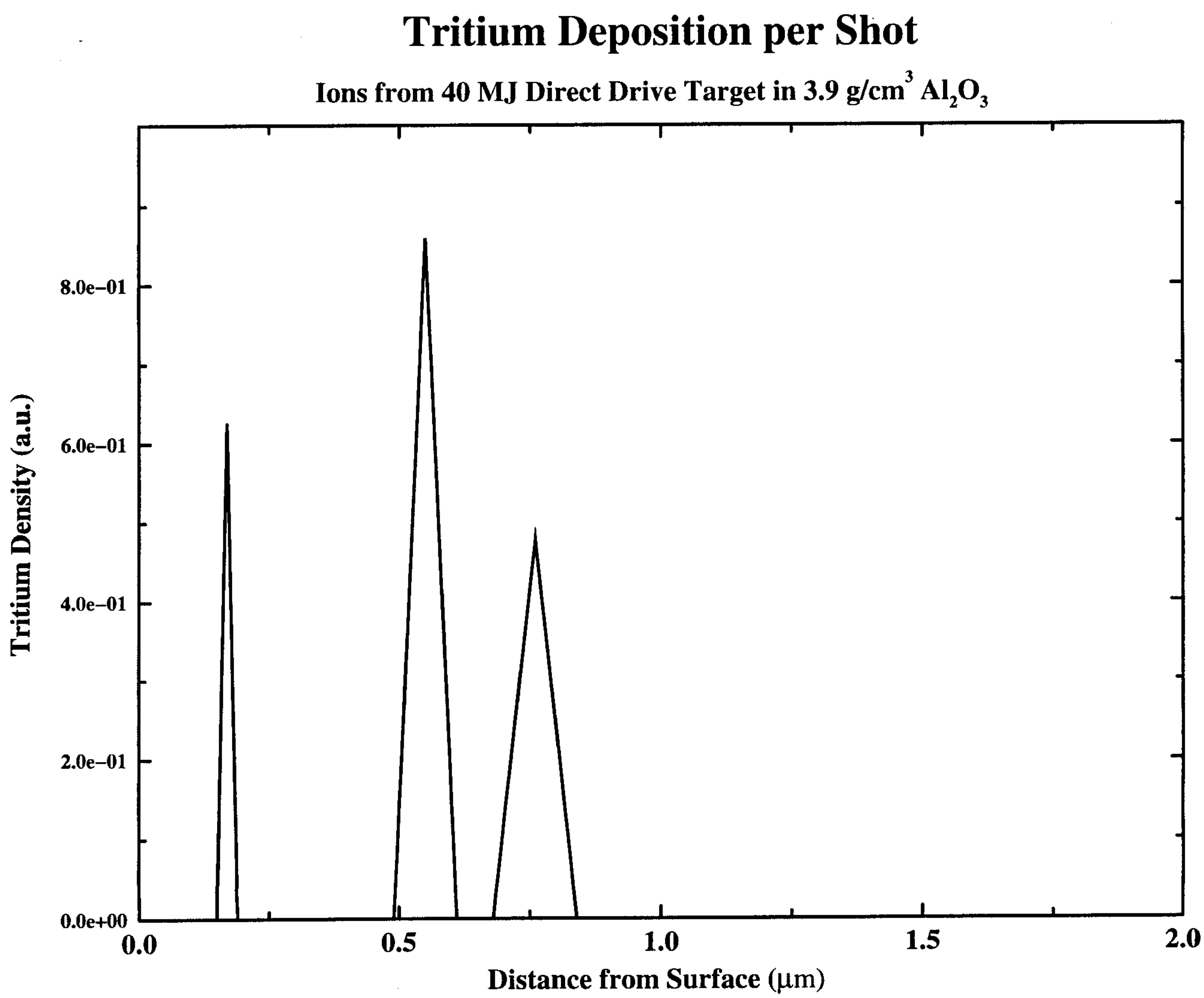

Figure 3.2. BUCKY simulation of the deposition of tritium from a 40 MJ direct drive NIF target into 3.9 g/cm^{-3} Al_2O_3. The tritium spectrum is discrete (26.4 keV, 62.5 keV and 114 keV), estimated from the velocity and density profiles.

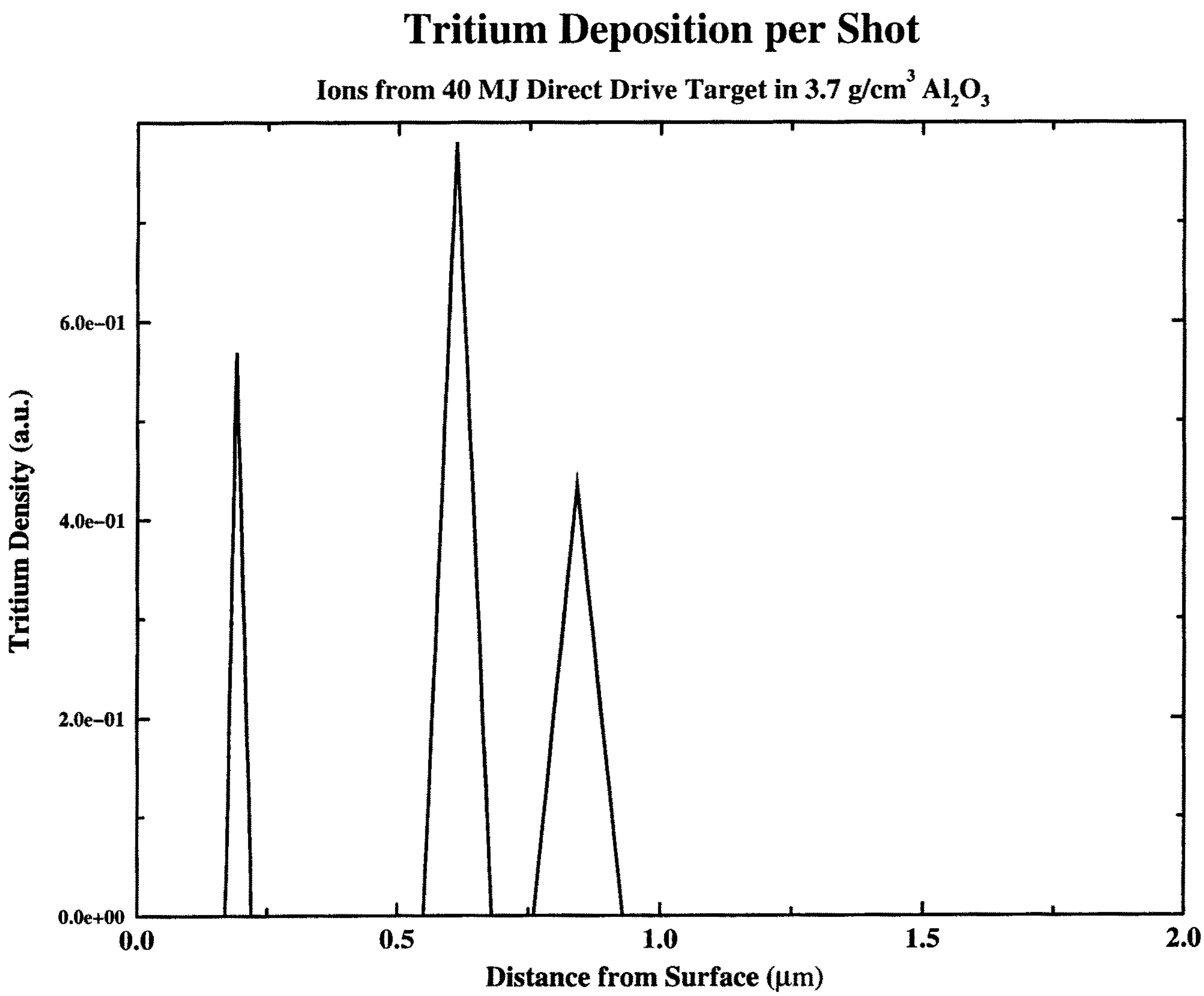

Figure 3.3. BUCKY simulation of the deposition of tritium from a 40 MJ direct drive NIF target into 3.7 g/cm^{-3} Al_2O_3. The tritium spectrum is discrete (26.4 keV, 62.5 keV and 114 keV), estimated from the velocity and density profiles.

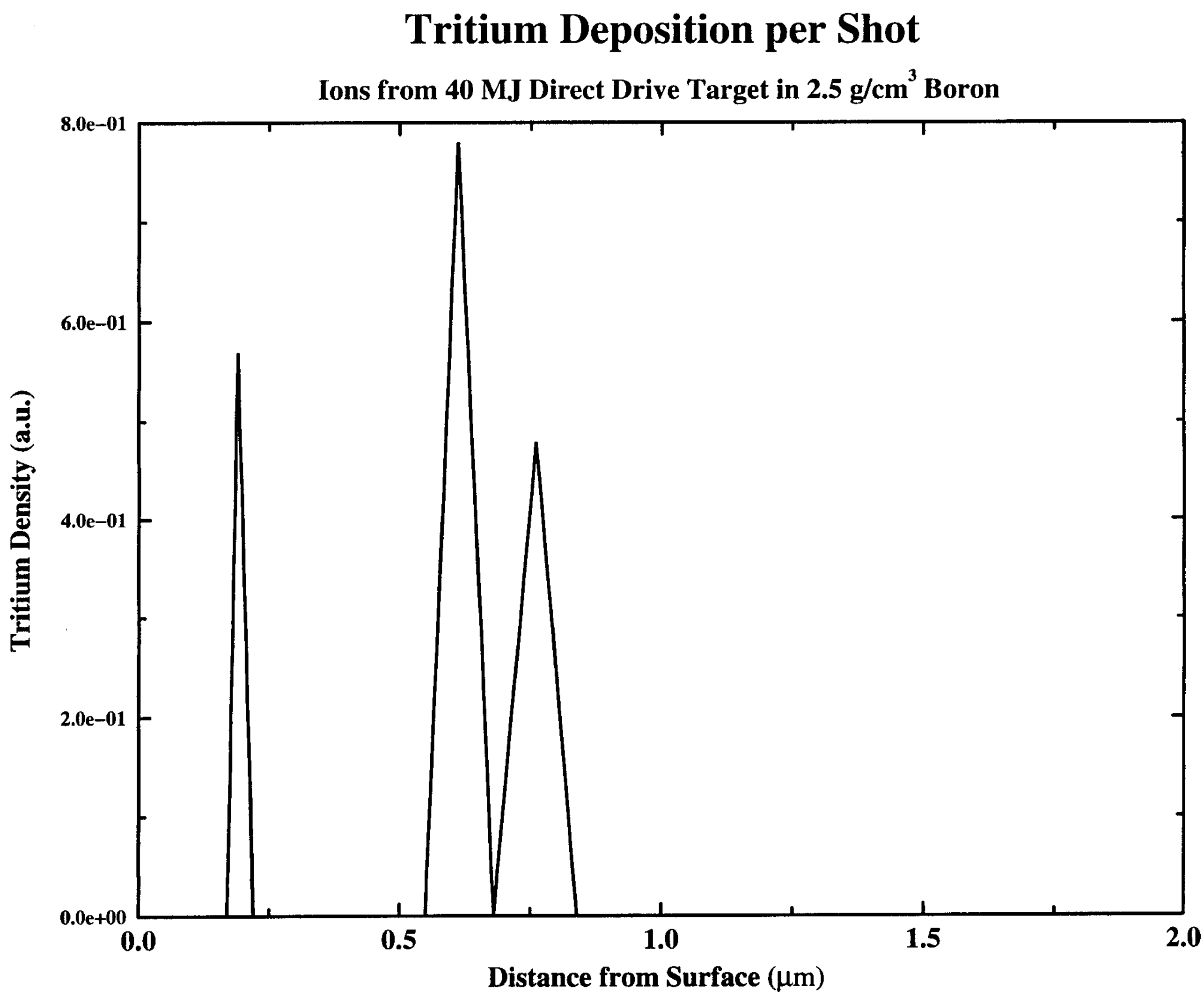

Figure 3.4. BUCKY simulation of the deposition of tritium from a 40 MJ direct drive NIF target into 2.5 g/cm^{-3} boron. The tritium spectrum is discrete (26.4 keV, 62.5 keV and 114 keV), estimated from the velocity and density profiles.

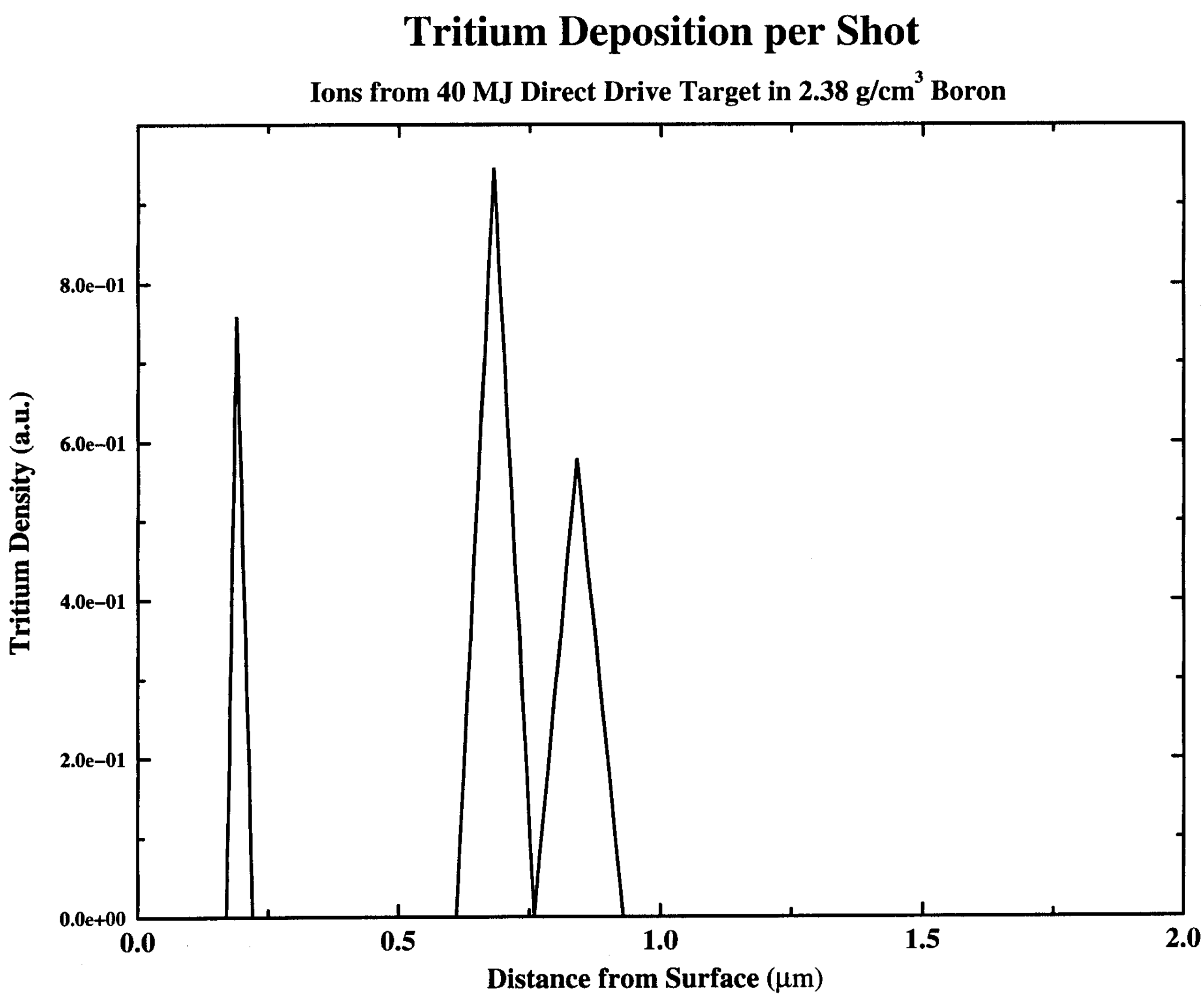

Figure 3.5. BUCKY simulation of the deposition of tritium from a 40 MJ direct drive NIF target into 2.38 g/cm^{-3} boron. The tritium spectrum is discrete (26.4 keV, 62.5 keV and 114 keV), estimated from the velocity and density profiles.

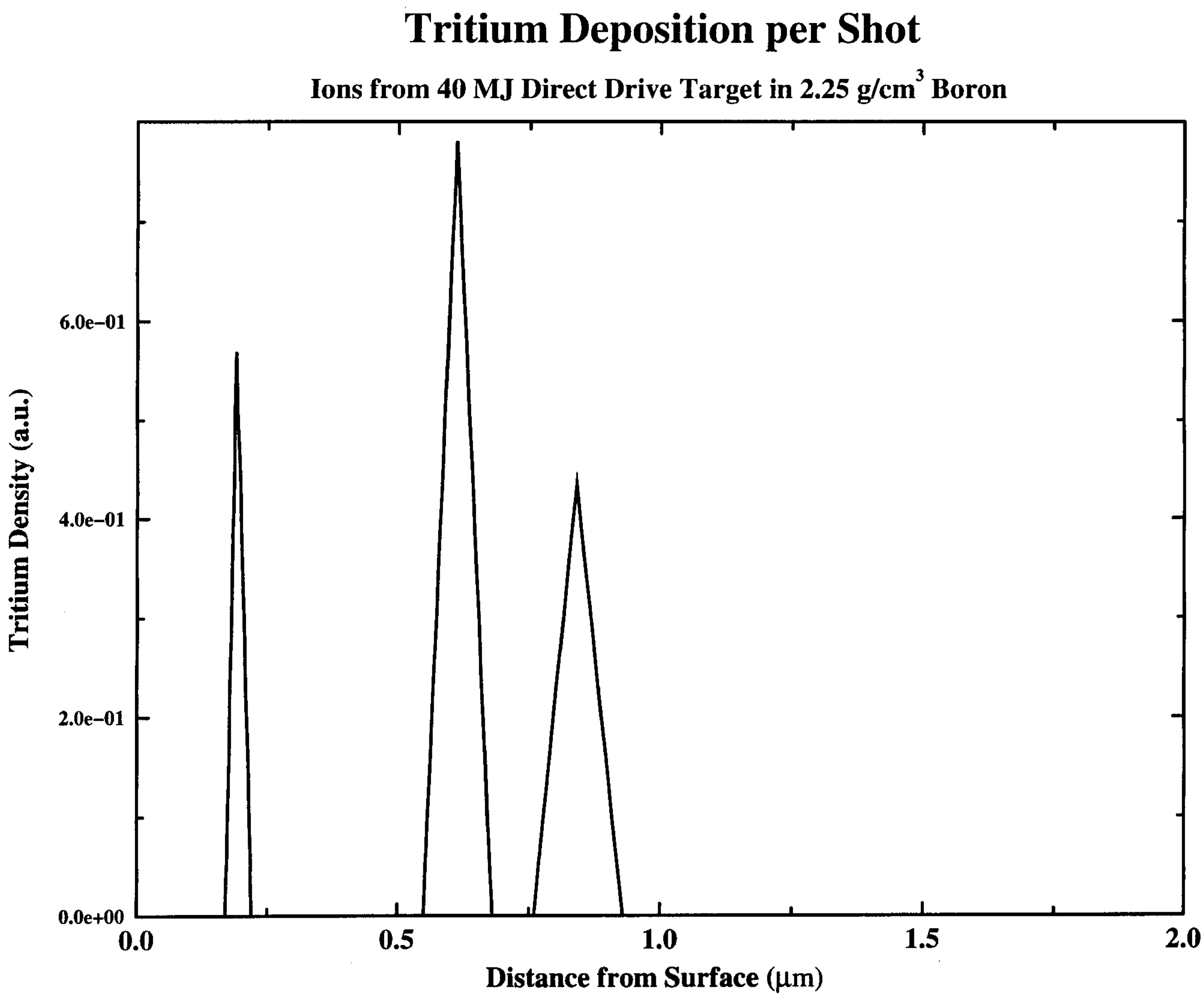

Figure 3.6. BUCKY simulation of the deposition of tritium from a 40 MJ direct drive NIF target into 2.25 g/cm^{-3} boron. The tritium spectrum is discrete (26.4 keV, 62.5 keV and 114 keV), estimated from the velocity and density profiles.

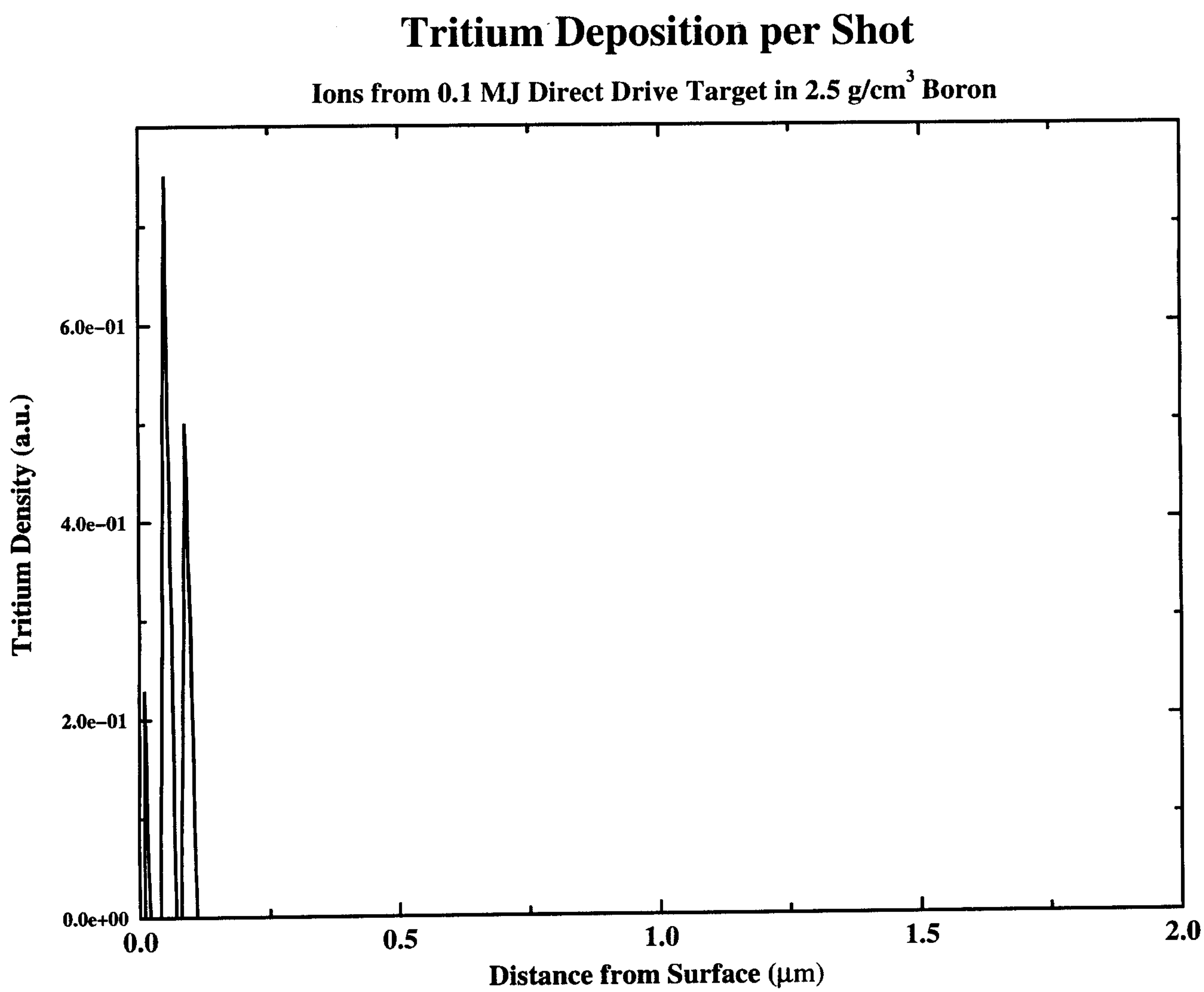

Figure 3.7. BUCKY simulation of the deposition of tritium from a 0.1 MJ direct drive NIF target into 2.5 g/cm^{-3} boron. The tritium spectrum is discrete (0.895 keV, 2.12 keV and 3.86 keV), estimated by assuming the same number of particles as in a 40 MJ yield, but reducing the energy per particle appropriately.

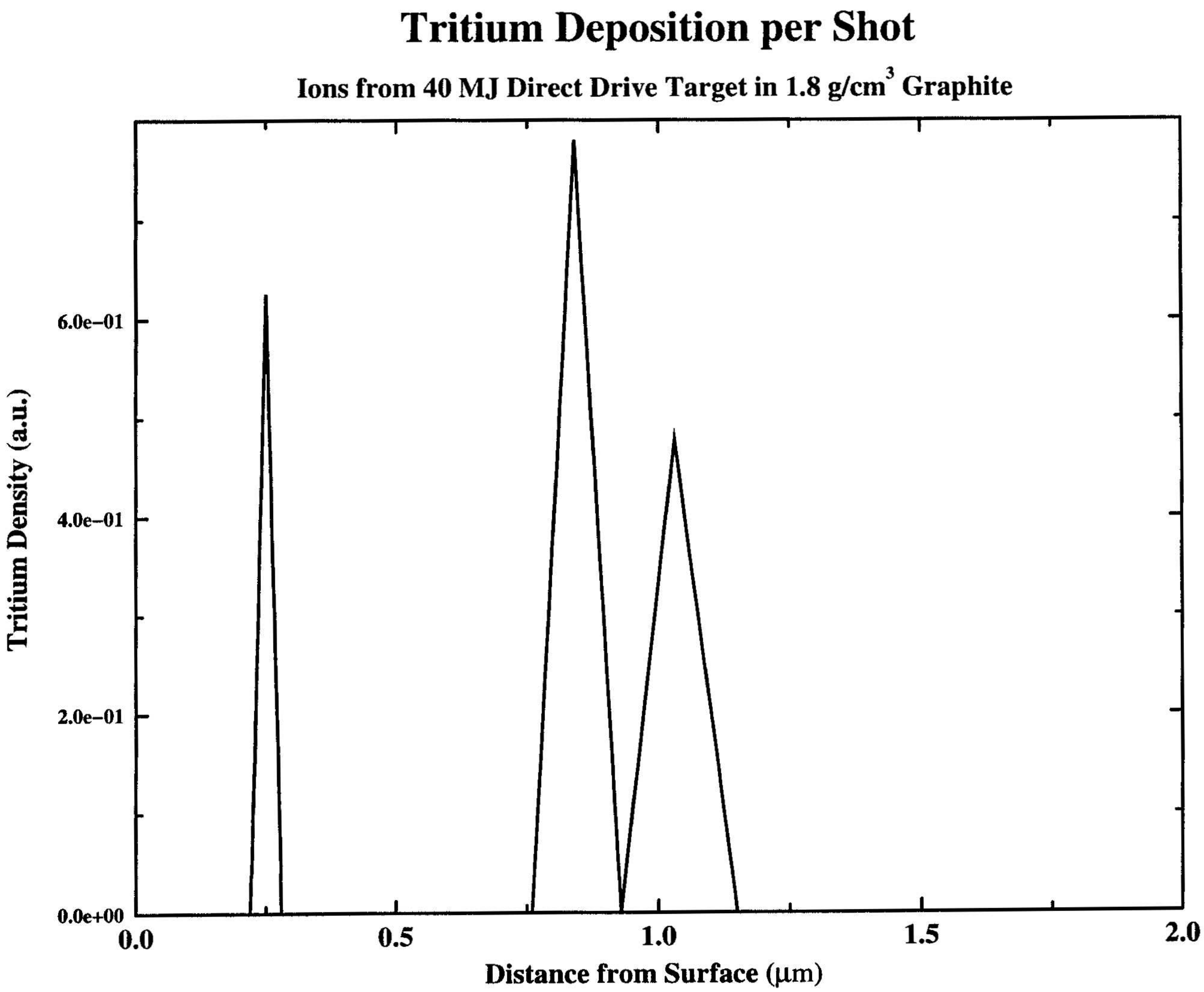

Figure 3.8. BUCKY simulation of the deposition of tritium from a 40 MJ direct drive NIF target into 1.8 g/cm^{-3} graphite. The tritium spectrum is discrete (26.4 keV, 62.5 keV and 114 keV), estimated from the velocity and density profiles.

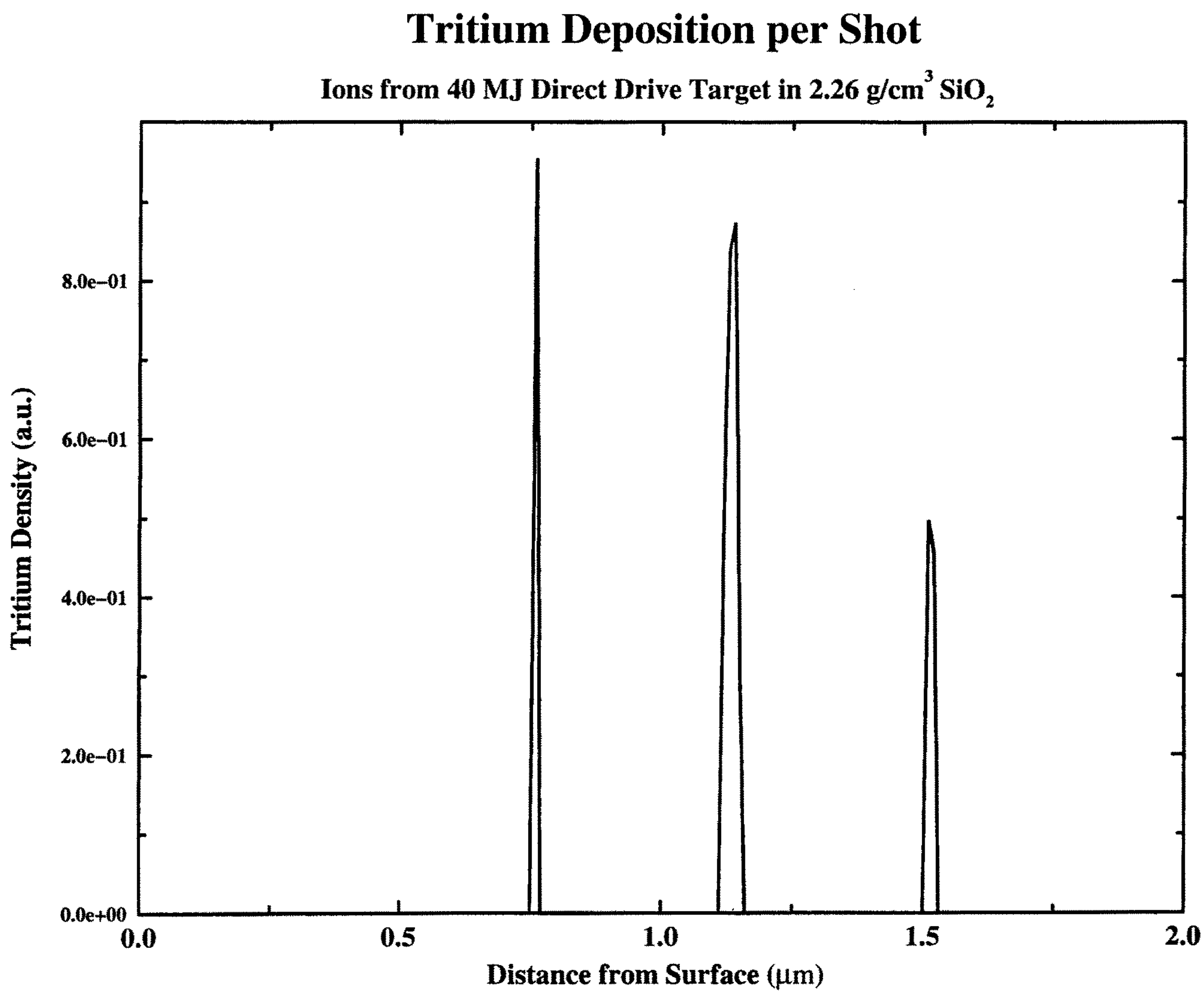

Figure 3.9. BUCKY simulation of the deposition of tritium from a 40 MJ direct drive NIF target into 3.9 g/cm^{-3} SiO_2. The tritium spectrum is discrete (26.4 keV, 62.5 keV and 114 keV), estimated from the velocity and density profiles.

Table 3.3. Tritium Deposition Parameters

First wall radius (m)	5
Total number of tritium atoms	2.25×10^{20}
Column density of tritium on wall (cm^{-2})	7.16×10^{13}
Ion energy #1 (keV)	26.4
Number of ions at energy #1	4.77×10^{19}
Ion energy #2 (keV)	62.5
Number of ions at energy #2	1.30×10^{20}
Ion energy #3 (keV)	114
Number of ions at energy #3	4.77×10^{19}

Table 3.4. Tritium Deposition Results for 40 MJ Direct Drive Target

Ion Energy (keV)	26.4	62.5	114
Al_2O_3			
Range for 3.9 g/cm^3 (μm)	0.20	0.55	0.75
Average tritium density (cm^{-3})		1.3×10^{18}	
Range for 3.7 g/cm^3 (μm)	0.22	0.60	0.82
Average tritium density (cm^{-3})		1.2×10^{18}	
Boron			
Range for 2.5 g/cm^3 (μm)	0.20	0.60	0.75
Average tritium density (cm^{-3})		1.3×10^{18}	
Range for 2.38 g/cm^3 (μm)	0.21	0.63	0.80
Average tritium density (cm^{-3})		1.2×10^{18}	
Range for 2.25 g/cm^3 (μm)	0.22	0.66	0.82
Average tritium density (cm^{-3})		1.2×10^{18}	
Graphite			
Range for 1.8 g/cm^3 (μm)	0.20	0.70	0.95
Average tritium density (cm^{-3})		9.5×10^{17}	
SiO_2			
Range for 2.26 g/cm^3 (μm)	0.76	1.15	1.62
Average tritium density (cm^{-3})		8.3×10^{17}	

Table 3.5. Tritium Deposition Results for 0.1 MJ Direct Drive Target

Ion Energy (keV)	0.895	2.12	3.86
Range for 2.5 g/cm^3 boron (μm)	0.02	0.10	0.15
Average tritium density (cm^{-3})		5.5×10^{18}	

Calculations have been performed for direct drive targets only. The tritium ion debris spectra from indirect drive NIF targets can be no harder than the 40 MJ yield direct drive spectrum and is probably much softer. The indirect drive yield will be no higher than about 20 MJ and the total number of tritium atoms is comparable to the direct drive target, so the energy per tritium is less than or comparable to the direct drive target. In the indirect drive targets, most of the tritium ions will collide with the remnants of the hohlraum case, converting much of their energy into radiation. Those tritium ions pointed toward the laser entrance holes will lose some energy going through the cloud of gold vapor that has been blown off of the case. These effects will substantially reduce the tritium ion energies seen on the wall of the target chamber.

The results of these calculations indicate that for all of the materials studied, tritium will penetrate no more than about 2 μm into the material. From a single shot, about 10^{18} tritium atoms per cm^3 are added to the material. The actual profiles in the tritium density in the material need to be calculated as a continuous ion energy spectrum, which is suggested as future work. The glass in the debris shield experiences the deepest penetration, while the other materials all have very similar penetration distances. For the 0.1 MJ yield direct drive target, the tritium deposits within 0.2 μm for boron. Graphite and Al_2O_3 will have similar results.

3.3. Material Properties of Alumina Plasma Sprayed Coatings

It was reported at the workshop at Oak Ridge National Laboratory that plasma spray alumina consists of both the α and γ phases [9]. We were asked to consider what implications this might have for the first wall response to the target explosion. We have done a literature search into the properties of the two phases of alumina. The γ phase of alumina is transformed into the α phase at 750-1200°C. The material is usually heated to well above this level in transit from the plasma spray gun to the material surface, so the presence of the γ phase must be due to incomplete phase transition in the transit or rapid solidification on the material surfaces.

The material response to x rays and debris might not be sensitive to the phase of the alumina. SRI [9] has suggested that differences in the material properties would be seen in differences in the response of plasma sprayed and sintered alumina to their electron beam source. They say no difference, and they therefore believe that there is not a significant difference in material properties. They use α properties in their simulations.

We have tried to look further and find the properties of both phases of alumina. The most clear difference is in the structure. α is hexagonal and γ is cubic close-packed. The cubic structure is less compact, so γ-alumina is less dense and readily absorbs water and dissolves in acids [10]. The γ phase is actually several similar cubic phases. Some is known about the thermodynamic properties of γ-alumina [11], particularly the enthalpy of transition from α-alumina, which is -33 kJ/mol. This allows the calculation of the enthalpy of formation of γ-alumina as -1657 kJ/mol. The heat capacity of γ-alumina is 4.7 α-alumina. This is all the properties we have yet to find for γ-alumina. The unknown properties are assumed to be the same as for α-alumina, which is a very well known material.

4. Code Development

In the past year, there has been significant development to the BUCKY 1-D radiation-hydrodynamics code and the ZEUS 2-D radiation-hydrodynamics code. This includes both actual changes to the codes and verification and benchmarking. Additionally, a manual was written for the BUCKY code [1].

4.1. Testing of BUCKY Results

4.1.1. Ion Stopping

The ion stopping in BUCKY has been compared with the TRIM code [8]. The TRIM code uses fits to measured results to obtain range as a function of energy, while BUCKY is an ab initio calculation as discussed above. Also, TRIM does a 3-D Monte Carlo calculation of ion trajectories, including direction change scattering, while BUCKY assumes 1-D normal incidence ion trajectories and does a deterministic calculation. This means that TRIM can include the straggling effect, a spreading and shortening of the normal penetration distance because of transverse ion motion, while BUCKY cannot. The Monte Carlo method in TRIM would not be applicable to a radiation hydrodynamics code like BUCKY because it is a much less computer efficient way of doing the calculation. Also TRIM does not currently allow a spectrum of ion energies, while BUCKY does.

Table 4.1. Tritium Range in 1.8 g/cm^3 Graphite Calculated by TRIM and BUCKY

Ion Energy (keV)	26.4	62.5	114
BUCKY			
Range (μm)	0.20	0.70	0.95
TRIM			
Range (μm)	0.35	0.75	1.25
Straggling (μm)	0.07	0.07	0.07

Because of the very different methods used and to test the importance of straggling, comparing TRIM to BUCKY is a good test of BUCKY. The tritium density (in arbitrary units) of beams of three energies in graphite are shown in Figure 4.1. The BUCKY results are shown in Figure 3.8. The results are summarized in Table 4.1. There is some difference in the range calculated by the two codes. The most significant difference is at 114 keV, where the BUCKY calculation is 24% short. The straggling is about constant in energy, so it is much more important in short range deposition. For 114 keV, straggling is only about 5%. A spectrum of energies will evidently cause more spreading than straggling does.

4.1.2. Radiation Transport and Hydrodynamics

The radiation transport and hydrodynamics in the BUCKY code has been benchmarked by comparison with the HYADES code and with Nova experiments. The comparisons were suggested by Jon Larsen. BUCKY calculations were then performed by UW and the final comparisons were then done by Larsen. Two main issues were addressed; hydrodynamic motion and radiation transport. The details of the comparison have been reported by Larsen, so the results will be only summarized here. There were two test problems, for which BUCKY was compared with HYADES and experiment; radiative burnthrough of a gold foil and the breakup of a spherical hohlraum target.

Many burnthrough experiments have been performed on the Nova laser. A thin gold foil is placed on the side of a cylindrical gold hohlraum. The Nova laser beams are focused into the hohlraum, generating about 250 eV blackbody radiation. This radiation generates a Marshak wave that burns through the gold. The radiation leaking out the back of the gold foil is observed with the DANTE x-ray diode array. For a 2 μm thick gold foil,

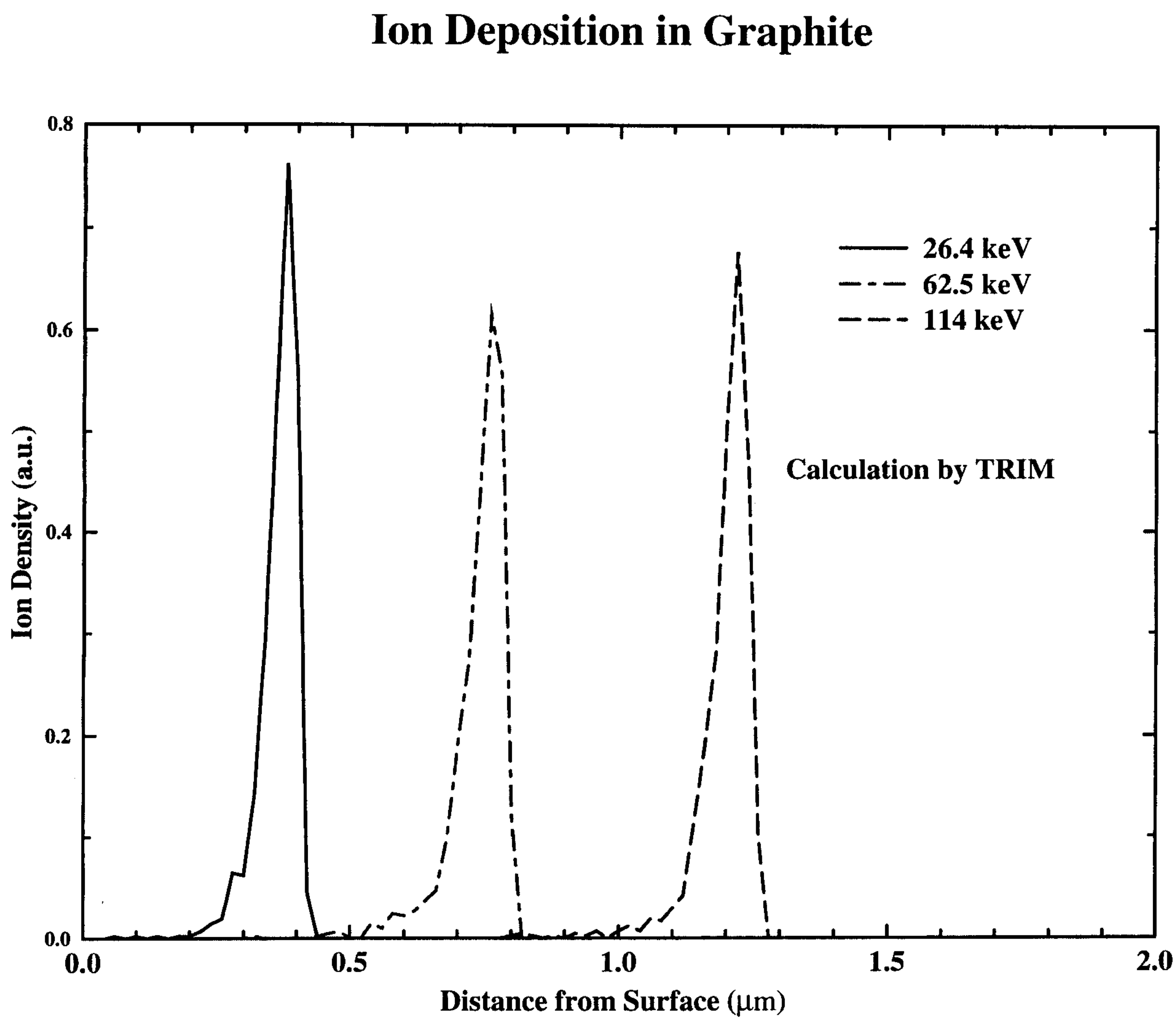

Figure 4.1. TRIM simulation of the deposition of tritium into 1.8 g/cm^{-3} graphite. The tritium spectrum is discrete (26.4 keV, 62.5 keV and 114 keV).

Table 4.2. Energy Partitioning in Gold Burnthrough Experiment

	BUCKY	HYADES
Time (ns)	4	5.2
Kinetic Energy (J/cm^2)	46.02	46.87
Internal Energy (J/cm^2)	17.60	15.82
Radiation (J/cm^2)	.18	.29
Radiation Losses (J/cm^2)	77.7	51.12
Total (J/cm^2)	141.5	114.1

Table 4.3. Energy Partitioning of NIF Indirect Drive Target

	BUCKY	HYADES
Time (ns)	20	20
Kinetic Energy (MJ)	2.13	2.21
Internal Energy (MJ)	3.06	1.95
Radiation (MJ)	.05	.02
Radiation Losses (MJ)	0.33	1.23
Total (MJ)	5.57	5.41

radiation in the 0.5 keV channel is observed to burn through, defined as reaching 1/2 of the peak emission power, in 1.035 ns ($\pm$ 30 ps). BUCKY predicts 1.22 ns and HYADES 1.31 ns. The energy partition of this BUCKY simulation is compared with the HYADES simulation in Table 4.2. The idealized blackbody temperature history, shown in Figure 4.2, was used. The predicted power in the 0.5 keV channel is shown in Figure 4.3. The velocity, temperature and density profiles are shown in Figures 4.4, 4.5 and 4.6. The time-integrated spectrum of x-rays emitted from the back of the foil is pictured in Figure 4.7. These are very similar to the predictions of HYADES.

In the second test problem, the radiative breakup of a spherical hohlraum target is calculated by BUCKY and HYADES. The target considered, shown in Figure 4.8, consists of a gold shell surrounding a plastic coated fuel capsule. At the time of the comparison, BUCKY was not able to properly do implosions and burn (it is now) so the calculations were started in the bang time configuration predicted by HYADES. The two codes are compared in energy partitioning, as shown in Table 4.3. The radiated power from BUCKY is shown in Figure 4.9. The first peak is due to collision between the rapidly expanding

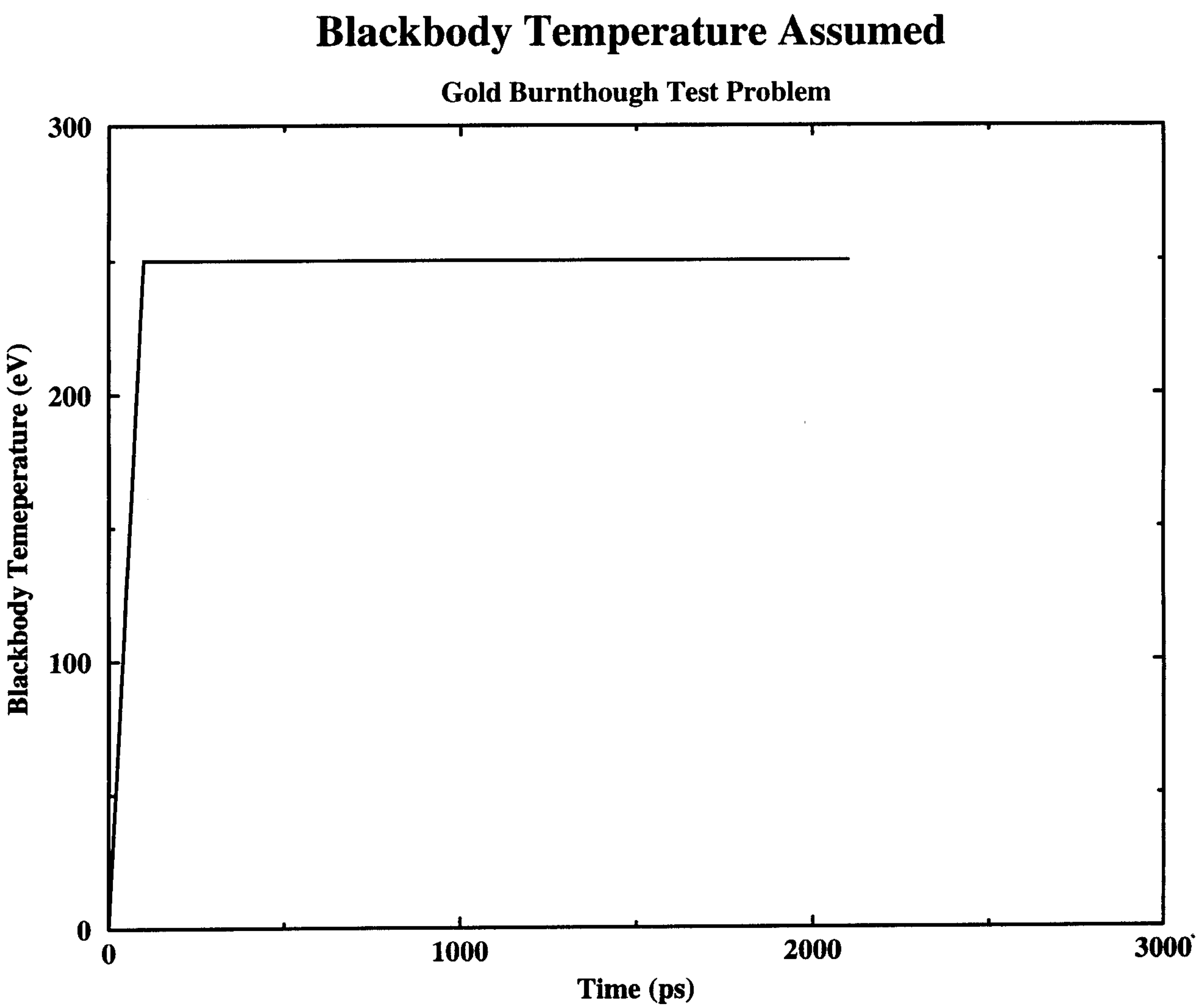

Figure 4.2. Assumed blackbody temperature versus time for radiation burnthrough experiment.

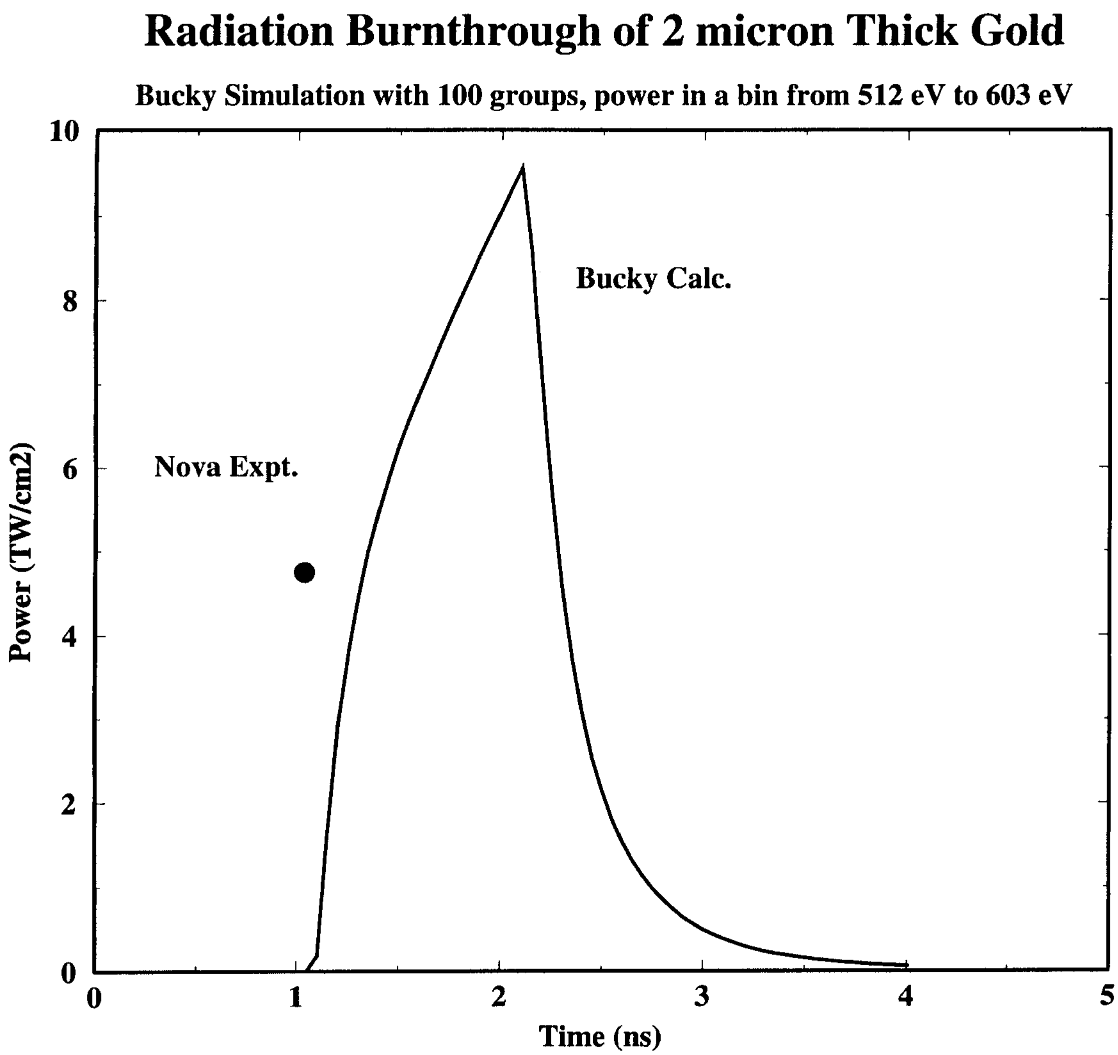

Figure 4.3. Radiation power burning through a 2 cm thick gold foil in 0.5 keV channel. Predicted by BUCKY.

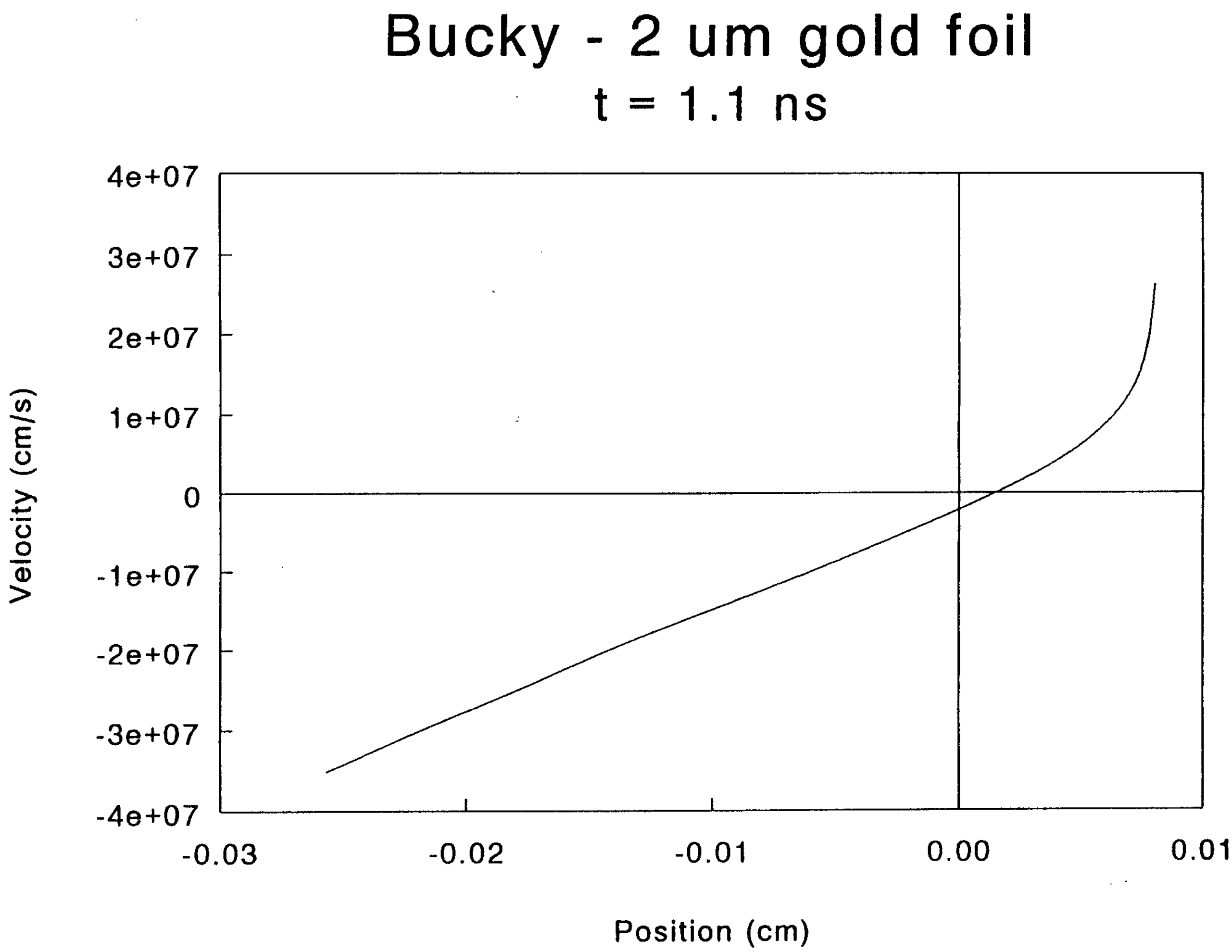

Figure 4.4. Velocity in a radiation driven gold foil at 1.1 ns. Predicted by BUCKY.

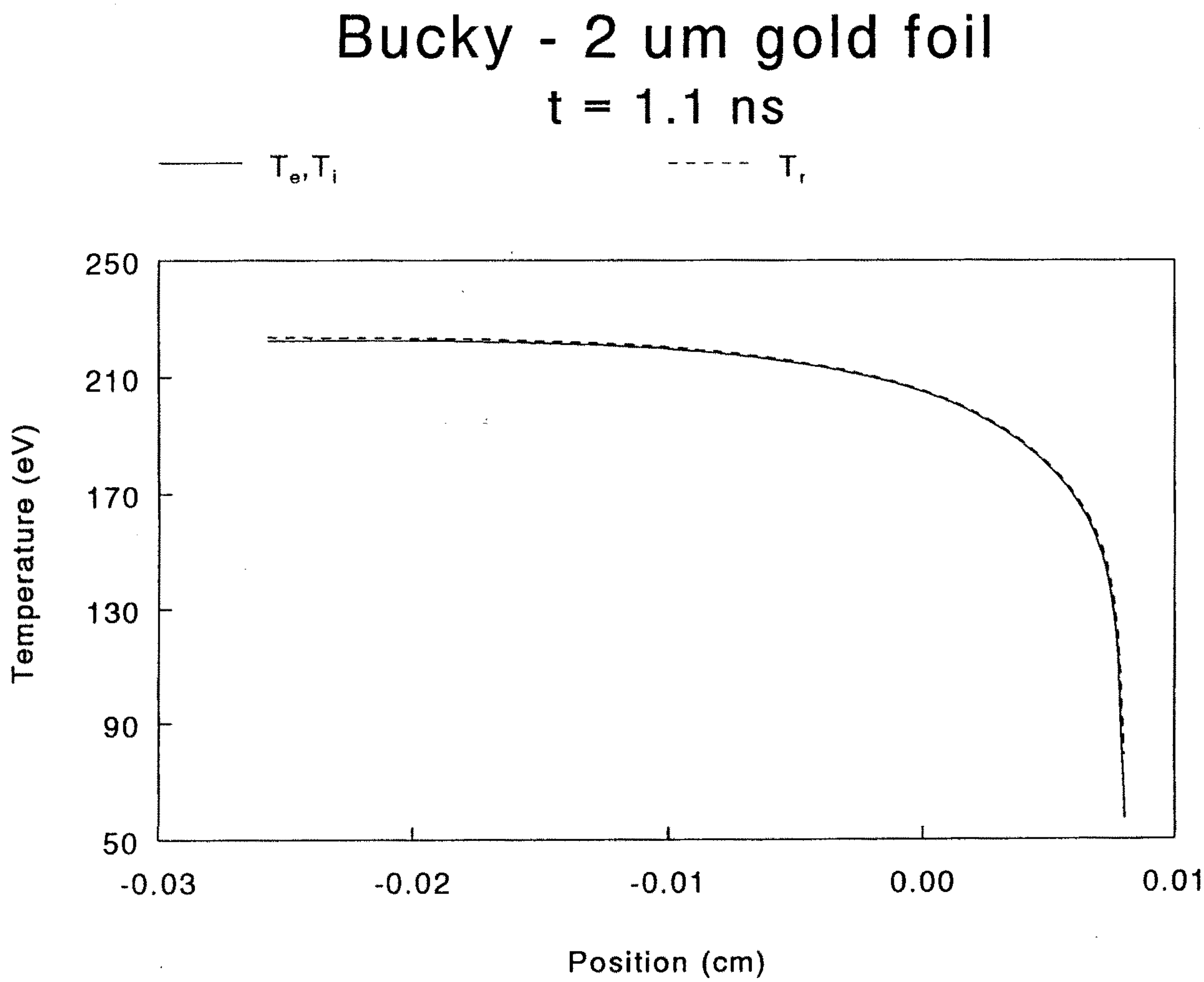

Figure 4.5. Radiation and plasma temperatures in a radiation driven gold foil at 1.1 ns. Predicted by BUCKY.

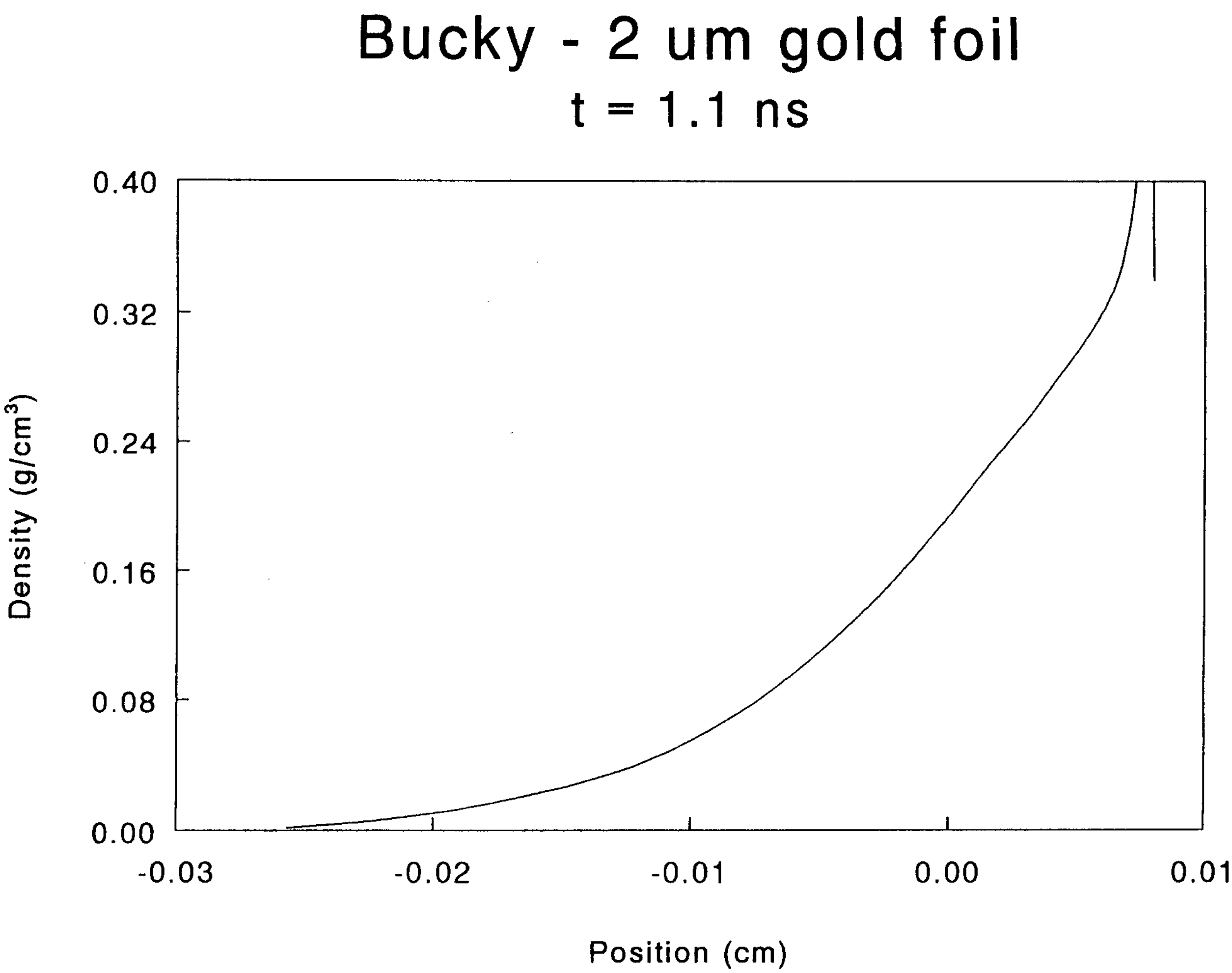

Figure 4.6. Density in a radiation driven gold foil at 1.1 ns. Predicted by BUCKY.

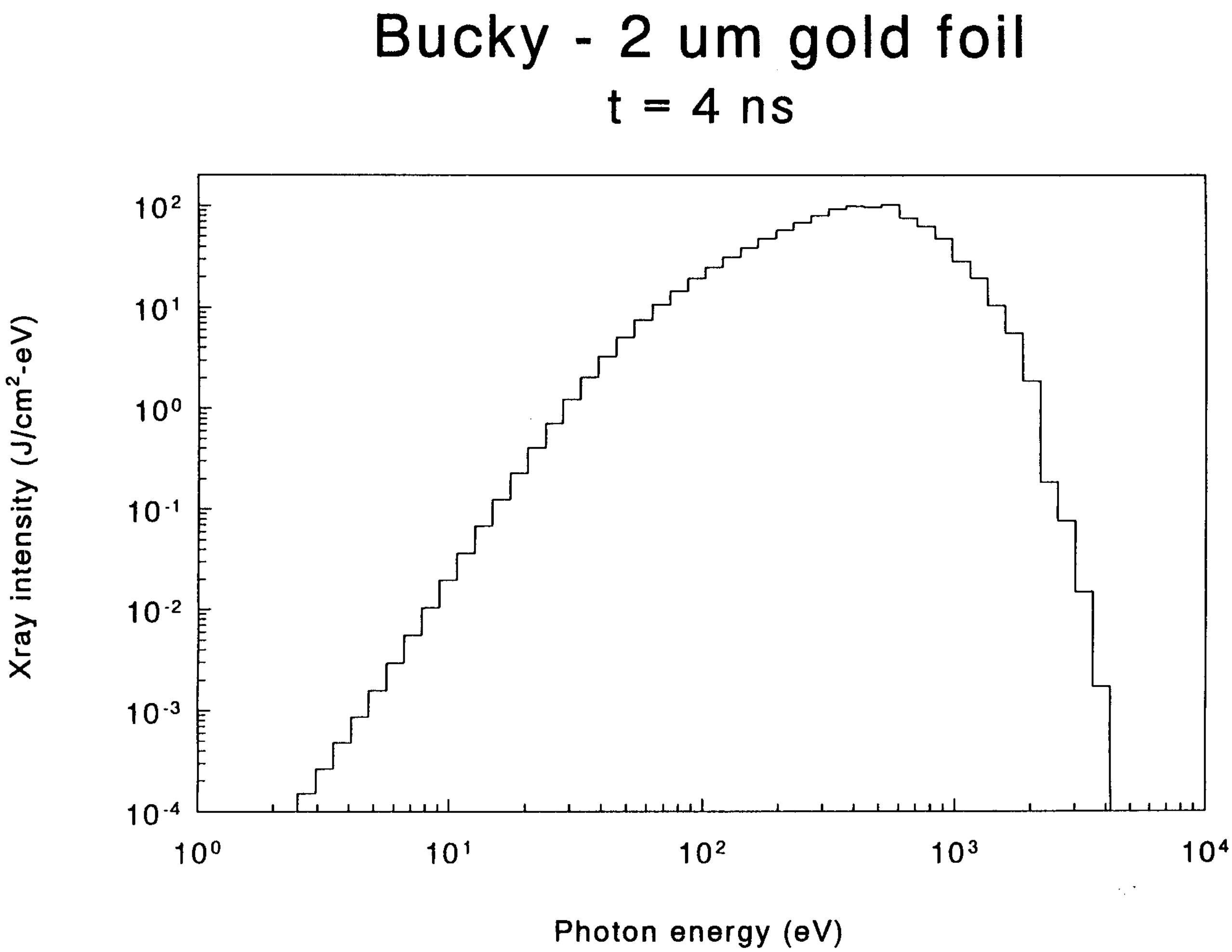

Figure 4.7. Time-integrated radiation spectrum burning through a 2 cm thick gold foil. Predicted by BUCKY.

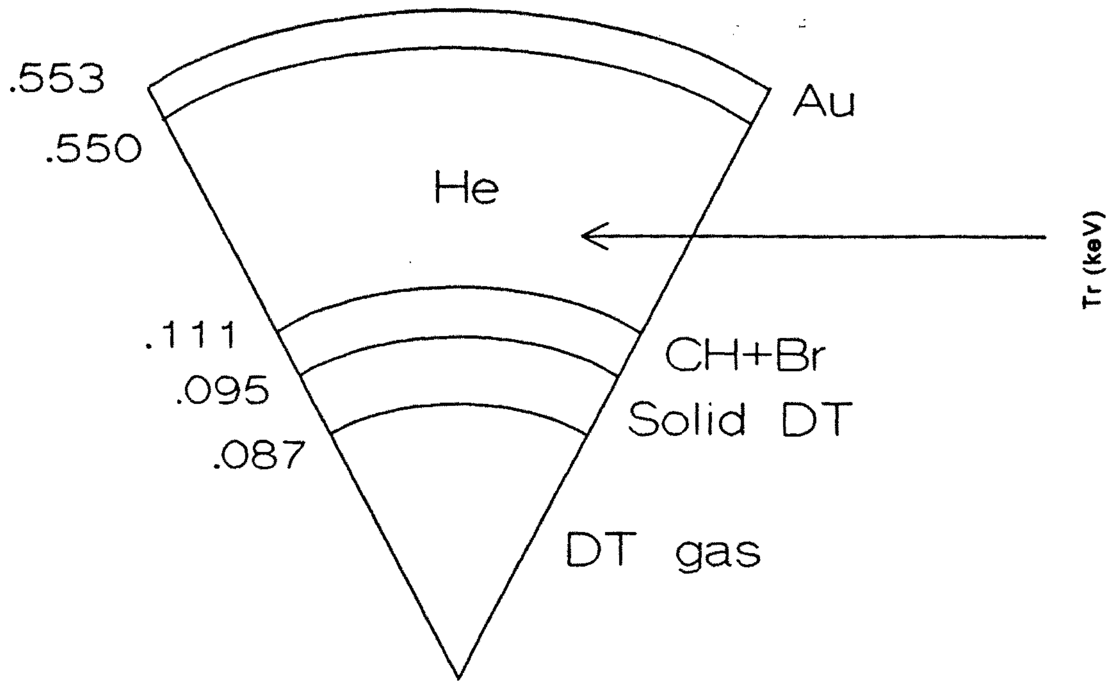

Figure 4.8. Sample target for comparison of x-ray emission predicted by BUCKY and HYADES.

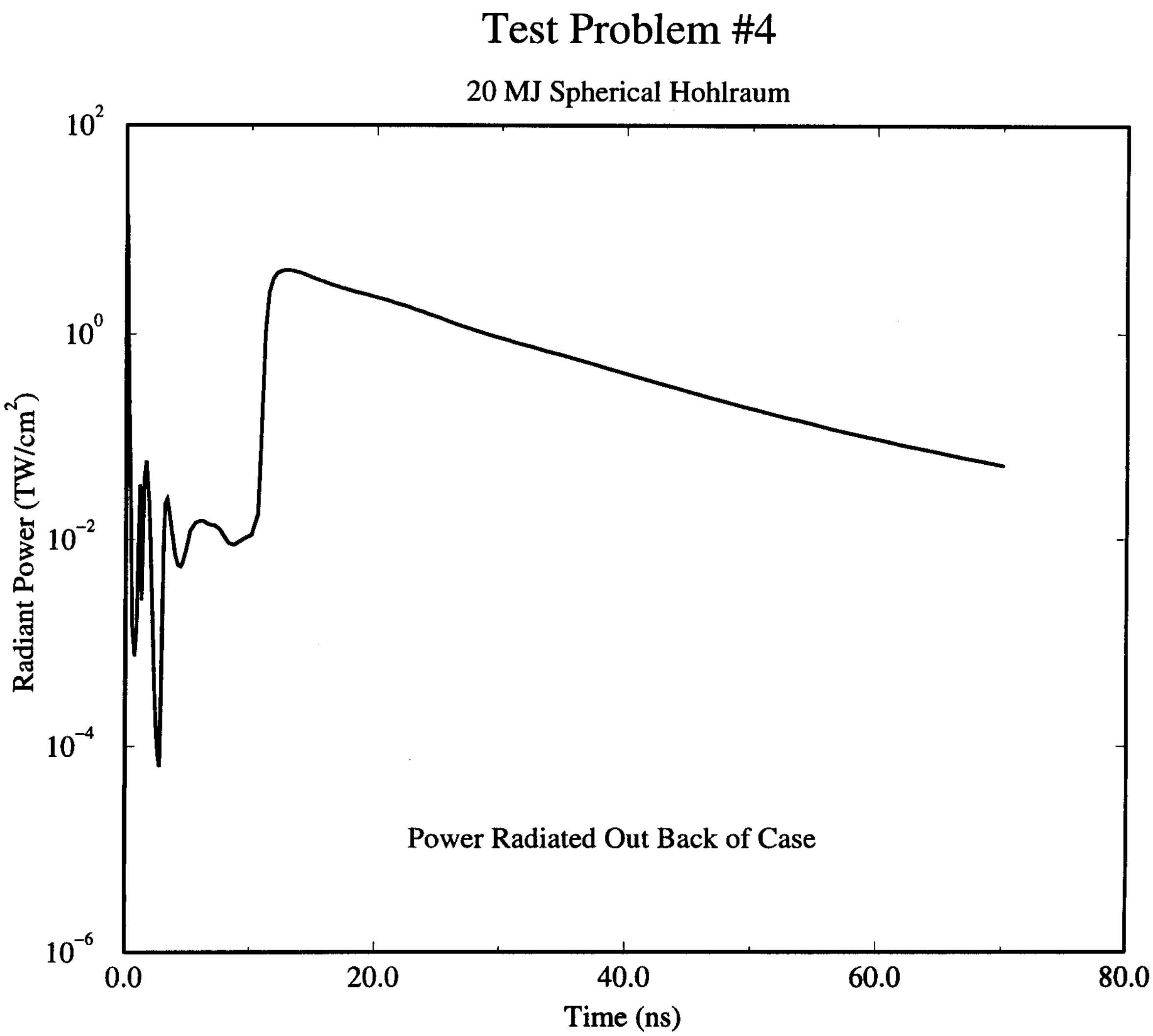

Figure 4.9. X-ray emission power from sample target predicted by BUCKY.

capsule and the hohlraum case. The final pulse is due to radiation burning through the case. The time-integrated x-ray spectrum emitted by the target is shown in Figure 4.10. The spectrum and the form of the x-ray power pulse are in agreement between the two codes, though the energy partitioning is not.

The disagreement in the energy partitioning could be settled with experiments. One possible experiment is a colliding plasma in a "tuna can", shown in Figure 4.11. This type of experiment has been done at LANL [12] and elsewhere. Two plasmas are created on opposite parts of the interior of the can. These two plasmas collide, stagnate and generate x rays. If one plasma is plastic and the other is gold and there is a helium gas in between, the situation that occurs in the target is mimicked. Therefore this experiment could benchmark the code's ability to calculate x-ray emission from the target.

4.1.3. X-ray Vaporization

X-ray vaporization is predicted by the BUCKY code. The time-dependent deposition of a multigroup spectrum of x rays is calculated in the solid and vapor materials, using cross sections from fits to experimental values [13]. Heat transfer in the materials is simultaneously performed. Vaporization is modeled by converting zones of solid into zones of vapor. The zones of vapor are Lagrangian and exhibit hydrodynamic motion; the solid zones do not move. A zone makes this conversion either when the zones have sufficient internal energy to overcome the sensible heat and latent heat of vaporization, or when the surface vapor pressure has been high enough for a long enough time that the zone has evaporated. This model assumes that mass is lost as individual atoms of molecules, not as large chunks.

The x-ray vaporization in BUCKY has been compared with experiments done on the Helen laser [14]. In these experiments, a laser strikes a foil, creating x rays with approximately a 160 eV blackbody spectrum. The x rays are assumed to be emitted in a Gaussian pulse 1 ns wide. The fluence on a sample material is adjusted by varying the position of the sample relative to the x ray producing foil. The material loss is then measured. For Al_2O_3, BUCKY calculations were performed and compared with the Helen experimental results. The comparison is made in Figure 4.12. There is a minimum measurable value of about 0.1 μm in the Helen results. The actual uncertainty in the results is not known, but near the vaporization threshold the uncertainty must be at least 0.05 μm. The Helen data points at about 0.6 and 0.8 J/cm^2 shown to have zero depth removed, but to have some surface damage. This may mean a small depth removed that could not be measured. The Helen results show a threshold for vaporization of between 0.25 and

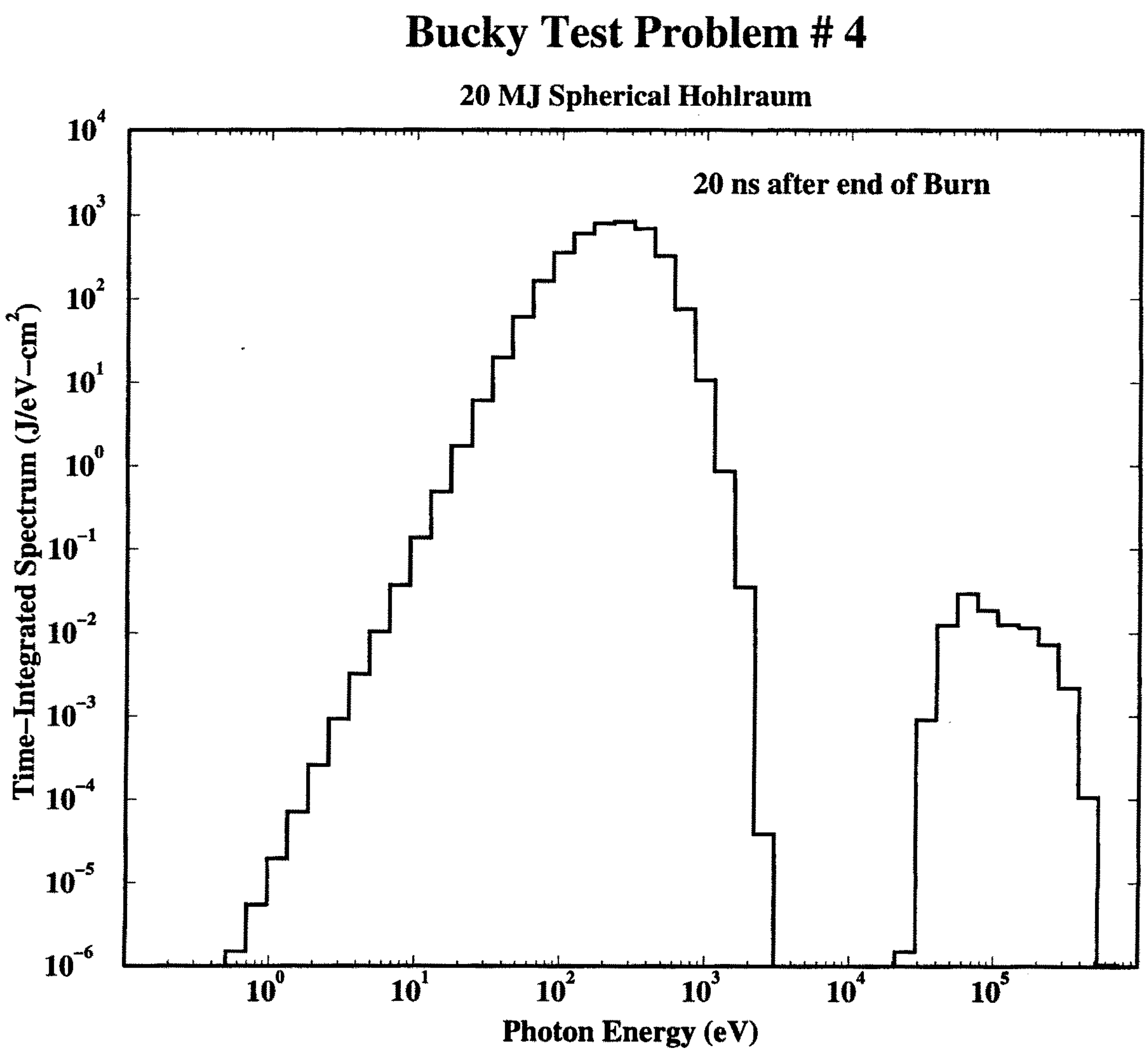

Figure 4.10. Time-integrated x-ray emission spectrum from sample target predicted by BUCKY.

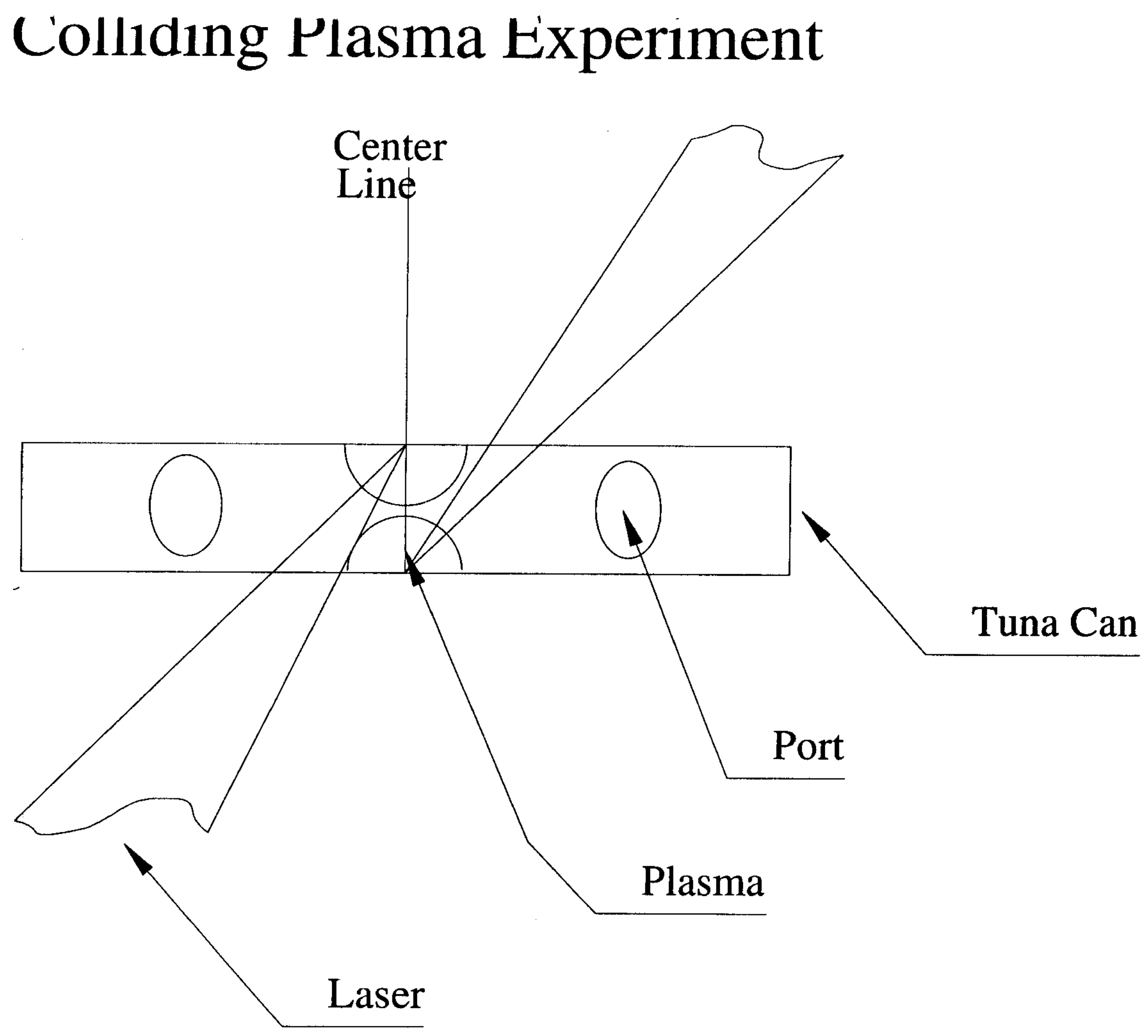

Figure 4.11. Schematic picture of colliding plasma experiment.

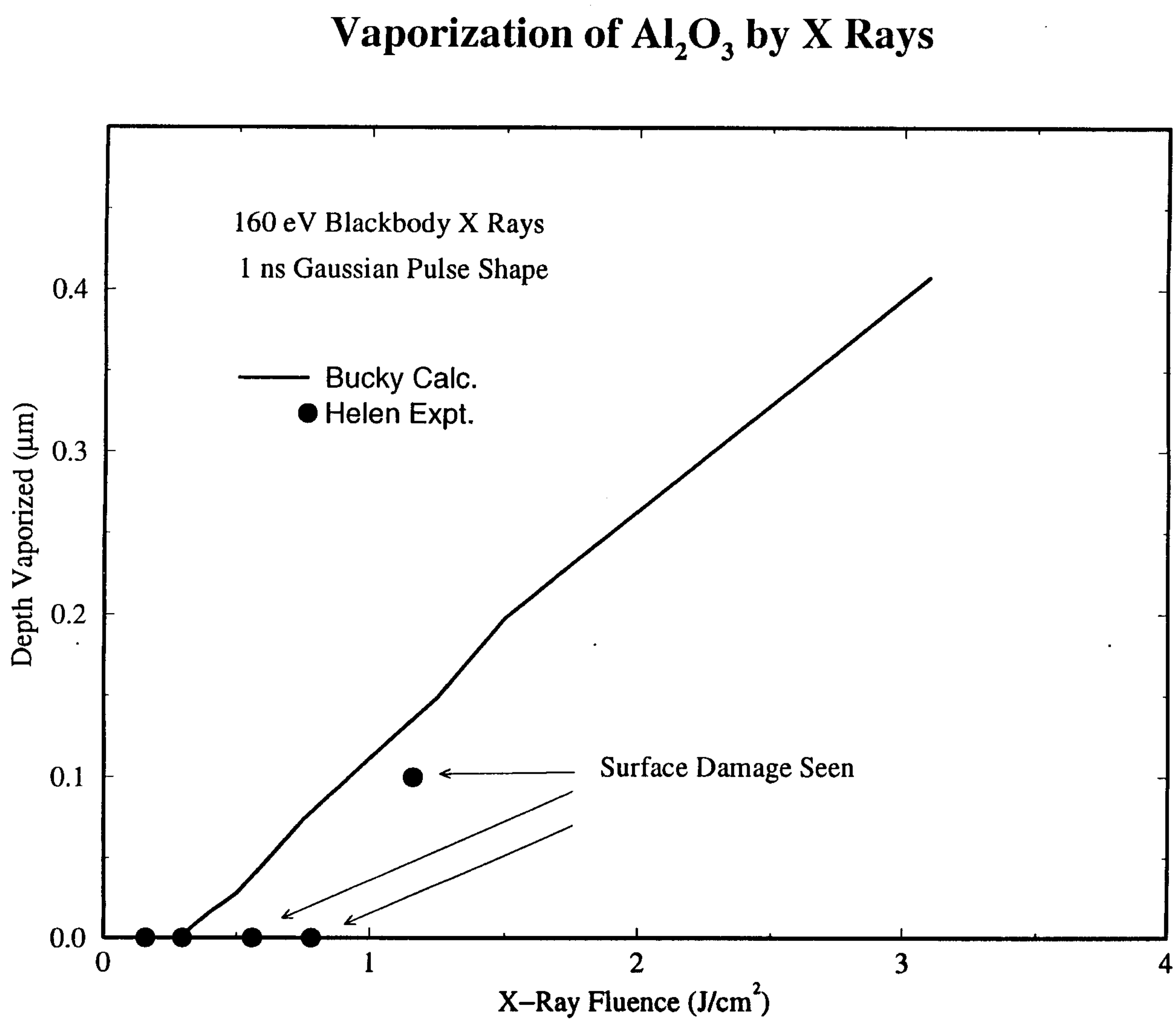

Figure 4.12. Vaporization of Al_2O_3 by 160 eV x rays. Results of Helen experiments are compared with BUCKY simulations. The minimum measurable loss depth in the Helen results is about 0.1 μm.

Table 4.4. Ion Vaporization Experiment Parameters

	Carbon	Proton
Peak Energy (keV)	500	500
Peak Current Density (A/cm^2)	60	30
Fluence (J/cm^2)	3.40	0.63

0.6 J/cm^2. The BUCKY simulations predict a vaporization threshold of 0.25 J/cm^2. At about 1.1 J/cm^2, Helen had a removal of 0.1 μm and BUCKY predicted 0.12 μm. So the agreement between BUCKY and Helen experiments was within experimental uncertainty.

Recently, the interpretation of these experiments has come into some doubt. Atomic force microscopy of these experiments has shown that the resulting surface is very rough, looking like large "divots" of material have been removed. This material was plasma sprayed so individual splats could have been removed by the shock resulting from recoil to the vaporization. This is totally divergent from the material removal model in BUCKY, so the agreement with experiment could be just due to good fortune.

4.1.4. Ion Vaporization and Melting

The ability of BUCKY to model the vaporization of materials by ions has been tested by comparing a simulation with an experiment performed at Sandia National Laboratories. Tim Renk of SNL has irradiated a pure aluminum sample with 4 J/cm^2 of mixed carbon ions and protons and has measured the melt depth. The experiment was performed with a light ion diode focusing a beam onto a sample across a distance of 25 cm. The experimental parameters are given in Table 4.4. The pulse shape for the two ions is shown in Figure 4.13. This is the pulse shape seen at the surface of the sample. The carbon ions arrive after the protons because they are moving more slowly. The experiment yields a 5 μm thick melt layer.

The results of a BUCKY simulation of this experiment are shown in Figures 4.14 through 4.19. The peak surface temperature, shown in Figure 4.14, is about 2800 K and is reached at 160 ns after the start of the protons reaching the sample. The temperature profile at 60 ns is due to the protons, which have a range of a few μm in aluminum. The profile, shown in Figure 4.15, has a temperature peak about 2.5 μm into the material. The melting temperature of aluminum is 933 K, so the protons do no melting. The profile

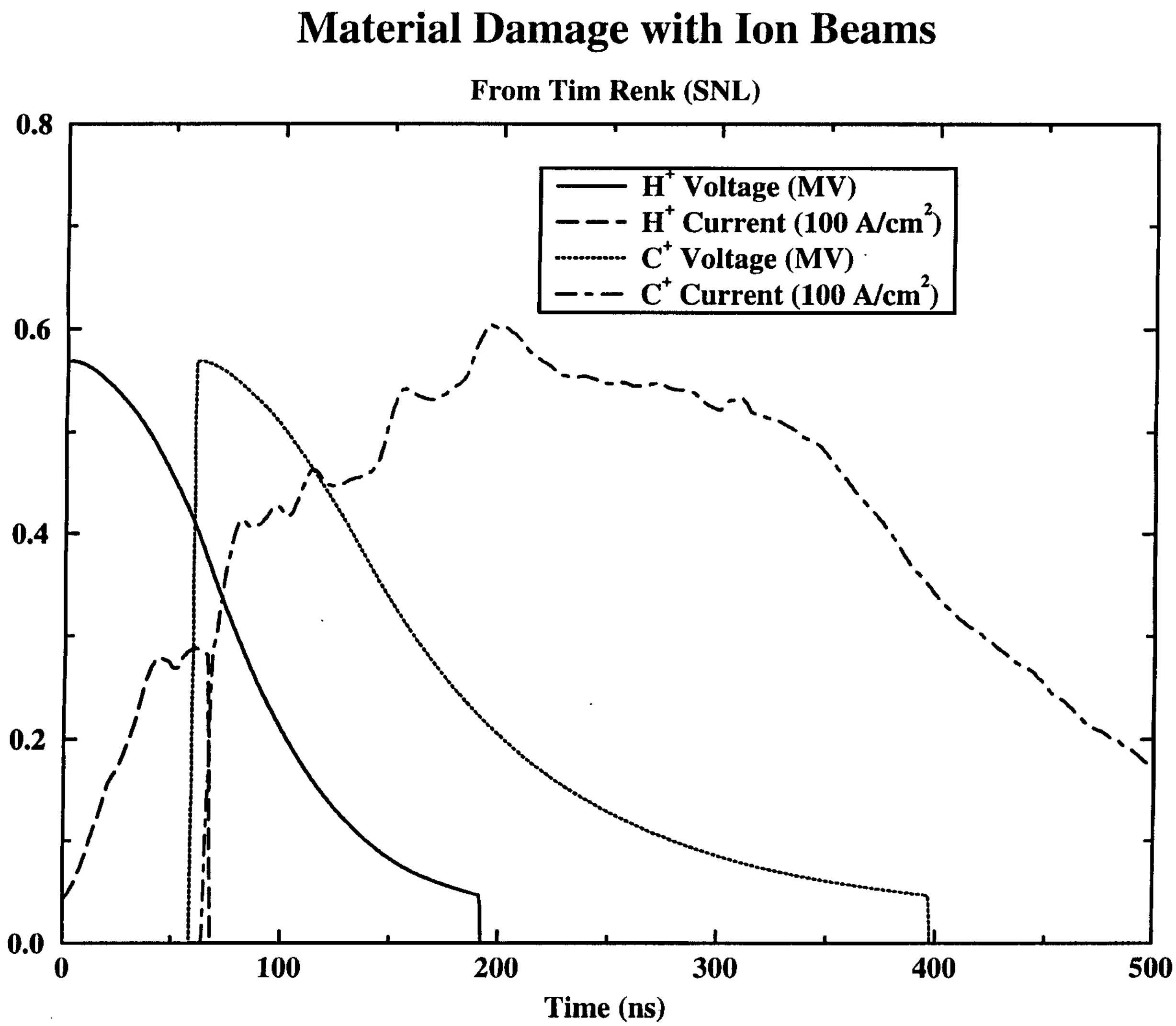

Figure 4.13. Current density and voltage for ions on surface of aluminum.

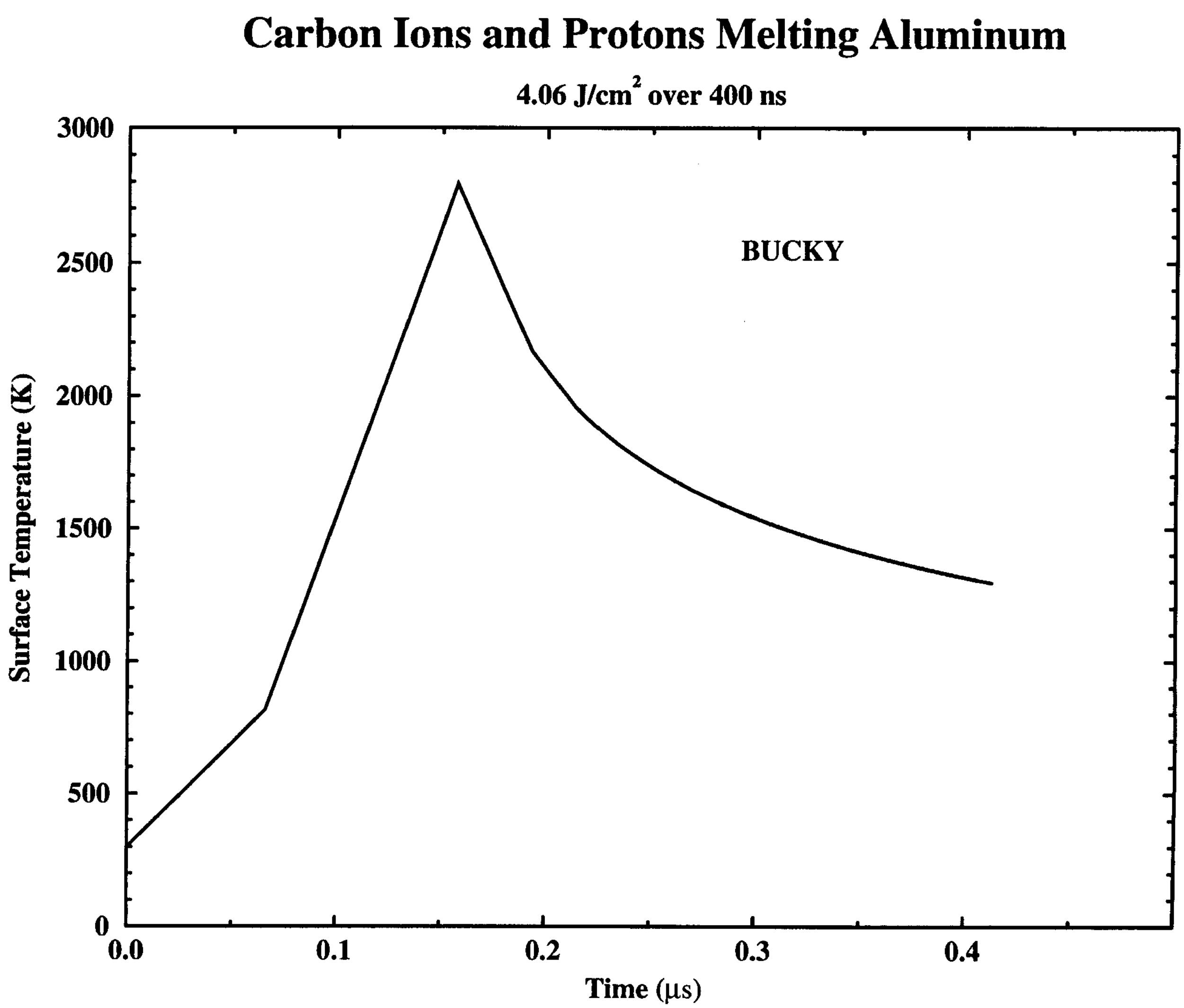

Figure 4.14. Surface temperature of aluminum irradiated by proton and carbon beams.

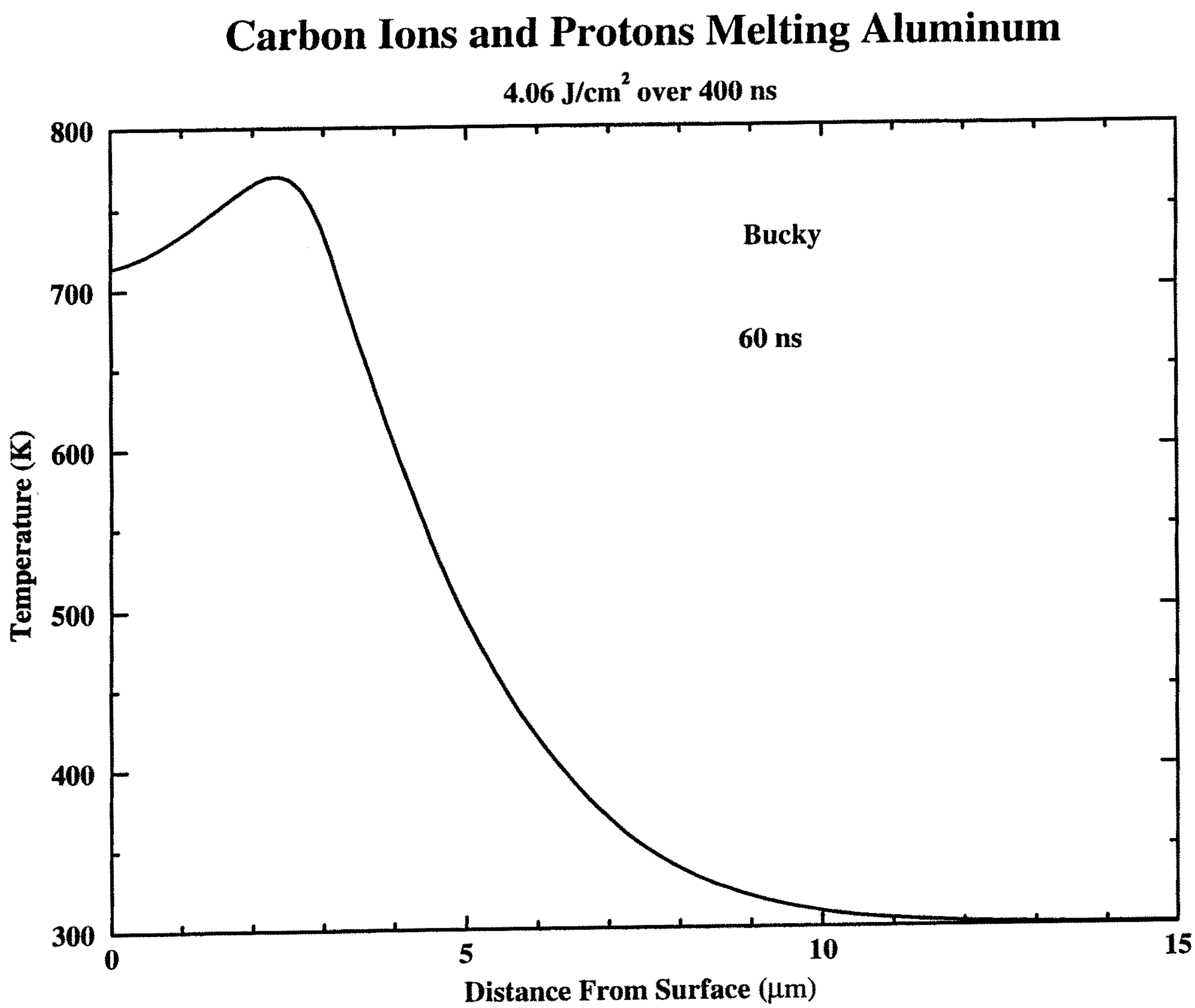

Figure 4.15. Temperature profiles of aluminum irradiated by proton and carbon beams 60 ns after start of proton beam.

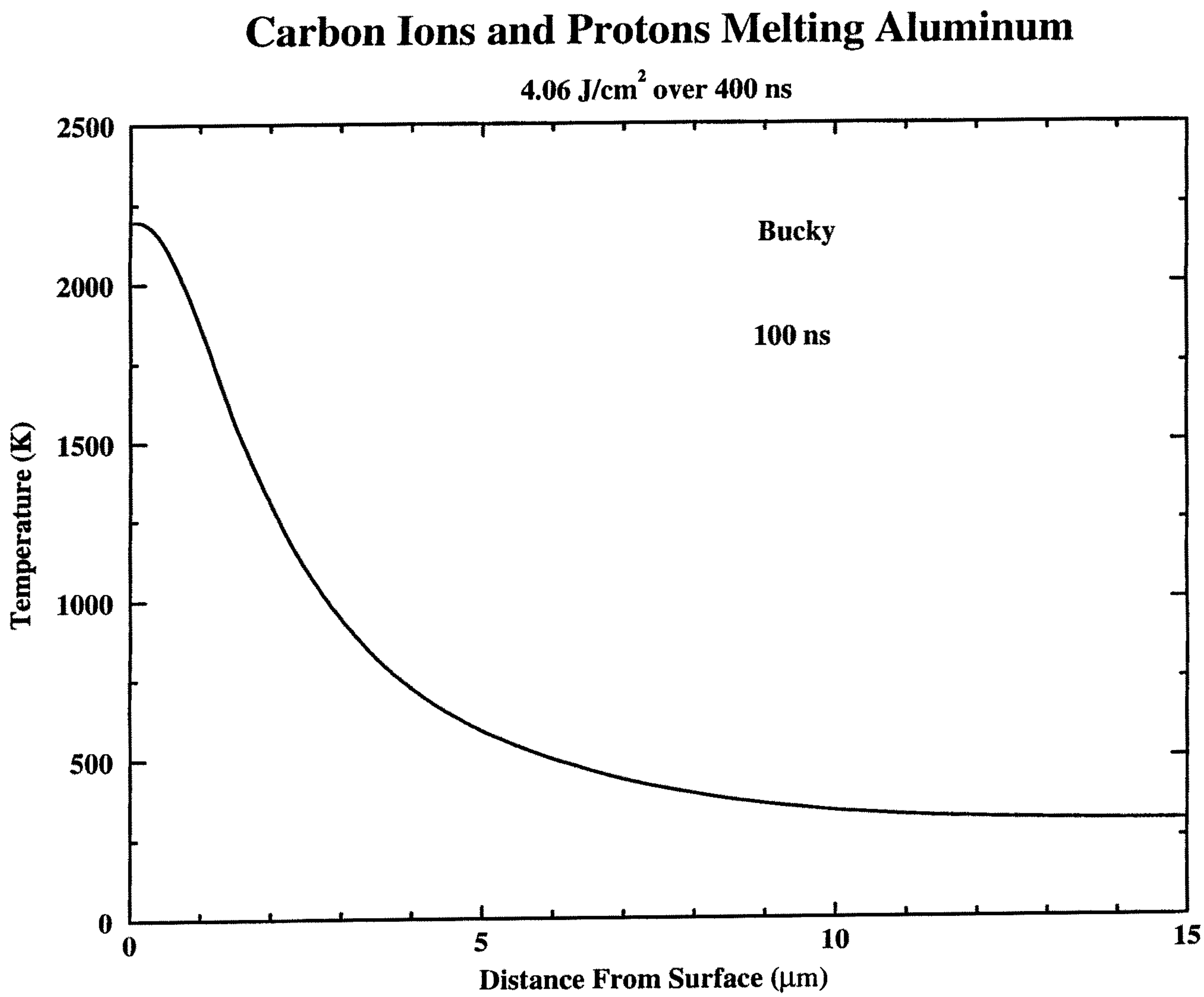

Figure 4.16. Temperature profiles of aluminum irradiated by proton and carbon beams 100 ns after start of proton beam.

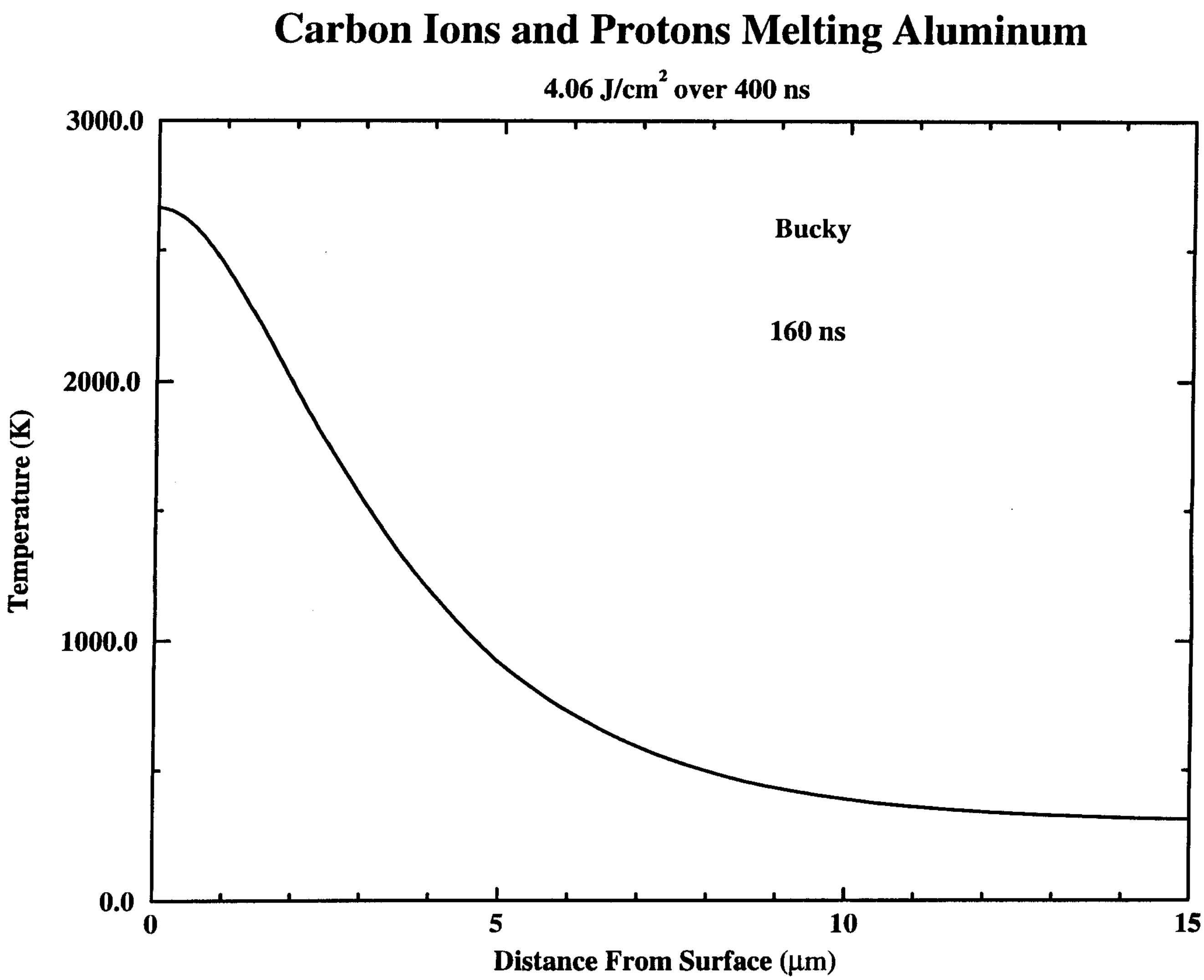

Figure 4.17. Temperature profiles of aluminum irradiated by proton and carbon beams 160 ns after start of proton beam.

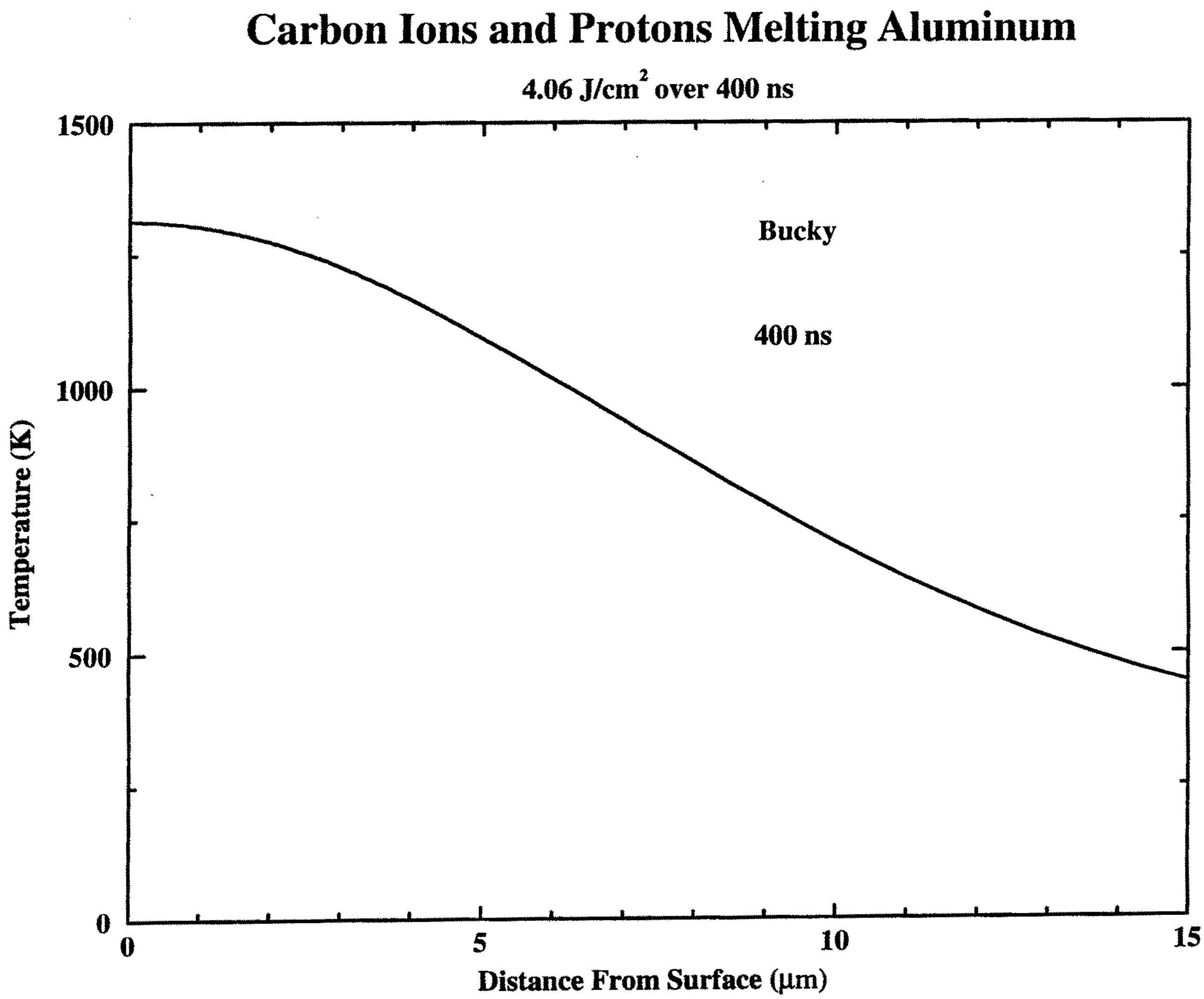

Figure 4.18. Temperature profiles of aluminum irradiated by proton and carbon beams 400 ns after start of proton beam.

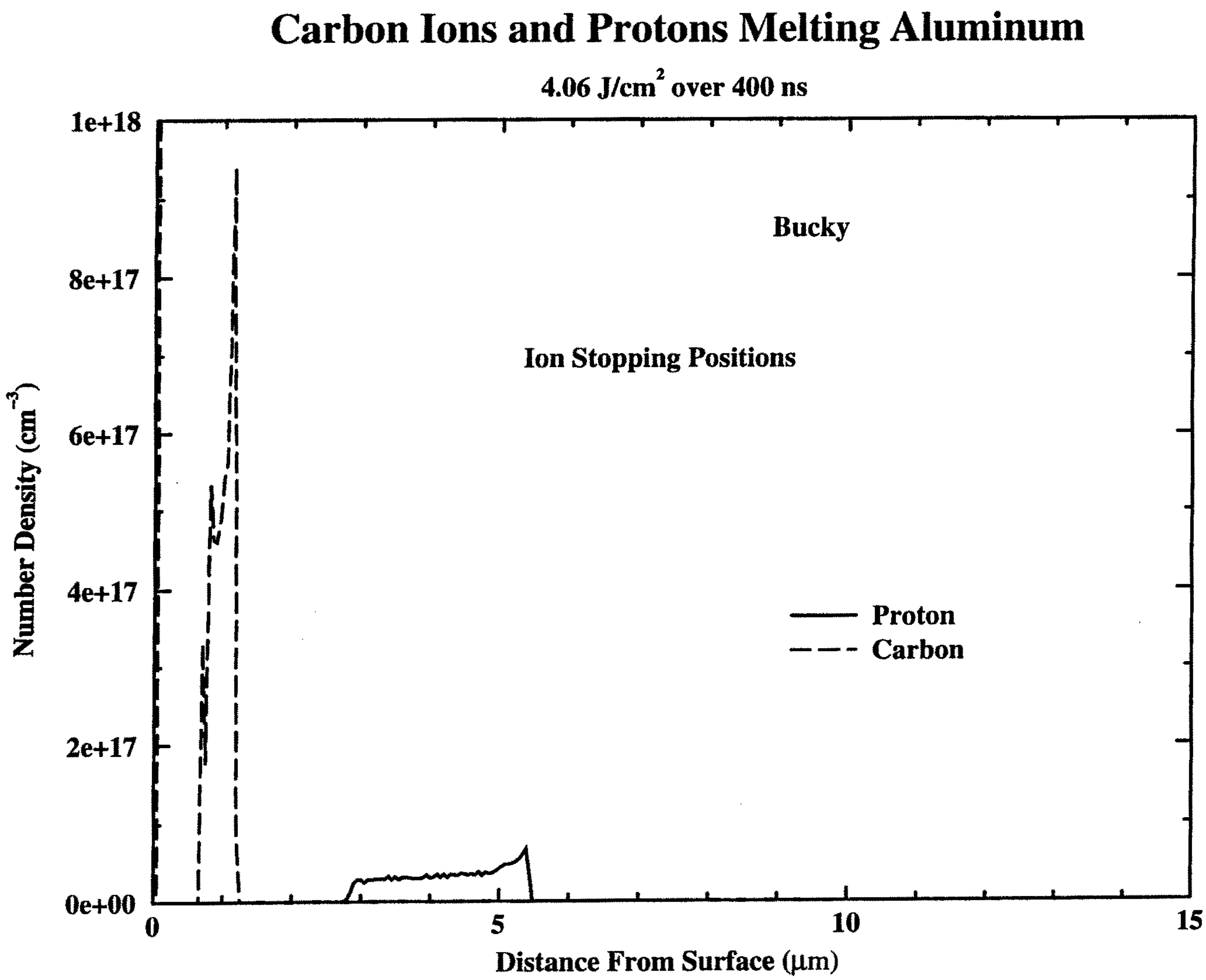

Figure 4.19. Number density profiles for carbon ions and protons deposited in aluminum by a single shot. Calculated by BUCKY.

at 100 ns, Figure 4.16 is dominated by carbon ions. The peak in temperature is at the surface because the range of carbon is so much shorter. The melt depth is estimated by just considering all material above the melting temperature to be melted. This ignores the effect of latent heat. The melt depth at 100 ns is about 3 μm. The maximum temperature is reached at 160 ns and the temperature profile is shown in Figure 4.17. The melt depth at this time is about 5 μm. At 400 ns, the profile in Figure 4.18 is predicted, which has a melt depth of about 7 μm. If the calculation were carried out to a later time, only a small amount of additional depth would be melted. The density of beam ions in the aluminum builds through out the shot due to deposition. The final density profiles of the deposited ions is shown in Figure 4.19. The carbons are much closer to the surface. This can be compared with the TRIM code densities, shown in Figure 4.20, where 500 keV protons and carbons (monoenergetic) are deposited in aluminum. TRIM calculations include the effects of straggling, which are seen to be important for 500 keV carbon. The maximum ranges predicted by BUCKY and TRIM are quite close.

The BUCKY calculations agree reasonably well with the TRIM calculations and with the SNL experiments. BUCKY predicts 0.05 μm of vaporization. This has not been detected in the SNL experiments.

4.2. Code Development

4.2.1. BUCKY Laser Deposition

Laser deposition has been added to the BUCKY code. The model used considers only inverse Bremsstrahlung in regions where the local electron plasma frequency is less than the laser frequency. In regions where the plasma frequency is greater than the laser frequency, the laser energy that enters any zone is entirely absorbed. The absorption coefficient in the underdense region is, therefore,

$$\kappa = (2\pi)^{1/2}\,(16\pi/3)\,\frac{e^6}{c(m_e kT_e)^{3/2}} Z n_e^2 \frac{\ln\Lambda}{\omega_L^2(1-(\omega_{pe}/\omega_L)^2)^{1/2}}\ . \tag{3}$$

Here, ω_{pe} and ω_L and the electron plasma and laser frequencies and $\ln\Lambda$ is the familiar expression from atomic collision theory.

The model has been tested by comparison with the classic results of Kidder [15]. BUCKY was used to implode a large aspect ratio target with an ideal laser pulse shape. The hydromotion predicted by BUCKY was indistinguishable from the result published by Kidder.

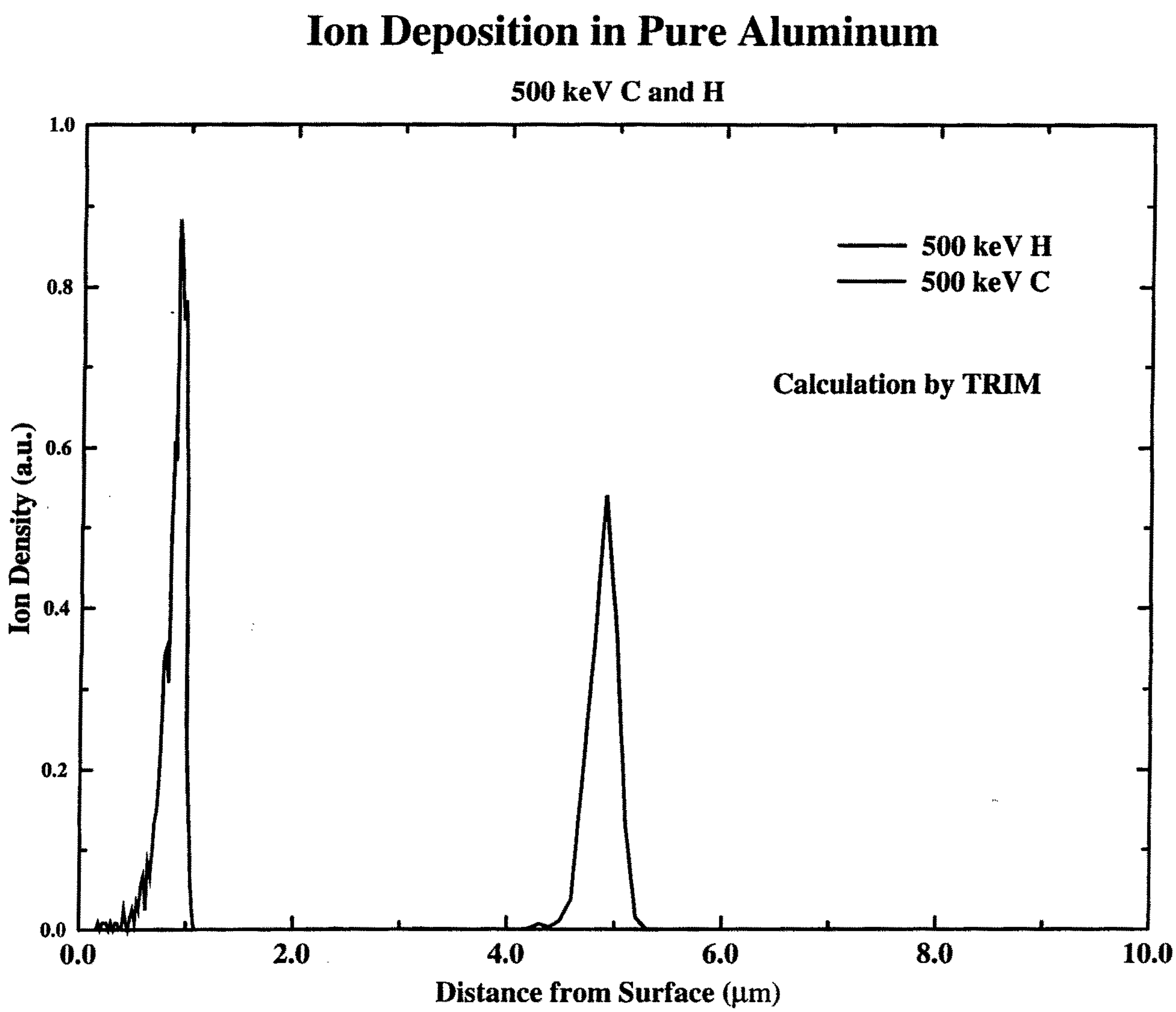

Figure 4.20. Number density profiles for carbon ions and protons deposited in aluminum by a single shot. Calculated by TRIM.

4.3. BUCKY Ion Deposition in Solids

The calculation of the deposition of ions in solids by the BUCKY code has been improved. Originally, the code treated the ion deposition in solids as a surface energy source. The code divides material into two parts; hydrodynamic regions where the material is allowed to move and solid or liquid regions, where hydrodynamic motion does not occur. Heat transfer is calculated in both parts, though radiation transport is not calculated in solids. Photons reaching the interface between vapor and solid are deposited in the first solid zone, which is the way that ions were originally treated. Now, the ion deposition is calculated in the solid material as a function of distance using the model discussed above. The code also now records the position that the ions stop in the solid, which is a new feature.

4.3.1. ZEUS 2-D Radiation Hydrodynamics Code

The ZEUS-2D radiation-magnetohydrodynamics code [16, 17, 18] is being augmented to add the key capabilities of the University of Wisconsin's 1-D BUCKY code, including

- Multiple materials,
- Multigroup frequency dependence,
- Table lookup of detailed opacities and equations of state,
- Energy deposition in surfaces, and
- Fusion burn.

ZEUS-2D is a two-dimensional, Eulerian-mesh code, written in covariant orthogonal coordinates and solved by finite differences with operator splitting into implicit source and explicit transport steps. The fundamental hydrodynamic equations can be solved alone or with magnetohydrodynamics, radiation, or both. The finite-difference mesh can be modified dynamically, although ZEUS-2D is not an adaptive-mesh code, and the mesh spacing can be varied independently in both dimensions.

The unmodified ZEUS-2D code has been tested on simple radiation diffusion, micro-explosion, and hohlraum test problems, and it appears to be a suitable code upon which to base the desired modifications. Multiple materials have been implemented by including the solution of a separate equation of continuity for each species. The modifications to the difference equations required to add multigroup frequency dependence have been developed and tested in a small auxiliary code, using the same variable names and covariant differencing scheme presently in ZEUS-2D. These modifications will soon be introduced into ZEUS-2D. The table lookup subroutines from the BUCKY code for equations of state and opacities have been merged with the ZEUS-2D code, and debugging of this merger is in its final stages.

5. Future Work

- **Indirect Drive Target Emissions**

  Experiments to confirm the x-ray emission predictions of BUCKY, Lasnex and HYADES need to be performed. These should include something like the colliding plasma "tuna can" experiments to study the emission by the stagnated plasma. The ion mean free paths are relatively long in this stagnated plasma and all of these codes assume that there is no interpenetration of the plasmas. The closing of the laser entrance hole to the x rays emitted inside the hohlraum is predicted by Lasnex. ZEUS calculations will study this same phenomenon. Experiments to measure the angle dependent x-ray spectrum from a hohlraum should be performed on Nova or Omega to verify these code predictions. Debris emission needs more study with the codes. The hydromotion out the laser entrance holes is a very difficult problem for a Lagrangian code like Lasnex. ZEUS is Eulerian and other adaptive mesh codes could be considered. Of course these predictions also need to be tested against experiments of debris from Nova or Omega hohlraums. BUCKY should be used to follow a NIF spherical hohlraum target from laser deposition through implosion, burn and x-ray emission. This should then be compared with HYADES.

- **Direct Drive Target Emissions**

  BUCKY should be used to follow a NIF direct drive target from laser deposition through implosion, burn and x-ray emission. All of the needed pieces are in BUCKY and have been tested. Preliminary efforts to shape the laser pulse have not yet achieved a ρR of more than 0.5 g/cm^2 and a yield of more than 100 kJ. Experimental verification could be performed by simulation of Omega direct drive target experiments. These experiments could be performed with add-on measurements of x rays and debris.

- **Ion Debris Damage** The deposition of ions in wall materials should be calculated using continuous ion energy spectra. This will provide a deposition profile of tritium in the target chamber materials, which is required for analysis of cleaning requirements and tritium outgassing. Experiments with ion beams are possible to create the conditions experienced by NIF target chamber materials and can validate the BUCKY predictions of ion generated melting and vaporization.

- **X-Ray Damage** The calculation of x-ray damage to plasma sprayed material with BUCKY needs further development and verification. The present model does not account for "divots" seen in some experiments. Comparisons with more experiments from Helen, Nova and Phebus need to be made.

- **Laser Deposition** The laser deposition model in BUCKY needs further development. Correction of the current model to allow off-normal laser irradiation would allow the simulation of many experiments that BUCKY can not currently study. These simulations include the NIF hohlraum target, where the laser beams strike the gold case at an off-normal angle. The addition of the effects of Stimulated Brillioun and Raman scattering would also be valuable. Currently this has to be accounted for by just reducing the total laser energy. Including SRS and SBS would give BUCKY a unique capability.

Acknowledgement

The bulk of this work was supported by Lawrence Livermore National Laboratory under Contract #B310594. The Lasnex calculations were performed at Los Alamos National Laboratory with Robert Peterson being supported by LANL as a visiting scientist. Part of the work done on the ZEUS code was support by the U.S. Department of Energy on a separate contract.

Prof. Ed Larsen was very helpful in studying the properties of γ-alumina. Wang Ping provided the equations-of-state and opacities for the BUCKY calculations. Many useful discussions occurred with Jon Larsen, of Cascade Applied Sciences, and Andy Anderson, Mike Tobin and others at LLNL.

References

[1] J.J. MacFarlane, G.A. Moses and R.R. Peterson, "BUCKY-1 – A 1-D Radiation Transport Code for Simulating Inertial Confinement Fusion High Energy Density Plasmas," University of Wisconsin Fusion Technology Institute Report UWFDM-984 (August 1995).

[2] Jon Larsen, Cascade Scientific Inc., private communication, (1995).

[3] J. Larsen, "HYADES Users' Guide," Cascade Applied Sciences, Inc. Report CAS044 (May 1995).

[4] P. Wang, "EOSOPA - A Code for Computing the Equations of State and Opacities of High Temperature Plasmas with Detailed Atomic Models," University of Wisconsin Fusion Technology Institute Report UWFDM-933 (December 1993).

[5] J. Lindhard and M. Scharff, "Energy Dissipation by Ions in the keV Range," *Phys. Rev.* **124**, 128 (1961).

[6] H.A. Bethe, Handbuck der Physik, Edited by S. Flugge, Springer-Verlag, Berlin, Vol. 24, 273 (1933).

[7] J.J MacFarlane and P. Wang, "Numerical Simulation of High Energy Density Plasmas in KALIF Beam-Target Interaction Experiments," University of Wisconsin Fusion Technology Institute Report UWFDM-1002 (December 1995).

[8] J.F. Ziegler, "TRIM-90 The Transport of Ions in Matter," IBM - Research, Yorktown, New York (1990). Also, J.F. Ziegler, J.P Biersack, and U. Littmark, "The Stopping and Range of Ions in Solids," Pergamon Press, New York (1985).

[9] R.E. Tokheim, SRI, private communication (1996).

[10] "The Encyclopedia of Advanced Materials," Ed. D. Bloor, R.J. Brook, M.C. Flemings, and S. Mahajan (Pergamon) p. 89.

[11] "Thermodynamic Properties of Individual Substances," vol. 3, part 1, ed. L.V. Gurvich, I.V. Veyts, and C.B. Alcock (CRC) pp. 135-136.

[12] M.D. Wilke, et al., "X-ray Emission From Colliding Laser Plasmas," SPIE Conf. Proceedings, San Diego (July 1995).

[13] F. Biggs and R. Lighthill, "Analytical Approximations for X-Ray Cross Sections III," Sandia National Laboratories Report SAND-0070 (August 1988).

[14] A. Anderson, private communication.

[15] R.E. Kidder, *Nucl. Fusion* **16**, 3 (1976).

[16] J.M. Stone and M.L. Norman, "ZEUS-2D: A Radiation Magnetohydrodynamics Code for Astrophysical Flows in Two Space Dimensions. I. The Hydrodynamic Algorithms and Tests," *Astrophysical J. Suppl.* **80**, 753 (1992).

[17] J.M. Stone and M.L. Norman, "ZEUS-2D: A Radiation Magnetohydrodynamics Code for Astrophysical Flows in Two Space Dimensions. II. The Magnetohydrodynamic Algorithms and Tests," *Astrophysical J. Suppl.* **80**, 791 (1992).

[18] J.M. Stone, D. Mihalas, and M.L. Norman, "ZEUS-2D: A Radiation Magnetohydrodynamics Code for Astrophysical Flows in Two Space Dimensions. III. The Radiation Hydrodynamic Algorithms and Tests," *Astrophysical J. Suppl.* **80**, 753 (1992).